Scanning of hadron cross section at DAΦNE by analysis of the initial-state radiative events

M. Konchatnij and N. P. Merenkov

Kharkov Institute of Physics and Technology National Science Center, 310108 Kharkov, Ukraine

The initial-state radiative events in electron–positron annihilation into hadrons at DAΦNE are considered. The corresponding cross section with the full first-order radiative corrections is calculated. The analytical calculations take into account the actual angular acceptance and energy cutoff of the DAΦNE photon detector. © *1999 American Institute of Physics.* [S0021-3640(99)00111-5]

PACS numbers: 13.65.+i, 13.40.Ks, 12.15.Lk

It is the general viewpoint at present that the dominant error in Standard Model fits stems from the fairly large uncertainty in the hadron contribution to the vacuum polarization (HVP). The limited knowledge of the HVP also affects the precise determination of the muon anomalous magnetic moment.[1,2] The main problem comes at low and intermediate energies, because in these regions the HVP cannot be computed by means of QCD. The only possibility is to reconstruct it by a dispersion integral using the measured total cross section of the process $e^+e^- \rightarrow$ hadrons at continuously varying energies. Thus there is an eminent physical reason to scan the total hadronic cross section in the region up to a few GeV.

For this goal one can exploit the high luminosity of the upcoming fixed-energy e^+e^- colliders and use the process of radiative return to lower energies due to initial-state photon emission:[3–5]

$$e^-(p_1) + e^+(p_2) - \gamma(k) \rightarrow \gamma^*(q) \rightarrow H(q), \quad q = p_1 + p_2 - k, \tag{1}$$

where H denotes all final hadrons, and γ^* is the intermediate heavy photon. We write the final photon on the left-hand side of (1) to emphasize that it radiates from the initial state. The total hadronic cross section σ_t of the process (1), that defines the imaginary part of the HVP, depends on the heavy photon virtuality

$$q^2 = s(1-x), \quad s = 4\varepsilon^2, \quad x = \omega/\varepsilon,$$

where $\omega(\varepsilon)$ is the photon (electron) energy. Therefore, by measuring the photon energy fraction x one can extract the distribution $\sigma[s(1-x)]$.

In the case of a final-state radiation process

$$e^-(p_1) + e^+(p_2) \rightarrow \gamma^*(p_1 + p_2) \rightarrow \gamma(k) + H(q) \tag{2}$$

the quantity σ_t depends on s, while the hadron invariant mass q^2 remains the same. Consequently, to scan the total hadronic cross section one only needs to use events with initial-state radiation. The events with final-state radiation (FSR) are treated as a background.

Some possibilities for separating this background have been considered in Ref. 5. The model-independent method is based on the different angular distributions of photons emitted in initial and final states. It can be effective for for the high-statistics events expected at DAΦNE. The other approach involves modeling of the final hadronic states. In particular, the contribution to the total hadronic cross section due to the $\pi^+\pi^-\gamma$ channel for FSR with pointlike pions has been investigated in Ref. 5. On the other hand, the restriction of the hadron phase space, a measure which was also suggested in Ref. 5 to get rid of the FSR background, is, in our opinion, unsuited to the main goal, because the hadronic cross section measured in this case must depend on the restriction parameters, whereas the quantity σ_t (which enters into the dispersion integral) depends, by definition, on the heavy photon invariant mass only. Nevertheless, the FSR background under the DAΦNE conditions can be controlled.

Another source of background is due to the production of hadrons by two-photon and double-annihilation mechanisms. But the corresponding contribution to the cross section (provided that the photon hits the photon detector) is proportional to α^5 [for comparison the Born contribution is proportional to α^3, see Eqs. (4) and (5)] and can to high accuracy be neglected.

In this paper we calculate σ_t for the process (1) and the radiative correction to it, using realistic conditions for the tagged photon detector (PD) at the DAΦNE collider. The angular acceptance of the DAΦNE PD covers all phase space except for two symmetrical cones with opening angle $2\theta_0$ along both the electron and the positron beam directions. This kind of angular acceptance is just opposite to that used in Ref. 4, where the PD covered a narrow cone along the electron (or the positron) beam direction. Besides, the actual DAΦNE PD selects events with only one hard photon hitting it, and the corresponding energy cutoff parameter is Δ. Under the DAΦNE conditions one has

$$\theta_0 = 10°, \quad \Delta = 4 \times 10^{-2}, \tag{3}$$

and the radiative-corrected total hadronic cross section will depend on both the angular and energy cutoff parameters.

The Born cross section of process (1) can be written as follows: Refs. 4 and 6

$$d\sigma^B = \int_{\Omega(\theta_0)} \sigma(q^2) \frac{\alpha}{2\pi^2} \frac{(s+t_1)^2+(s+t_2)^2}{t_1 t_2} \frac{d^3k}{s\omega}, \tag{4}$$

where $\Omega(\theta_0)$ spans the angular acceptance of the PD, and $t_{1,2} = -2(kp_{1,2})$. The normalization cross section under the integral sign on the right-hand side of Eq. (4) can be expressed in terms of the ratio R of the total hadronic and muonic cross sections:

$$\sigma(q^2) = \frac{4\pi\alpha^2}{3q^2|1-\Pi(q^2)|^2} R(q^2) \left(1 + \frac{2\mu^2}{q^2}\right) \sqrt{1 - \frac{4\mu^2}{q^2}},$$

$$R(q^2) = \frac{\sigma_t(e^+e^- \to \text{hadrons})}{\sigma_t(e^+e^- \to \mu^+\mu^-)}, \tag{5}$$

where μ is the muon mass. The lepton contribution to the vacuum polarization, $\Pi(q^2)$, is a known function[1] and will not be specified here. The angular integration of Eq. (4) gives

$$d\sigma^B = \frac{\alpha}{2\pi}\sigma(q^2)2\left[\frac{1+(1-x)^2}{x}\ln\frac{1+\cos\theta_0}{1-\cos\theta_0} - x\cos\theta_0\right]dx. \tag{6}$$

In the Born approximation the cross section of the process (1) depends on the angular cutoff parameter only. Looking at Eq. (6), we see that measurement of that cross section at different values of the tagged photon energy fraction x will allow one to extract the quantity $\sigma(e^+e^- \to \text{hadrons})$ at different effective collision energies $s(1-x)$.

High-precision measurement of the total hadronic cross section requires adequate theoretical calculations. These last have to take into account at least the first-order radiative correction (RC). The RC to $d\sigma^B$ includes the contributions due to additional virtual and real soft (with energy less than $\varepsilon\Delta$, i.e., $\omega < \varepsilon\Delta$) photon emission in all angular phase space as well as due to hard ($\omega > \varepsilon\Delta$) photon emission in the region where the PD does not record it.

When calculating the RC to the Born cross section we suppose that $\sigma(q^2)$ is a flat enough function of its argument that the conditions

$$\frac{\Delta}{\sigma(q^2)}\frac{d\sigma}{d\ln(q^2)} \ll 1, \quad \frac{\theta_0^2}{\sigma(q^2)}\frac{d\sigma}{d\ln(q^2)} \ll 1 \tag{7}$$

are satisfied. These conditions permit the application of the soft photon approximation and the quasireal electron method[7] for a description of only the wide-resonance contributions to the cross section.

The virtual and soft photon corrections can be computed using the results of Ref. 8, where one-loop-corrected Compton tensor with a heavy photon was calculated for the scattering channel. In order to reconstruct the corresponding results for the annihilation channel it suffices to make the substitutions (in accordance with the notation used here)

$$p_2 \to -p_2, \quad u \to s, \quad t \to t_1 \tag{8}$$

in all of the formulas of Ref. 8.

Thus the contribution of virtual and soft photon emission to the RC to the Born cross section can be written as follows:

$$d\sigma^{V+S} = \int_{\Omega(\theta_0)}\sigma(q^2)\frac{\alpha^2}{4\pi^3}\left[\rho\frac{(s+t_1)^2+(s+t_2)^2}{t_1t_2} + T\right]\frac{d^3k}{s\omega}, \tag{9}$$

$$\rho = 4(l_s-1)\ln\Delta + 3[l_s + \ln(1-x)] - \frac{\pi^2}{3} - \frac{9}{2}, \quad l_s = \ln\frac{s}{m^2}, \tag{10}$$

$$T = \frac{3}{2} T_g - \frac{1}{8q^2} \{ T_{11}(s+t_1)^2 + T_{22}(s+t_2)^2 + (T_{12}+T_{21})[s(s+t_1+t_2)-t_1 t_2] \}, \quad (11)$$

where m is the electron mass. For the quantities T_g and T_{ik} see Ref. 8, bearing in mind the substitution (8). It must be noted only that under the conditions at DAΦNE one has $|t_{1,2}|_{min} \approx \varepsilon^2 \theta_0^2 \gg m^2$, and one should therefore omit terms proportional to m^2 in both T_g and T_{ik}.

The Born-like structure containing the factor ρ on the right-hand side of Eq. (9) absorbs all infrared singularities via the quantity $\ln\Delta$. In the limiting case

$$|t_1| = 2\varepsilon^2(1-c) \approx \varepsilon^2 \theta_0^2 \ll s, \quad |t_2|; \quad t_2 = -sx, \quad q^2 = s(1-x),$$

which corresponds to events with the tagged photon detected very close to the cutoff angle θ_0 along the electron beam direction, the expression in parentheses on the right-hand side of Eq. (9) reads

$$2\rho \frac{1+(1-x)^2}{x^2(1-c)} + \frac{2}{x(1-c)} \left\{ \frac{1+(1-x)^2}{x} \left[\ln(1-x)\ln\frac{x^2(1-c)}{2(1-x)} - 2f(x) \right] + \frac{2-x^2}{2x} \right\}, \quad (12)$$

$$f(x) = \int_0^x \frac{dz}{z} \ln(1-z), \quad c = \cos\theta,$$

where θ is the angle between vectors $\mathbf{k}$ and $\mathbf{p}_1$. For events with the recorded photon very close to the cutoff angle θ_0 along the positron beam direction, one must change c in (12) to $-c$.

To compute the RC due to an invisible hard photon radiated along the electron beam direction inside a cone with opening angle $2\theta_0$ we can use the quasireal electron method.[7] In accordance with this method the corresponding contribution to the cross section has the form

$$d\sigma_1^H = \int d\sigma^B(p_1 - k_1, k, p_2) dW_{p_1}(k_1), \quad (13)$$

where $d\sigma_1^H$ is the cross section of the process

$$e^-(p_1) + e^+(p_2) - \gamma(k) - \gamma(k_1) \rightarrow \gamma^* \rightarrow H(q), \quad (14)$$

provided that the additional hard photon $\gamma(k_1)$ is emitted along the electron beam direction.

The expression for the radiation probability $dW(k_1)$ is well known,[7] and under the DAΦNE conditions it may be written as follows:

$$dW(k_1) = \frac{\alpha}{2\pi} P\left(1-z, \ln\frac{\varepsilon^2 \theta_0^2}{m^2}\right) dz, \quad P(1-z,L) = \frac{1+(1-z)^2}{z} L - \frac{2(1-z)}{z}, \quad (15)$$

where z is the energy fraction of the invisible photon, and we use the approximation $2(1-\cos\theta_0) = \theta_0^2$ in the argument of the logarithm.

The shifted Born cross section on the right-hand side of Eq. (13) is given by the formula

$$d\sigma^B(p_1-k_1,k,p_2)=\int_{\Omega(\theta_0)}\frac{\alpha}{2\pi}\sigma(q_1^2)\frac{(1-z)^2(s+t_1)^2+[(1-z)s+t_2]^2}{(1-z)^2t_1t_2}\frac{d^3k}{s\omega}, \quad (16)$$

$$q_1=(1-z)p_1+p_2-k.$$

After integration over the invisible photon energy fraction z on the right-hand side of Eq. (13), we obtain

$$d\sigma_1^H=\frac{\alpha}{2\pi}\int_\Delta^{z_m}dz\, P\left(1-z,\ln\frac{\varepsilon^2\theta_0^2}{m^2}\right)d\sigma^B(p_1-k_1,k,p_2), \quad (17)$$

where the upper limit of integration is defined by the condition $q_1^2\geq 4m_\pi^2$ (m_π is the pion mass) and reads

$$z_m=\frac{2(1-x-\delta)}{2-x(1-c)}, \quad \delta=\frac{4m_\pi^2}{s}.$$

The corresponding expression for $d\sigma_2^H$, when the additional invisible hard photon is emitted along the positron beam direction, can be obtained from Eq. (17) by the substitutions $p_1\leftrightarrow p_2$ in $d\sigma^B$ and $c\rightarrow -c$ in z_m. Because the angular acceptance of the DAΦNE PD is symmetrical respect to the substitution $c\rightarrow -c$, one has $d\sigma_1^H=d\sigma_2^H$, and the full RC to the Born cross section reads

$$d\sigma^{RC}=d\sigma^{V+S}+2d\sigma_1^H. \quad (18)$$

It is useful to rewrite the function $P(1-z,L)$, where $L=l_s+\ln(\theta_0^2/4)$, that enters into $d\sigma_1^H$ in the following form:

$$P(1-z,L)=P_1(1-z,L)-2G-\delta(z)\left[\left(\frac{3}{2}+2\ln\Delta\right)L-2\ln\Delta\right], \quad (19)$$

$$P_1(1-z,L)=\left[\frac{1+(1-z)^2}{z}\theta(z-\Delta)+\delta(z)\left(\frac{3}{2}+2\ln\Delta\right)\right]L,$$

$$G=\frac{1-z}{z}\theta(z-\Delta)+\delta(z)\ln\Delta,$$

where the quantity $(\alpha/2\pi)P_1(y,L)$ is the well-known first-order electron structure function,[9] and simultaneously suppose the lower limit of the z integration in $d\sigma_1^H$ to be equal to zero. Then the measured cross section of the process (1) under the DAΦNE conditions can be written as follows:

$$d\sigma=d\sigma^B(p_1,k,p_2)\left\{1+\frac{\alpha}{2\pi}\left[(3+4\ln\Delta)\ln\frac{4}{\theta_0^2}+3\ln(1-x)-\frac{\pi^2}{3}-\frac{9}{2}\right]\right\}+\frac{\alpha}{2\pi}$$

$$\times\left\{\frac{\alpha}{2\pi^2}\int_{\Omega(\theta_0)}\sigma(q^2)T\frac{d^3k}{s\omega}+2\int_0^{z_m}dz[P_1(1-z,L)-G]d\sigma^B[(1-z)p_1,k,p_2]\right\}.$$

$$(20)$$

The term containing the product of logarithms of the energy and the angle cutoff parameter arises because we do not permit the additional hard photon to appear inside the PD. We can resum the main contributions on the right-hand side of Eq. (20) in all orders of perturbation theory and write the master formula in the form

$$d\sigma = \int dz_1 \int dz_2 d\sigma^B(z_1,z_2) \Bigg\{ D(z_1,L)D(z_2,L) - \frac{\alpha}{2\pi}[\,\delta(1-z_1)G(1-z_2)$$

$$+ \delta(1-z_2)G(1-z_1)]\Bigg\} \Theta_{12} + d\sigma^B(1,1)\left[\frac{\alpha}{2\pi}\left(3\ln(1-x) - \frac{\pi^2}{3} - \frac{9}{2}\right)\right.$$

$$+ \exp(\beta l_s)\left(1 - \exp\left(\beta \ln\frac{\theta_0^2}{4}\right)\right)\right] + \frac{\alpha^2}{4\pi^2}\int_{\Omega(\theta_0)} \sigma(q^2) T \frac{d^3k}{s\omega},$$

$$d\sigma^B(z_1,z_2) = d\sigma^B(z_1 p_1, k, z_2 p_2), \quad \beta = \frac{2\alpha}{\pi}\left(\frac{3}{4} + \ln\Delta\right), \tag{21}$$

where $D(z,L)$ is the full electron structure function. The theta function Θ_{12} under the integral sign defines the integration limits over variables z_1 and z_2 under the condition

$$(z_1 p_1 + z_2 p_2 + k)^2 \geqslant 4m_\pi^2.$$

The corresponding limits of integration can be written as follows:

$$1 > z_2 > \frac{2\delta + z_1 x(1-c)}{2z_1 - x(1+c)}, \quad 1 > z_1 > \frac{2\delta + x(1+c)}{2 - x(1-c)}. \tag{22}$$

The cross section (21) corresponds to an event selection such that one hard photon with energy fraction x hitting the PD with an arbitrary number of accompanying soft photons with an energy fraction up to Δ for every one inside the PD is included as an event. If we want to select events for which the energy fraction of all soft photons inside PD does not exceed Δ, we have to replace β by

$$\bar\beta = \frac{2\alpha}{\pi}\left(\frac{3}{4} - C + \ln\Delta\right),$$

where C is the Euler constant, and write

$$\frac{1}{\Gamma(1 + (2\alpha/\pi)l_s)} - \frac{\exp(\bar\beta \ln[\,\theta_0^2/4])}{\Gamma(1 + (2\alpha/\pi)L)}$$

instead of $1 - \exp(\beta \ln(\theta_0^2/4))$ on the second line of Eq. (21).

The master formula (21) takes into account only the photonic RC. It can be generalized in such a way to include also the leading corrections due to electron–positron pair production. We will assume that inside the PD only soft pairs (with energy fraction less than Δ) can be present, while outside the PD there can be both soft and hard pairs. In this case the corresponding generalization can be carried out by the insertion of an effective electromagnetic coupling[9] in place of αl_s and αL,

$$\alpha l_s \to -3\pi \ln\left(1 - \frac{\alpha}{3\pi}l_s\right), \quad \alpha L \to -3\pi \ln\left(1 - \frac{\alpha}{3\pi}L\right), \tag{23}$$

in the electron structure functions and exponents on the right-hand side of Eq. (21). In addition to this we have to represent the electron structure function as a sum of nonsinglet and singlet parts.[9] Note that the nonsinglet part can be written in iterative as well as in exponentiated form, whereas the singlet part has only the iterative form. For the electron structure functions see Refs. 9 and 10.

The master formula (21) takes into account the full first-order RC and resums the main contributions in all orders. It is accurate to better than 0.5 percent.

To extract the RC-corrected hadronic cross section from the corresponding experimental data for the DAΦNE collider with an accuracy of a few tenths of one percent, it suffices to use Eq. (20). In this case we can expand the quantity $\sigma(q^2)$ as

$$\sigma(q^2) = \sigma_0(q^2) + \frac{\alpha}{2\pi}\sigma_1(q^2) \tag{24}$$

and obtain σ_0 and σ_1 by application of a simple iterative procedure to Eq. (20), bearing in mind that the cross section on the left-hand side of this equation is measured by experiment. The corresponding equation in the zeroth approximation,

$$d\sigma^{\text{exp}} = \frac{\alpha}{2\pi^2}\int_{\Omega(\theta_0)}\sigma_0(q^2)\frac{(s+t_1)^2+(s+t_2)^2}{t_1 t_2}\frac{d^3 k}{s\omega} \tag{25}$$

allows one to extract the dependence of $\sigma_0(q^2)$ over a wide interval of the variable q^2. In the first approximation the equation for σ_1 reads

$$\int_{\Omega(\theta_0)}\frac{d^3 k}{s\omega}\left\{\left[\sigma_1(q^2)\sigma_0(q^2)\left((3+4\ln\Delta)\frac{4}{\theta_0^2}+3\ln(1-x)-\frac{\pi^2}{3}-\frac{9}{2}\right)\right]\right.$$
$$\times\frac{(s+t_1)^2+(s+t_2)^2}{t_1 t_2}+\sigma_0(q^2)T+2\int_0^{z_m}\sigma_0(q_1^2)[P_1(1-z,L)-G]$$
$$\left.\times\frac{(1-z)^2(s+t_1)^2+[(1-z)s+t_2]^2}{(1-z)^2 t_1 t_2}dz\right\}=0. \tag{26}$$

This equation can be solved numerically for the function $\sigma_1(q^2)$.

[1] D. H. Brown and W. A. Worstell, Phys. Rev. D **54**, 3237 (1996); S. Eidelman *et al.*, Z. Phys. C **67**, 585 (1995).

[2] F. Jegerlehner, *Transparencies of the Workshop on Hadron Production Cross Sections at DAΦNE*, edited by U. V. Hagel, W. Kluge, J. Kühn, and G. Pancheri, Karlsrue, Germany, 1996, Vol. 1, p. 81.

[3] M. W. Krasny, W. Placzek, and H. Spiesberger, Z. Phys. C **53**, 687 (1992); D. Bardin, L. Kalinovskaya, and T. Riemann, Z. Phys. C **76**, 425 (1997); H. Anlauf, A. B. Arbuzov, E. A. Kuraev, and N. P. Merenkov, Phys. Rev. D **59**, 014003 (1999).

[4] A. B. Arbuzov, E. A. Kuraev, N. P. Merenkov, and L. Trentadue, J. High Energy Phys. **12**, 9 (1998).

[5] S. Binner, J. H. Kühn, and K. Melnikov, http://xxx.lanl.gov/abs/hep-ph/9902399.

[6] V. N. Baier and V. A. Khoze, Zh. Éksp. Teor. Fiz. **48**, 1708 (1965) [Sov. Phys. JETP **21**, 1145 (1965)].

[7] V. N. Baier, V. S. Fadin, and V. A. Khoze, Phys. Lett. B **65**, 381 (1973).

[8] E. A. Kuraev, N. P. Merenkov, and V. S. Fadin, Yad. Fiz. **45**, 782 (1987) [Sov. J. Nucl. Phys. **45**, 486 (1987)].
[9] E. A. Kuraev and V. S. Fadin, Yad. Fiz. **41**, 733 (1985) [Sov. J. Nucl. Phys. **41**, 466 (1985)].
[10] M. Skrzypek, Acta Phys. Pol. B **23**, 135 (1992); S. Jadach, M. Skrzypek, and B. F. L. Ward, Phys. Rev. D **47**, 3733 (1993).

On the spontaneous-coherence-transfer-induced sign change of a sub-natural-width nonlinear resonance

A. V. Taĭchenachev,*) A. M. Tumaĭkin, and V. I. Yudin

Novosibirsk State University, 630090 Novosibirsk, Russia

A simple theoretical model is proposed which describes the positive sign of the nonlinear absorption resonances in the experiments of Akul'shin *et al.* [Phys. Rev. A **57**, 2996 (1998)]. An analytical expression for the linear response to a weak probe field is obtained in the weak-saturation limit. It is shown that the positive sign of sub-natural-width resonances is due to the spontaneous transfer of low-frequency coherence from an excited level to the ground state. © *1999 American Institute of Physics.* [S0021-3640(99)00211-X]

PACS numbers: 42.65.−k, 42.50.Gy

1. It is well known that nonlinear interference effects accompanying the resonant interaction of atoms with light can produce interesting and important phenomena, such as electromagnetically induced transparency,[1] coherent population trapping,[2] amplification and generation without inversion,[3] and others. Common to all these phenomena is the appearance of light-induced coherence between the atomic levels in a dipole-forbidden transition. Sub-natural-width nonlinear resonances have recently been observed[4] in absorption at the D_2 line of rubidium under excitation by two codirectional optical waves with a variable frequency difference. It is remarkable that, besides the expected resonances of electromagnetically induced transparency, with negative sign, there were also positive resonances, describing a substantial growth of the absorption. The authors of Ref. 4 later concluded[5] on the basis of experimental results and numerical calculations that positive sub-natural-width absorption resonances arise in a degenerate two-level system when three conditions are satisfied: 1) The total angular momentum of the excited level is greater than the angular momentum in the ground state: $F_e = F_g + 1$; 2) the transition $F_g \rightarrow F_e$ must be a cycling transition; and, 3) the ground-state level must be degenerate, $F_g > 0$. However, the physical reasons for the sign change of the resonance, in our view, remained unexplained.

At the same time, as was shown in Ref. 6, the spontaneous transfer of Zeeman coherence from an excited level to the ground state (spontaneous cascade of coherence) can change the position, width, and amplitude (which is most important in the present context) of nonlinear resonances in probe-field spectroscopy. It is likely that this process is responsible for the sign change of the resonance in Ref. 4. We note that the simple theoretical models (Λ atom, V atom, and others), ordinarily used to describe nonlinear interference effects, neglect the spontaneous cascade of coherence. Rautian's works on
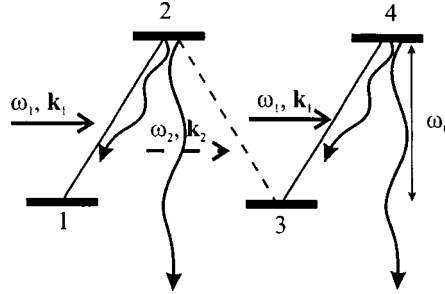
819

FIG. 1. *N* atom. The solid lines (pump field) and the dashed line (probe field) show light-induced transitions. The wavy lines show the two possible channels for spontaneous decay of low-frequency coherence.

the spontaneous transfer of optical coherence are, to all appearances, an exception (see Ref. 7 and the references cited therein).

2. In the present letter we propose a simple theoretical model that admits spontaneous transfer of low-frequency coherence and describes a positive sign of the nonlinear resonances in absorption — an *N* atom. Specifically, we consider an atomic system with four states $|i\rangle$, $i = 1, \ldots, 4$ (see Fig. 1). The odd-numbered states $|1\rangle$ and $|3\rangle$ belong to the nonrelaxing ground state with zero energy. The even-numbered states $|2\rangle$ and $|4\rangle$ form an excited level with energy $\hbar\omega_0$ and spontaneous relaxation rate Γ. All optical transitions $|odd\rangle \rightarrow |even\rangle$ are allowed with the exception of $|1\rangle \rightarrow |4\rangle$, which is forbidden by a selection rule (for example, on the projection of the angular momentum). The *N* atom interacts resonantly with a two-frequency light field:

$$l(\mathbf{r},t) = \mathbf{E}_1 \exp[-i\omega_1 t + i(\mathbf{k}_1 \mathbf{r})] + \mathbf{E}_2 \exp[-i\omega_2 t + i(\mathbf{k}_2 \mathbf{r})] + \text{c.c.} \tag{1}$$

A pump field with amplitude $\mathbf{E}_1$ and frequency ω_1 excites two transitions simultaneously: $|1\rangle \rightarrow |2\rangle$ and $|3\rangle \rightarrow |4\rangle$. A weak probe field $\mathbf{E}_2$ at frequency ω_2 is applied at the transition $|3\rangle \rightarrow |2\rangle$. The Hamiltonian of a free atom can be represented in a basis rotating together with the field as

$$\hat{H}_0 = \hbar\delta_1 |1\rangle\langle 1| + \hbar\delta_2 |3\rangle\langle 3| + \hbar(\delta_2 - \delta_1)|4\rangle\langle 4|, \tag{2}$$

where $\delta_q = \omega_q - \omega_0 - \mathbf{k}_q \cdot \mathbf{v}$ $(q = 1, 2)$ are the detunings with allowance for the Doppler shifts. We use the resonance approximation for the interaction operator $(|\delta_q| \ll \omega_q)$

$$\hat{H}_{AF} = \hbar\Omega_1 \hat{Q}_1 + \hbar\Omega_2 \hat{Q}_2 + \text{h.c.} \tag{3}$$

Here Ω_q is the Rabi frequency, and the operators $\hat{Q}_q$ are given by

$$\hat{Q}_1 = A|2\rangle\langle 1| + |4\rangle\langle 3|,$$

$$\hat{Q}_2 = B|2\rangle\langle 3|, \quad A^2 + B^2 = 1, \tag{4}$$

where the real numbers *A* and *B* determine the relative transition amplitudes (we assume the transition $|3\rangle \rightarrow |4\rangle$ has an amplitude of 1). In the purely radiative relaxation approximation the kinetic equation for the density matrix $\hat{\rho}$ of the atoms has the form

$$\frac{d}{dt}\hat{\rho}+\frac{i}{\hbar}[\hat{H}_0+\hat{H}_{AF},\hat{\rho}]+\frac{1}{2}\Gamma\left\{\sum_{q=1,2}\hat{Q}_q\hat{Q}_q^{\dagger},\hat{\rho}\right\}-b\Gamma\sum_{q=1,2}\hat{Q}_q^{\dagger}\hat{\rho}\hat{Q}_q=\hat{R}\,, \tag{5}$$

where the third term on the left-hand side has the structure of the anticommutator of the state described above and the optical coherences. The last term on the left-hand side corresponds to the transfer of population and low-frequency coherence from the excited level to the ground state. The branching ratio $0\leqslant b\leqslant 1$ sets the probability of an excited atom returning into the initial level. Specifically, $b=1$ for a cycling transition. The right-hand side of Eq. (5) is a source describing external pumping of the levels.

3. As is well known,[8] the work performed by the probe field per unit time is given by the expression $P=2\hbar\omega_2\mathrm{Re}[i\Omega_2^*\rho_{23}]$. A positive sign of P corresponds to absorption of radiation by the medium.

Stationary optical coherence ρ_{23} can be written in the form

$$\rho_{23}=[\Gamma/2-i\delta_2]^{-1}\{-iB\Omega_2(\rho_{33}-\rho_{22})-iA\Omega_1\rho_{13}+i\Omega_1\rho_{24}\}\,. \tag{6}$$

The last two terms (proportional to Ω_1) in braces in Eq. (6) describe the changes occurring in absorption as a result of light-induced low-frequency coherence.

For Λ and V atoms the off-diagonal elements ρ_{13} and ρ_{24} have phases such that the absorption of the probe field decreases at a two-photon resonance $\delta_2=\delta_1$. We note that the corresponding terms have opposite signs. In the case at hand an additional term, due to the spontaneous cascade $\rho_{24}\rightarrow\rho_{13}$ $(d\rho_{13}/dt=\ldots+bA\Gamma\rho_{24})$, appears in the equation for ρ_{13}. Therefore, that phase of the coherence ρ_{24} which gives transparency via the term $i\Omega_1\rho_{24}$ can give an increase of absorption via the term $-iA\Omega_1\rho_{13}$. In what follows we shall use two standard approximations: 1) first order in the probe-field amplitude Ω_2, and 2) weak-saturation limit with respect to the pump field, i.e., $\Omega_1<\Gamma$. Then we replace Eq. (6) by

$$\rho_{23}^{(1)}=[\Gamma/2-i\delta_2]^{-1}\{-iB\Omega_2\rho_{33}^{(0)}-iA\Omega_1\rho_{13}^{(1)}\}\,, \tag{7}$$

where the index in $\rho^{(n)}$ signifies that this element is taken in nth order with respect to Ω_2. Equation (7) is supplemented by the following equations for the first-order coherences:

$$i(\delta_1-\delta_2)\rho_{13}^{(1)}=iB\Omega_2\rho_{12}^{(0)}-iA\Omega_1^*\rho_{23}^{(1)}+i\Omega_1\rho_{14}^{(1)}+bA\Gamma\rho_{24}^{(1)}\,,$$

$$[\Gamma+i(\delta_1-\delta_2)]\rho_{24}^{(1)}=-iB\Omega_2\rho_{34}^{(0)}-iA\Omega_1\rho_{14}^{(1)}+i\Omega_1^*\rho_{23}^{(1)}\,,$$

$$[\Gamma/2+i(2\delta_1-\delta_2)]\rho_{14}^{(1)}=i\Omega_1^*\rho_{13}^{(1)}\,, \tag{8}$$

$$\rho_{12}^{(0)}=\frac{iA\Omega_1^*\rho_{11}^{(0)}}{\Gamma/2+i\delta_1}\,;\quad\rho_{34}^{(0)}=\frac{i\Omega_1^*\rho_{33}^{(0)}}{\Gamma/2+i\delta_1}\,.$$

Here we assume that the term $\hat{R}$ in Eq. (5) is diagonal and therefore contributes in Eq. (8) implicitly via the zeroth-order population $\rho_{ii}^{(0)}$. The following coupled equations for the low-frequency coherences can be obtained from Eqs. (8):

$$\left[\frac{|A\Omega_1|^2}{\Gamma/2-i\delta_2}+\frac{|\Omega_1|^2}{\Gamma/2+i(2\delta_1-\delta_2)}+i(\delta_1-\delta_2)\right]\rho_{13}^{(1)}-bA\Gamma\rho_{24}^{(1)}$$

$$=-\frac{AB\Omega_2\Omega_1^*}{\Gamma/2-i\delta_2}\rho_{33}^{(0)}-\frac{AB\Omega_2\Omega_1^*}{\Gamma/2+i\delta_1}\rho_{11}^{(0)},$$

$$[\Gamma+i(\delta_1-\delta_2)]\rho_{24}^{(1)}-\left\{\frac{A|\Omega_1|^2}{\Gamma/2-i\delta_2}+\frac{A|\Omega_1|^2}{\Gamma/2+i(2\delta_1-\delta_2)}\right\}\rho_{13}^{(1)}$$

$$=\left\{\frac{B\Omega_2\Omega_1^*}{\Gamma/2-i\delta_2}+\frac{B\Omega_2\Omega_1^*}{\Gamma/2+i\delta_1}\right\}\rho_{33}^{(0)}. \tag{9}$$

The right-hand sides of Eqs. (9) describe the appearance of $\rho_{13}^{(1)}$ and $\rho_{24}^{(1)}$ as a result of interference of the transition. The field-induced broadening and optical shifts of the states of the ground level are presented in brackets in the first equation. Equations (9) are not independent because of the second terms, which correspond to spontaneous and induced coherence transfers between the levels, on the left-hand sides. In the low-saturation limit under consideration, the appearance of the coherence $\rho_{24}^{(1)}$ in the equation for $\rho_{13}^{(1)}$ is due to a spontaneous cascade. As one can see from Eq. (9), this process changes the position, width, and amplitude of the nonlinear resonance due to the low-frequency coherence of the ground state. Using Eq. (9) to eliminate the low-frequency coherence from Eq. (7), we obtain the final result for the linear response:

$$\rho_{23}^{(1)}=\frac{-iB\Omega_2}{\Gamma/2-i\delta_2}\left\{\rho_{33}^{(0)}\right.$$

$$+\frac{(b-1)\rho_{33}^{(0)}|A\Omega_1|^2}{|A\Omega_1|^2(1-b)+|\Omega_1|^2(1-bA^2)\dfrac{\Gamma/2-i\delta_2}{\Gamma/2+i\delta_1}+i(\delta_1-\delta_2)(\Gamma/2-i\delta_2)}$$

$$\left.+\frac{(b\rho_{33}^{(0)}-\rho_{11}^{(0)})|A\Omega_1|^2}{|A\Omega_1|^2(1-b)\dfrac{\Gamma/2+i\delta_1}{\Gamma/2-i\delta_2}+|\Omega_1|^2(1-bA^2)+i(\delta_1-\delta_2)(\Gamma/2+i\delta_1)}\right\}, \tag{10}$$

where we have used the approximation $|\delta_1-\delta_2|\ll\Gamma$, since we are interested in a sub-natural-width two-photon resonance.

4. We consider first the case of stationary atoms $\mathbf{v}=0$ (homogeneous broadening). The stationary zeroth-order populations $\rho_{11}^{(0)}$ and $\rho_{33}^{(0)}$ are determined by the balance between pumping and relaxation of the levels and, evidently, they cannot contain structure with width less than Γ. Therefore the last two terms in Eq. (10) are responsible for the sub-natural-width resonances at the frequency difference $\delta_1-\delta_2$. If the pump field is tuned exactly to resonance, $\delta_1=0$, then the sign of the two-photon absorption resonance is determined by the sign of the expression $(2b-1)\rho_{33}^{(0)}-\rho_{11}^{(0)}$, i.e., it depends on the branching ratio and on the populations in the absence of the probe field (see Fig. 2a). For example, if $b=0$, i.e., there is no spontaneous cascade, then the resonance is always
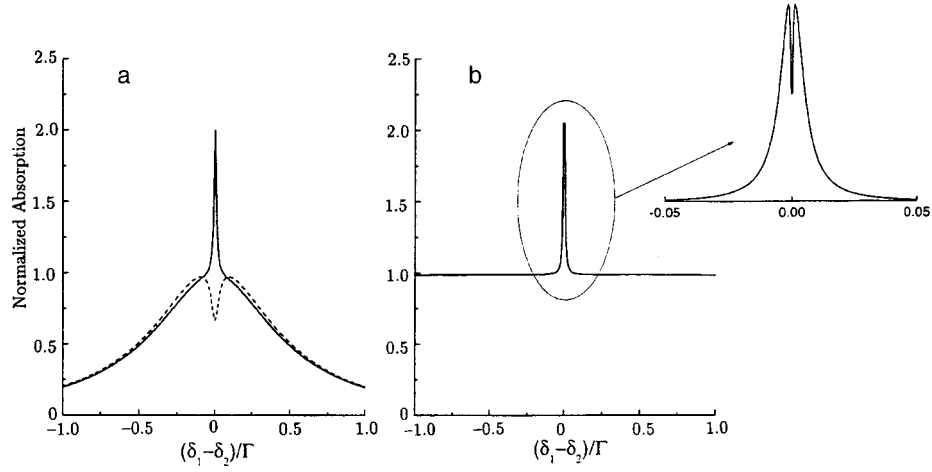
FIG. 2. Probe-field absorption normalized to the linear absorption at line center as a function of the frequency difference for homogeneous broadening $\mathbf{v}=0$ (a) and for Doppler broadening $k\bar{v}=10\Gamma$ (b). The solid (dashed) lines correspond to $b=1$ ($b=0$). The parameters of the pump field are $\delta_1=0$, $\Omega_1=0.1\Gamma$; the other parameters are $A^2=B^2=1/2$ and $\rho_{11}^{(0)}=0$.

negative, which corresponds to electromagnetically induced transparency. In the opposite case of a cycling transition ($b=1$) the resonance is positive, if $\rho_{33}^{(0)}>\rho_{11}^{(0)}$. For $\rho_{11}^{(0)}=0$ the absorption is $(A/B)^2$ times greater than in the linear case.

The position and width of the positive resonance [the last term in Eq. (10)] are determined by the real and imaginary parts of the expression

$$(1-b)\frac{|A\Omega_1|^2}{\delta_1-i\Gamma/2}-(1-bA^2)\frac{|\Omega_1|^2}{\delta_1+i\Gamma/2},$$

which is a linear combination of complex light shifts of the states of the ground level with coefficients that depend on b.

5. We shall now show that the effect does not vanish on averaging over the velocities of the atoms in at least one case of importance for practical applications. Let the codirectional waves have approximately the same Doppler shifts, $\mathbf{k}_1\cdot\mathbf{v}\approx\mathbf{k}_2\cdot\mathbf{v}\approx kv_z$, let the transition be a cycling transition ($b=1$), and let the zeroth-order populations be $\rho_{11}^{(0)}=0$ and $\rho_{23}^{(0)}=f_M(\mathbf{v})$, a Maxwellian velocity distribution. The averaged optical coherence can be expressed in terms of the error function as

$$\langle\rho_{23}\rangle_v=-iB\Omega_2\left\{V(\delta_2)+\frac{|A\Omega_1|^2}{|B\Omega_1|^2+i\Gamma(\delta_1-\delta_2)-(\delta_1-\delta_2)^2}\right.$$

$$\left.\times\left[V(\delta_2)+V\left(-\delta_1+\frac{|B\Omega_1|^2}{\delta_1-\delta_2}\right)\right]\right\},$$

$$V(x) = \frac{\sqrt{\pi}}{k\bar{v}} \exp\left[\left(\frac{\Gamma/2 - ix}{k\bar{v}}\right)^2\right]\left(1 - \mathrm{erf}\left(\frac{\Gamma/2 - ix}{k\bar{v}}\right)\right), \tag{11}$$

where $\delta_q = \omega_q - \omega_0$, $\bar{v} = \sqrt{2k_B T/M}$, and $V(x)$ describes the well-known Voigt contour (the convolution of Lorentzian and Gaussian curves). For a large Doppler width, $k\bar{v} \gg \Gamma$, the absorption of the probe field $\propto \mathrm{Re}\{i\Omega_2^* \langle\rho_{23}\rangle_v\}$ as a function of the frequency difference $\delta_1 - \delta_2$ contains two structures, at the point $\delta_1 - \delta_2 = 0$, with different widths and signs (see Fig. 2b). One structure, described by the Lorentzian $|A\Omega_1|^2/(|B\Omega_1|^2 + i\Gamma(\delta_1 - \delta_2))$, has a width of $|B\Omega_1|^2\Gamma$ and increases absorption. The second structure is associated with the function $V(-\delta_1 + |B\Omega_1|^2/(\delta_1 - \delta_2))$ in Eq. (11) and describes a very narrow dip in the absorption spectrum. This structure, which has a width of $|B\Omega_1|^2/k\bar{v}$, is the result of averaging. For an atom with a fixed velocity $\mathbf{v}$ the effective detuning is $\delta_1 - kv_z$ and, as one can see from Eq. (10), the resonance is optically shifted relative to the point $\delta_1 - \delta_2 = 0$. The sum of such shifted resonances with widths and amplitudes that depend on v_z gives the dip. For $\delta_1 \neq 0$ the resonance becomes asymmetric.

We note that at room temperature the width of the absorption resonance differs by two orders of magnitude from the width of the narrower dip in it. This circumstance can be viewed as a possible reason for the absence of such dips dips in the experiments of Refs. 4 and 5.

6. In conclusion, we note that the *N*-type interaction scheme can be easily organized in real atomic systems. For example, let us consider the cycling transition $F_g = F \rightarrow F_e = F+1$ of the D_2 line of alkali metal atoms that interacts with a circularly polarized (σ_+) pump field. In the absence of a probe field all atoms are transferred to the outermost Zeeman states $|F_g, m_g = F\rangle$ and $|F_e, m_e = F+1\rangle$. If the probe field possesses orthogonal circular polarization (σ_-), then to first order in the probe-field amplitude Ω_2 we have an *N* atom with the states $|1\rangle = |F_g, m_g = F-2\rangle$, $|2\rangle = |F_e, m_e = F-1\rangle$, $|3\rangle = |F_g, m_g = F\rangle$, and $|4\rangle = |F_e, m_e = F+1\rangle$. This scheme was implemented in Refs. 4 and 5 in experiments with circularly polarized waves.

*⁾e-mail: llf@admin.nus.ru

[1] S. E. Harris, Phys. Today **50**(7), 36 (1997).
[2] E. Arimondo, in *Progress in Optics*, edited by E. Wolf (North-Holland, Amsterdam, 1996), Vol. 35, pp. 259–354.
[3] M. O. Scully, Phys. Rep. **219**, 191 (1992); O. Kocharovskaya, Phys. Rep. **175**, 191 (1992).
[4] A. M. Akulshin, S. Barreiro, and A. Lezama, Phys. Rev. A **57**, 2996 (1998).
[5] A. Lezama, S. Barreiro, and A. M. Akulshin, to be published in Phys. Rev. A.
[6] S. G. Rautian, JETP Lett. **60**, 481 (1994).
[7] S. G. Rautian, Zh. Éksp. Teor. Fiz. **115**, 12 (1999) [JETP **88**, 6 (1999)].
[8] S. G. Rautian, G. I. Smirnov, and A. M. Shalagin, *Nonlinear Resonances in Atomic and Molecular Spectra* (Nauka, Novosibirsk, 1979, Chap. 3, Sec. 3).

Translated by M. E. Alferieff

Fluctuation-induced escape from the basin of attraction of a quasiattractor

D. G. Luchinskiĭ*[)]

Department of Physics, Lancaster University, Lancaster, LA1 4 YB, UK

I. A. Khovanov

Saratov State University, 410026 Saratov, Russia

Noise-induced escape from the basin of attraction of a strange attractor (SA) in a periodically excited nonlinear oscillator is investigated. It is shown by numerical simulation methods that escape occurs in two steps: transfer of the system from the SA to a close-lying saddle cycle along several optimal trajectories, and a subsequent fluctuation-induced transfer from the basin of attraction of the SA along a single optimal trajectory. The possibility of using the results of this work to solve problems of the optimal control of switchings from an attractor and for constructing theoretical estimates of the escape probability is discussed. © *1999 American Institute of Physics.* [S0021-3640(99)00311-4]

PACS numbers: 05.45.Gg, 05.40.Ca

The problem of the stability of chaotic attractors in the presence of weak noise is a fundamental unsolved problem of the theory of fluctuations (see, for example, Ref. 1) that is of great importance for practical applications.[2,3] The difficulty in solving this problem stems from, specifically, the fact that the dynamics of a system near a chaotic attractor in the process of large noise-induced deviations from deterministic chaotic trajectories remains obscure.

In the present letter we propose using measurements of the *prehistory probability of fluctuations*[4] for direct experimental investigation of the dynamics of a system near a strange attractor immediately prior to escape from the basin of attraction.

The method is based on the idea of optimal trajectories along which the system fluctuates toward states far from equilibrium.[5] A mathematical variant of these physical ideas are asymptotic formulas, written in terms of rays or wave fronts, for solving the Fokker–Planck equation.[6] The method essentially reduces to following continuously the dynamics of a system and constructing the distribution of all realizations of the fluctuation trajectories of the system that transfer it from a state of equilibrium to a prescribed remote state.[4] The advantages of this approach have been demonstrated previously[7–9] in an investigation of certain fundamental symmetry properties of optimal trajectories and singular characteristics of their distribution.
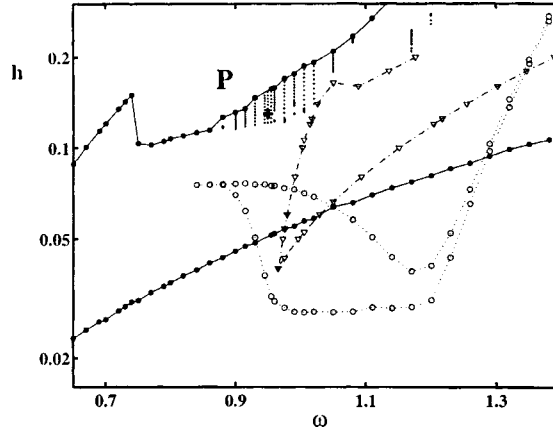
FIG. 1. Phase diagram of the system (1) in the plane of the parameters of the external force. The diagram was obtained by numerical simulation of the system (1) with $\Gamma = 0.05$, $\omega_0 = 0.597$, $\beta = 1$, and $\gamma = 1$. The small crosses show the regions of chaos. The filled dots show the region of coexistence of two attractors corresponding to resonances of period 1 of the system (1). The circles bound the region of hysteresis of creation and vanishing of an attractor corresponding to a resonance of period 2. The triangles show the region of coexistence of two attractors corresponding to a resonance of period 2 (the solid, dot-and-dash, and dashed lines connecting the symbols are drawn to facilitate reading the figure). The working point P with $\omega_f = 0.95$ and $h = 0.13$ shown by the thick cross is chosen in the region of coexistence of the strange attractor and a stable limit cycle corresponding to a resonance of period 1.

A nonlinear oscillator in the presence of noise and an external periodic force was chosen as the model for investigation:

$$\dot{\mathbf{q}} = \mathbf{K}(\mathbf{q},t) + \mathbf{f}(t), \quad \mathbf{K} = \{K_1, K_2\} = \{q_2, -2\Gamma q_2 - \omega_0^2 q_1 - \beta q_1^2 - \gamma q_1^3 + h\cos(\omega_f t)\},$$

$$\mathbf{f}(t) = \{0, \xi(t)\}, \quad \langle \xi(t) \rangle = 0, \quad \langle \xi(t)\xi(0) \rangle = 4\Gamma kT\delta(t), \tag{1}$$

$$\Gamma \ll \omega_f, \quad 9/10 < \beta^2/\gamma\omega_0^2 < 4.$$

For the chosen values of the parameters the potential is a single-well potential ($\beta^2 < 4\gamma\omega_0^2$), and the energy dependence of the oscillation frequency is nonmonotonic ($\beta^2/\gamma\omega_0^2 > 9/10$). This model is encountered in many applications and can be used to perform a theoretical analysis over a large range of the parameters (see, for example, Refs. 10 and 11). It has been shown previously[10] that chaos can arise in the system (1) for comparatively small amplitudes $h \approx 0.1$ of the external force.

A simplified diagram (Fig. 1) shows the stability boundaries of limit cycles of periods 1 and 2 as well as the existence regions of dynamical chaos. A chaotic attractor arises as a result of a cascade of period-doubling bifurcations, and it is therefore a quasiattractor.[12] We note that qualitatively this diagram reproduces the features predicted theoretically for not very different values of the parameters.[10]

The point P in the diagram denotes the regime chosen for investigation, where a SA coexists with a stable limit cycle. This regime is often encountered in applications which are of practical interest.[2,13,14] To study in detail the behavior of the system (1) in this regime, numerical investigations of its dynamics were performed using a fast pseudorandom sequence generator.[15]
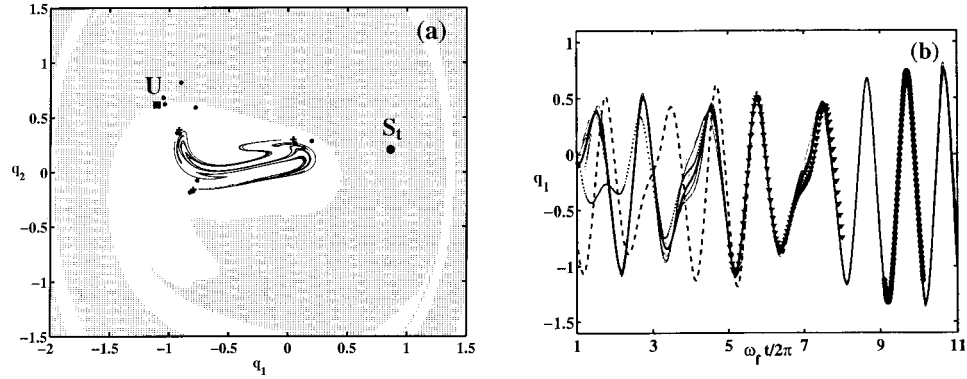
FIG. 2. (a) The hatched and white regions correspond to basins of attraction of a stable limit cycle S_t and a SA in a Poincaré section of the system (1) for $\omega_f t = 0.6\pi$ with parameters corresponding to the point P in the preceding figure. The filled dots show the intersections with a given plane of one of the real escape trajectories of the system from the basin of attraction of the SA. The point U shows an unstable limit cycle lying on the boundary of the basin of attraction of the SA. The crosses correspond to points belonging to the cycle $S3$. (b) The three optimal escape trajectories shown by dashed, solid, and dotted lines have relative probabilities 9.5:4:1, respectively. The triangles and filled dots show one period of an unstable saddle cycle of period 3 ($S3$) and one period of an unstable limit cycle U, respectively. The solid thin lines show 15 real escape trajectories corresponding to the same optimal trajectory.

The basins of attraction of both attractors are shown in Fig. 2a for one of the Poincaré surfaces of section. The symbols S_t and U in the figure denote the stable and unstable limit cycles, respectively. The SA is shown in the figure by dots (the maximum Lyapunov exponent is $\lambda_M = 0.0449$). In the presence of weak noise there is a finite probability of noise-induced transitions between the chaotic attractor and a stable limit cycle. In the figure the filled dots show the intersections of one of the real escape trajectories with the given Poincaré section. The crosses show a saddle cycle of period 3 ($S3$) through which the optimal escape trajectory passes (see below). The multipliers for $S3$ are $\mu_1 = 0.04873 < 1$ and $\mu_2 = 7.608312 > 1$.

The following very simple escape scenario can be expected in the Hamiltonian formalism. Let us consider first the escape of the system from the basin of attraction of a stable limit cycle that is bounded by an unstable limit cycle. In general, escape occurs along a single optimal trajectory $\mathbf{q}_{opt}(t)$ connecting the two limit cycles. To determine $\mathbf{q}_{opt}(t)$ and the escape probability P in the limit $T \to 0$ we can seek the solution of the Fokker–Planck equation corresponding to the system (1) in a form similar to the WKB approximation[6] (see also Refs. 4–9, 17, and 18):

$$P(\mathbf{q},t) \approx C \exp(-S(\mathbf{q},t)/kT), \quad T \to 0, \tag{2}$$

where C is a prefactor and $S(\mathbf{q},t)$ plays the role of an ''activation energy'' of fluctuations at the point $\mathbf{q}$ in the space of states of the system and is a periodic function of time for periodically excited systems. Substituting the function (2) into the Fokker–Planck equation and expanding in powers of T shows that, to leading order in the expansion, $S(\mathbf{q},t)$ satisfies the Hamiltonian–Jacobi equation with the so-called Wentzel–Freidlin Hamiltonian H:[6]

$$\dot{S} + H\left(\mathbf{q}, \frac{\partial S}{\partial \mathbf{q}}\right) = 0, \quad H = \frac{1}{2}p_2^2 + p_1 K_1 + p_2 K_2, \quad \mathbf{p} = \{p_1, p_2\} = \frac{\partial S}{\partial \mathbf{q}}. \tag{3}$$

The trajectory $\mathbf{q}_{opt}(t)$ is determined by minimizing S on the set of all classical deterministic trajectories determined by the Hamiltonian H, that start on a stable limit cycle as $t \to -\infty$ and terminate at an unstable limit cycle as $t \to \infty$. That is, $\mathbf{q}_{opt}(t)$ is a heteroclinic trajectory of the system (3) with minimum action $S_a = \min S$, where the minimum is understood in the sense indicated, and the escape probability assumes the form $P \approx \exp(-S_a/kT)$. We note that the existence of optimal escape trajectories and the validity of Eqs. (2) and (3) have been confirmed experimentally for a number of nonchaotic systems (see Refs. 7–9 and the references cited therein).

If the noise is weak, then the probability $P(\mathbf{q}_{opt}, t)$ of escape along the optimal trajectory is exponentially small, but it is exponentially greater than the escape probability along any other trajectory, including along other heteroclinic trajectories of the system (3).

Since the basin of attraction of the SA is bounded by an unstable limit cycle U, the situation near U remains qualitatively the same and the escape trajectory remains unique in this region. However, the situation is different near a chaotic attractor. In this region it is virtually impossible to analyze the Hamiltonian flux of the additional system (3), and no predictions have been made about the character of the distribution of the optimal trajectories near a SA. The simplest scenario is that an optimal trajectory approaching the boundary of a chaotic attractor is smeared into a ''cometary tail'' and is lost, merging with the boundary of the attractor.

However, statistical analysis of real fluctuation-induced escape trajectories gives a more detailed picture of the noise-induced escape from a chaotic attractor.

Several thousands of real escape trajectories of the system (1) from the basin of attraction of a SA in various operating regimes were investigated. The typical situation is displayed in Fig. 2b for system parameters corresponding to the point P in Fig. 1. Fifteen real escape trajectories corresponding to the same optimal trajectory are presented in Fig. 2b as an example. All trajectories are made to coincide in time at a single characteristic point corresponding to the passage through a saddle cycle of period 3 (triangles) accompanying a transition from chaotic to regular motion. It is evident that all real trajectories pass through the immediate neighborhood of the optimal trajectory in a band with half width $\propto \sqrt{kT}$ (we note that the space of states of the system (1) is three-dimensional and the trajectories form in this space a narrow tube with radius $\propto \sqrt{kT}$; for simplicity, only the projection on the plane ($\omega_f t$, x) is shown in the figure). Therefore there is a possibility of determining optimal escape trajectories experimentally by simple averaging.

The three experimentally determined optimal trajectories of escape from the basin of attraction of a SA are shown in Fig. 2b (solid, dotted, and dashed lines). The same figure also shows one period for the numerically determined cycle $S3$ (triangles) located near the SA and one period for an unstable limit cycle (filled dots) bounding the basin of attraction of the SA. Analysis of the optimal trajectories shows the following features of the fluctuation-induced escape from the boundary of the basin of attraction of the SA: (i) the system escapes from the SA along several optimal trajectories; (ii) these trajectories merge into a single trajectory approaching the saddle cycle $S3$ located near the SA; (iii)

the subsequent escape occurs along a single optimal escape trajectory connecting $S3$ and an unstable limit cycle U, located at the boundary of the basin of attraction of the SA.

Apparently, of all unstable saddle cycles the cycle $S3$ is closest with respect to the action variable to the boundary of the basin of attraction of the SA and in this sense it can be regarded as the boundary of the SA. Moreover, the analysis performed makes it possible to divide the escape of the system from the basin of attraction of the SA conventionally into two stages: the transition SA→$S3$ along three optimal trajectories followed by fluctuation-induced escape $S3$→U along a single optimal trajectory. The number of optimal trajectories of the transition SA→$S3$ depends on the choice of the working point. One to three escape trajectories for operation in various regimes were observed experimentally. The escape probabilities along different trajectories are different (see, for example, the caption to Fig. 2b).

This escape scenario opens up the fundamental possibility of constructing analytic estimates of the probability $P(q)$ of the system switching from the SA to a stable limit cycle in addition to the methods proposed previously for estimating this probability numerically.[1,16] To a first approximation $P(q)$ can be estimated as the probability of escape from $S3$. Corrections can be calculated, keeping in mind the fact that the transition SA→$S3$ occurs along three optimal trajectories (see Fig. 2b). It is likely that the system passes from the SA to $S3$ via saddle cycles built into the structure of the SA. Of all saddle cycles the system chooses only several cycles, closest to $S3$ with respect to the action variable. The hierarchy of saddle cycles of the system along the action variable can be determined experimentally, if the corresponding realizations of the external random force are analyzed simultaneously with the statistical analysis of the dynamical trajectories of the system (see, for example, Ref. 8). A preliminary analysis shows that for the system parameters chosen the transition SA→$S3$ occurs mainly from a saddle cycle of period 5.

We note that the possibility of evaluating analytically the probabilities of transitions between limit cycles is itself linked with the need to generalize the recently proposed theory of logarithmic susceptibility[17,18] to systems with limit cycles.[19] However, in so doing there arises the additional problem of determining the form of the limit cycles.

In summary, the results of numerical experiments show that analysis of the fluctuation-induced escape of a system from the basin of attraction of a quasiattractor (in the case of nonfractal boundaries) reduces to analyzing the probability of transitions between several saddle cycles. The results obtained agree with the well-known conclusion that the chaotic behavior of low-dimensional dynamical systems is largely determined by the position and stability properties of unstable cycles built into the chaotic structures (see, for example, Refs. 20–22).

An additional statistical analysis of those realizations of the external random force which correspond to the system escaping from the basin of attraction of the SA makes it possible to find a deterministic optimal force (in the sense of minimum action) that switches the system from a regime of dynamical chaos into a periodic operating regime. Therefore the proposed method can be used as a new experimental approach to solving the problem of the optimal control of switchings of a system between chaotic and stable operating regimes in the presence of noise. This possibility will be investigated experimentally and numerically in future publications.

*)e-mail: d.luchinsky@lancaster.ac.uk

[1] R. Graham, A. Hamm, and T. Tel, Phys. Rev. Lett. **66**, 3089 (1991).

[2] R. Kautz, Phys. Lett. A **125**, 315 (1987).

[3] R. L. Kautz, Rep. Prog. Phys. **59**, 935 (1996).

[4] M. I. Dykman *et al.*, Phys. Rev. Lett. **68**, 2718 (1992).

[5] L. Onsager and S. Machlup, Phys. Rev. **91**, 1505 (1953).

[6] M. I. Freidlin and A. D. Wentzel, *Random Perturbations in Dynamical Systems* (Springer, New-York, 1984); M. I. Freidlin and A. D. Wentzel, Usp. Mat. Nauk **25**, 3 (1970).

[7] D. G. Luchinsky *et al.*, Phys. Rev. Lett. **79**, 3117 (1997).

[8] D. G. Luchinsky, P. V. E. McClintock, and M. I. Dykman, Rep. Prog. Phys. **61**, 889 (1998).

[9] D. G. Luchinsky and P. V. E. McClintock, Nature (London) **389**, 463 (1997).

[10] S. M. Soskin *et al.*, in *Proceedings of the 14th International Conference on Noise in Physical Systems and 1/f Fluctuations*, IMEC, edited by C. Claeys and E. Simoen (World Scientific, Leuven, Belgium, 1997), p. 351.

[11] R. Mannella, S. M. Soskin, and P. V. E. McClintock, Int. J. Bifurc. Chaos **8**, 701 (1998).

[12] V. S. Afraimovich, in *Nonlinear and Turbulent Processes in Physics* (Gordon and Breach, New York, 1984), p. 1133.

[13] H. M. Gibbs, F. A. Hopf, D. L. Kaplan, and R. L. Shoemaker, J. Opt. Soc. Am. **71**, 367 (1981).

[14] J. A. Blackburn, H. J. T. Smith, and N. Gronbech-Jensen, Phys. Rev. B **53**, 14546 (1996).

[15] G. Marsaglia and W.-W. Tsang, SIAM (Soc. Ind. Appl. Math.) J. Sci. Stat. Comput. **5**, 349 (1984).

[16] P. Jung and P. Hänggi, Phys. Rev. Lett. **65**, 3365 (1990).

[17] M. I. Dykman, H. Rabitz, V. N. Smelyanskiy, and B. E. Vugmeister, Phys. Rev. Lett. **79**, 1178 (1997).

[18] V. N. Smelyanskiy, M. I. Dykman, H. Rabitz, and B. E. Vugmeister, Phys. Rev. Lett. **79**, 3113 (1997).

[19] M. I. Dykman and V. N. Smelyanskiy, private communication.

[20] D. Auerbach *et al.*, Phys. Rev. Lett. **58**, 2387 (1987).

[21] C. Grebogi, E. Ott, and J. A. Yorke, Phys. Rev. A **37**, 1711 (1988).

[22] P. Schmelcher and F. K. Diakonos, Phys. Rev. Lett. **78**, 4733 (1997).

Fourth-order interference between independent biphotons

A. V. Burlakov, D. N. Klyshko, S. P. Kulik, and M. V. Chekhova

M. V. Lomonosov Moscow State University,[*)] *119899 Moscow, Russia*

The interference of biphotons emitted during collinear parametric scattering from two spatially separated regions is investigated experimentally and theoretically. It is shown that in this case the phase of the interference is determined by the pump wavelength and there is no need to equalize the optical paths for radiation from different regions. © *1999 American Institute of Physics.* [S0021-3640(99)00411-9]

PACS numbers: 42.50.−p

The question of whether or not it is possible to observe interference of independent photons has been discussed repeatedly (see, for example, the review in Ref. 1). Such interference of independent photons can be pictured as the interference of classical wave packets. The quantum properties of the light are then manifested only in detection as discreteness of the photocurrent.[2] However, such a pictorial representation of the field as a collection of packets with definite *a priori* properties is inapplicable for describing certain ''nonclassical'' optical effects (see Refs. 3–5). The nonclassical nature of light is most evident in experiments with biphotons and interference which is of fourth order in the field amplitude (it is also called interference of intensities — in contrast to ordinary interference which is of second order in amplitude). A biphoton is a pair of photons which are correlated with respect to their times of creation and, possibly, their polarization, direction, and energy. We shall be interested in the degenerate case where the average energy, direction, and polarization of the photons are identical, i.e., the photons in a pair are indistinguishable (more accurately, they are not distinguished by the detectors employed).

We describe in this letter an experiment on the observation of fourth-order interference between two biphotons which are emitted from two separated nonlinear regions as a result of parametric scattering of a general coherent and classical pump. The scattered field is described by the product of two wave functions, which gives two independent statistics for the observed probabilities and moments, so that the biphotons can be considered as independent in some sense. Fourth-order interference in nonlinear parametric scattering in two crystals (with four beams instead of two) has been analyzed in Refs. 6 and 7 and observed in Ref. 8, but a fundamental feature of the effect was that the optical paths of the signal and idler radiation had to be equalized to within their coherence length, which was several tens of microns. It is shown in the present letter that equalization of the optical paths for radiation from different regions is not required for interfer-
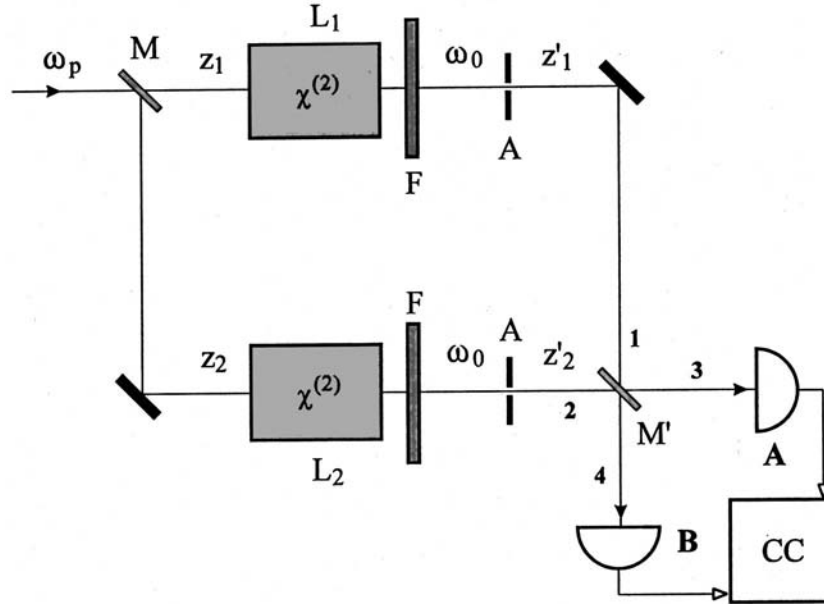
FIG. 1. Schematic diagram for observing interference of independent biphotons in the Mach–Zehnder scheme. ω_p — pump frequency, $\omega_0 = \omega_p/2$. M and M' — beam splitters, CC — coincidence circuit.

ence of biphotons emitted from two spatially separated regions in the collinear regime.

The collinear regime for scattering in two crystals has been used previously in Ref. 9, where the effect of the spatial distribution of the pump on fourth-order interference was studied.

A schematic diagram of the experiment is presented in Fig. 1. A monochromatic laser pump beam with frequency ω_p is split by a beam splitter M and passes through two transparent crystals with quadratic nonlinearity $\chi^{(2)}$ and is then absorbed by the filters F. The crystals spontaneously emit polarized biphotons with average frequency $\omega_0 = \omega_p/2$. The apertures A select a narrow solid angle with one transverse mode in the direction of the pump wave vector $\mathbf{k}_p$, so that the condition of collinear phase matching $\mathbf{k}_p = 2\mathbf{k}(\omega_0)$ is satisfied inside the crystals. Biphotons are emitted at random independent times, but nonetheless they interfere with one another in fourth order at the exit beam splitter M'. This interference is observed with a coincidence circuit CC.

We proceed from the effective Hamiltonian

$$H = -\frac{1}{2} \int d^3 r [\chi_1 E_{p1}(E_1^{(-)})^2 + \chi_2 E_{p2}(E_2^{(-)})^2] + \text{h.c} \equiv H_1 + H_2. \tag{1}$$

Here the nonlinearities χ_i are different from zero only inside the crystals; the indices $i = 1,2$ refer to the crystals and the spontaneous fields emitted by them with frequencies less than ω_p; the complex amplitudes of the pump in the crystals are $E_{pi}(\mathbf{r},t)$ and the parameters of the crystals can be different; $E_i(\mathbf{r},t)$ is the scattering field operator. It follows from Eq. (1) that to first order in $\chi_i E_{pi}$

$$|\psi\rangle=\left(1-\frac{i}{\hbar}\int dtH(t)\right)|0\rangle=|0\rangle+\frac{i}{2\hbar}\int dt\int d^3r\sum_i \chi_i E_{pi}(E_i^{(-)})^2|0\rangle.\qquad(2)$$

In the diffractionless approximation, we consider plane waves propagating parallel to $\mathbf{k}_p$ and perpendicular to the nonlinear layer. In the spectral representation

$$E_i^{(-)}(z,t)\propto a^+(z,t)\equiv\frac{1}{\sqrt{2\pi}}e^{i\omega_0 t}\int d\Omega a_i^+(\omega_0+\Omega)e^{i\Omega t-ik_i'(\omega_0+\Omega)z},\qquad(3)$$

where $\omega_0\equiv\omega_p/2$, $a_i(\omega_0+\Omega)$ is an operator annihilating a photon in a mode with frequency $\omega=\omega_0+\Omega$ and $k_i'(\omega_0+\Omega)$ is the wave vector, the primes distinguish wave vectors inside a crystal, and inconsequential constants are dropped (see Ref. 10 for a more detailed discussion). As a result,

$$|\psi\rangle=|0\rangle+\frac{1}{2}\sum_i \chi_i E_{pi}e^{i\phi_{pi}}\int d\Omega a_i^+(\omega_0+\Omega)a_i^+(\omega_0-\Omega)$$

$$\times\int_{z_i}^{z_i+L_i}dz\exp\{iz[k_{pi}'-k_p'(\omega_0+\Omega)-k_i'(\omega_0-\Omega)]\}|0\rangle,\qquad(4)$$

where $[z_i,z_i+L_i]$ are the limits of the ith crystal, $\phi_{pi}\equiv k_p z_i$ is the phase of the pump field at a distance z_i from the entrance mirror, the function $k'(\omega)$ describes the dispersion of ordinary waves in the nonlinear crystal, k_p is the pump wave vector (the pump wave inside the crystals is an extraordinary wave, and $k_{pi}'\approx 2k_i'(\omega_0)$). In the stationary state only components with $\omega_0+\Omega$ and $\omega_0-\Omega$ are correlated. We introduce

$$|\Omega\rangle_i\otimes|-\Omega\rangle_i\equiv a_i^+(\omega_0+\Omega)a_i^+(\omega_0-\Omega)|0\rangle,$$

$$\Delta k_i(\Omega)\equiv k_{pi}'-k_i'(\omega_0+\Omega)-k_i'(\omega_0-\Omega),$$

$$f_i(\Omega)\equiv\frac{1}{L_1}\int_{z_i}^{z_i+L}dze^{i\Delta k_i(\Omega)z},$$

$$F_i(\Omega)=F_i(-\Omega)\equiv 2\pi c^{-1}\omega_0\chi_i E_{pi}L_i f_i(\Omega)\equiv\Gamma_i f_i(\Omega).$$

Then Eq. (4) becomes

$$|\psi\rangle=|0\rangle+\frac{1}{2}\int d\Omega[F_1(\Omega)e^{i\phi_{p1}}|\Omega\rangle_1\otimes|-\Omega\rangle_1+F_2(\Omega)e^{i\phi_{p2}}|\Omega\rangle_2\otimes|-\Omega\rangle_2].\qquad(5)$$

Here Γ_i is the parametric gain ($|\Gamma_i|\ll 1$), and the function $f_i(\Omega)$ describes the frequency dependence of the gain. The symbol $|\Omega\rangle_i\equiv|1\rangle_{i\Omega}\equiv a_i^+(\Omega)|0\rangle$ signifies a one-photon state of a longitudinal mode with frequency $\omega_0+\Omega$ of the beam i.

If the spectral composition of the beams is neglected, then the state of the field can be represented in the two-mode approximation as

$$|\psi\rangle=|0\rangle_1\otimes|0\rangle_2+C_1|2\rangle_1\otimes|0\rangle_2+C_2|0\rangle_1\otimes|2\rangle_2\approx(|0\rangle_1+C_1|2\rangle_1)(|0\rangle_2+C_2|2\rangle_2),$$
$$(6)$$

where $C_i = \frac{1}{2}\Gamma_i$ and $|C_i| \ll 1$. The relative contributions C_i of the crystals and their phases can be regulated by the pump amplitudes E_{pi}. If the vacuum components are neglected, $|\psi\rangle$ describes two-photon states of two independent modes; the probability of observing two photons in one of the modes is 1 (instead of $|C_i|^2 \ll 1$).

From Eq. (5) we find the second moments of the scattering field

$$N_i(\Omega) \equiv \langle a_i(\Omega)^+ a_i(\Omega)\rangle = |F_i(\Omega)|^2,$$

$$\langle a_i(\Omega)a_j(\Omega')\rangle = \langle 0|a_i(\Omega)a_j(\Omega')|\psi\rangle = F_i(\Omega)e^{i\phi_{pi}}\delta_{ij}\delta(\Omega+\Omega'). \tag{7}$$

The quantities found refer to the coordinate $z_i + L_i$ at the exit of the ith crystal. Propagation to the second beam splitter M' adds the phases $k_\Omega z_i'$, where z_i' is the distance from the exit faces of the crystals to M' (see Fig. 1). In free space $k_\Omega = (\omega_0 + \Omega)/c$, so that $k_\Omega + k_{-\Omega} = 2k_0 = k_p$, i.e., taking account of the paths z_i' gives frequency-independent phase factors $\exp(ik_p z_i') \equiv \exp(i\phi_i')$ in the correlation functions $\langle a_i(\Omega)a_i(\Omega')\rangle$. Thus, as they propagate, two-photon wave packets acquire additional phases $\exp(i\phi_i')$. As a result,

$$\langle a_i(\Omega)a_i(\Omega')\rangle = F_i(\Omega)e^{i\phi_i}\delta(\Omega+\Omega'), \tag{8}$$

where $\phi_i \equiv k_p(z_i + z_i')$. When a crystal is displaced along the pump beam, the sum $z_i + z_i'$ remains unchanged, i.e., the longitudinal position of the crystals does not influence the observed effects (in the approximation of an infinite coherence length of the pump). Interference is determined by the difference of the lengths of the interferometer arms — the two paths between the beam splitters M and M', as in an ordinary Mach–Zehnder interferometer.

The Fourier transforms of the spectral moments determine the correlation function

$$F_i(t,t') \equiv \langle a_i(t)a_i(t')\rangle = \frac{1}{2\pi}e^{-i\omega_p(t+t')}\int d\Omega\, e^{-i\Omega(t-t')}F_i(\Omega). \tag{9}$$

The function $F_i(t,t') = F_i(t',t)$ can be called a two-photon wave packet or the effective field of a biphoton.[10] The dependence on two times shows that the scattering field is nonstationary — the statistics varies periodically with the pump frequency. If homodyne detection is excluded from consideration, then the phase factor $\exp[-i\omega_p(t+t')]$ plays no role, and we omit it in what follows. Then the correlation function $\langle a_i(t)a_i(t')\rangle$ depends only on the difference $\tau = t - t'$ of the photon detection times:

$$\langle a_i(t)a_i(t')\rangle = F_i(\tau)e^{i\phi_i} = \frac{1}{2\pi}e^{i\phi_i}\int d\Omega\, e^{-i\Omega\tau}F_i(\Omega). \tag{10}$$

According to Glauber[11] the function $G_i(\tau) = G_i(-\tau) = \langle a_i^+(\tau)a_i^+(0)a_i(0)a_i(\tau)\rangle$ in the one-mode detection approximation is proportional to the probability of detecting two photons in the beam i at times t and $t+\tau$. For a two-mode wave function (5) one has $G_i(\tau) = |F(\tau)|^2$. The function $G_i(t)$ can be measured, for example, by the Brown–Twiss method.[12]

We now take account of the effect of a 50% beam splitter M':

$$a_3(t) = [a_1(t) - a_2(t)]/\sqrt{2}, \quad a_4(t) = [a_1(t) + a_2(t)]/\sqrt{2}, \tag{11}$$

where a_3 and a_4 are operators annihilating photons in the corresponding beams after the beam splitter.

The detected number of counts in ideal detectors A and B becomes

$$R_A = \langle a_3^+(t)a_3(t)\rangle = \frac{1}{2}(R_1+R_2) \quad \text{and} \quad R_B = \langle a_4^+(t)a_4(t)\rangle = \frac{1}{2}(R_1+R_2) = R_A. \tag{12}$$

Therefore since the beams 1 and 2 are mutually incoherent in second order ($\langle a_1^+ a_2\rangle = 0$), the ordinary interference of fields in beams 3 and 4 is not observed.

Further, according to Eq. (11)

$$F_{34}(\tau) = \langle a_3(0)a_4(\tau)\rangle = \frac{1}{2}(F_1(\tau)e^{i\phi_1} - F_2(\tau)e^{i\phi_2}), \tag{13}$$

where $\phi_i \equiv k_p(z_i+z_i')$. The probability of detecting one photon in each of the exit beams at times t and $t+\tau$ is determined by the (even) correlation function

$$G_{34}(\tau) = |F_{34}(\tau)|^2 = \frac{1}{4}[|F_1(\tau)|^2 + |F_2(\tau)|^2 - 2\mathrm{Re}(F_1(\tau)F_2^*(\tau)e^{i\phi})], \tag{14}$$

where $\phi \equiv \phi_i - \phi_2$. Therefore this probability oscillates as a function of ϕ. Two-photon packets from each crystal ''remember'' the pump phase. This is manifested as beats of the probability G_{34} with period equal to the pump wavelength λ_p — just as for ordinary interference of fields in a Mach–Zehnder interferometer. This effect can be called *interference of independent biphotons*. We underscore the main feature of the function (14) — *the visibility of the interference pattern does not depend on the spatial position of the crystals and mirrors,* which therefore can be chosen arbitrarily (in the approximation of an infinite coherence length of the pump).

If the crystals and the pump fields in them are identical, then $F_1(\tau) = F_2(\tau) \equiv F(\tau)$ and

$$G_{34}(\tau) = |F(\tau)|^2 \sin^2(\phi/2). \tag{15}$$

Young's interference scheme was used in the real experiment (Fig. 2). In the present case this scheme is completely analogous to the Mach–Zehnder arrangement from the standpoint of the theoretical description as well as the physical essence of the observed effects. The only characteristic feature is that the detecting apparatus must be placed in the zone of diffraction superposition of the biphoton fields emitted by the two scattering regions, just as for ordinary second order interference in Young's scheme (in the Mach–Zender scheme the superposition is accomplished using a beam splitter). The choice of the present scheme was based on its main advantage — one crystal is used instead of two and the resulting simplicity of the experiment. The radiation from a He–Cd laser with one transverse mode, wavelength 0.325 μm, power 5 mW, and coherence length 15 cm was used as the pump. An opaque screen with two slits (the width of each slit $a = 130$ μm and the distance between the centers of the slits $b = 330$ μm) was placed directly in front of a lithium iodate crystal 15 mm long, cut out at an angle of 58° with respect to the optic axis (this corresponded to degenerate collinear matching of the scattering). A filter F (BS-8), placed immediately after the crystal, completely absorbed the pump and transmitted visible-range radiation. For type-I matching the polarizations of the scattered
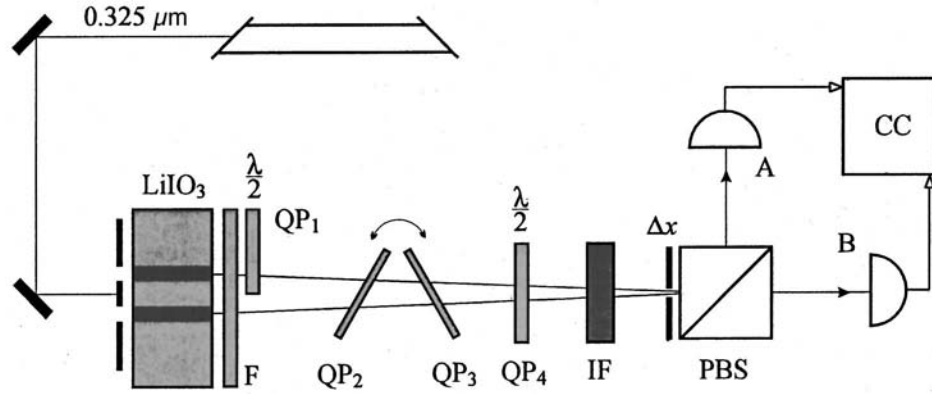
FIG. 2. Experimental setup for observing fourth-order interference in Young's scheme. The half-wave plate QP_1 introduces an initial optical path difference of 460 μm for the signal fields emitted by the first and second scattering regions, with a coherence length of 45 μm.

radiation in the signal and idler modes are identical, so that two beams of biphotons with the same polarization (horizontal) were obtained at the exit of the crystal. A Brown–Twiss interferometer with a polarized beam splitter *PBS* was used to check Eq. (17). A relative phase change of the radiation from the two regions of interaction was accomplished with four phase plates QP. The first half-wave plate (QP_1) was placed immediately after the crystal in one of the biphoton beams, so as to rotate its polarization by 90° (vertically). Two identical plates QP_2 and QP_3 with thickness $d = 820$ μm, cut out of crystalline quartz, served for smooth shifting of the phases between the beams. The ''fast'' (and ''slow'') axes, respectively, of these plates were oriented along the directions of the polarization vectors of the incident radiation. The phase difference δ was determined by the rotation angle α, the birefringence Δn, and the thickness d of the plates:

$$\delta = 2d[(1 - [\sin(\alpha)/n]^2)^{-1/2} - 1]\Delta n, \quad \Delta n(0.65 \ \mu\text{m}) = 0.009, \quad n(0.65 \ \mu\text{m}) = 1.542.$$

The last half-wave plate (QP_4) rotated the polarization of both beams by 45°, so that each detector placed after the polarized beam splitter detected the contribution from both polarizations (i.e., from both regions of interaction).

The size Δx of the diaphragm placed in front of the beam splitter was chosen in accordance with the conditions for detecting a single interference maximum ($\Delta x \leq \lambda_p z_0/b$, z_0 is the crystal–diaphragm distance).[9] An interference filter *IF* with a 10 nm passband, which corresponded to a 45 μm coherence length of the signal radiation, was used for spectral discrimination of the signal radiation. The pulses from the photomultiplier were fed into a coincidence circuit *CC* with a 1.9 ns time resolution.

Figure 3 shows the experimental dependence of the number $R_c(\delta)$ of coincidences in 20 min. The theoretical curve is a plot of the function $A(1 - V\cos[2\pi\delta/\lambda_p + \varphi_0])$ with adjustable constants A, V, and φ_0. Thus interference arises, with a period equal to the pump wavelength λ_p. The visibility V of the interference pattern is 85%. We note that the optical thickness of the first (QP_1) phase plate (460 μm) placed in one of the beams is an order of magnitude greater than the coherence length of the scattered field. This fact
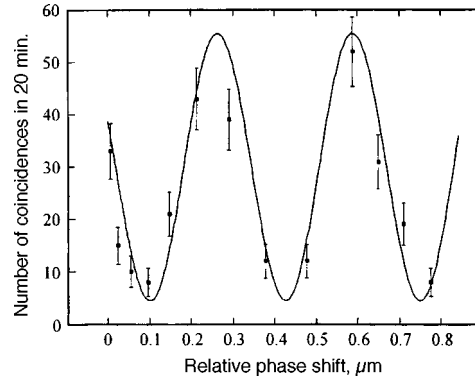
FIG. 3. Number of coincidences versus the relative phase shift between the signal radiation from two scattering regions. Dots — experimental data, solid curve — theoretical calculation. The interference period is equal to the pump wavelength, 0.325 μm.

confirms the conclusions drawn above that the observed phenomenon is independent of the coherence length of the signal field (in contrast to noncollinear scattering[8]).

The effect studied in this work has several paradoxical features.

The pump field E_p in Eq. (1) can be assumed to be classical (E_p is actually a quasimonochromatic random stationary field with a finite coherence length l_p, which in order to observe interference must be greater than the corresponding scales of the experimental apparatus — just as for the interference of independent photons). The operators H_1 and H_2 commute, so that the state of the scattered field factorizes

$$|\psi\rangle = e^{iH_1 t}|0\rangle_1 \otimes e^{iH_2 t}|0\rangle_2 = |\psi\rangle_1 \otimes |\psi\rangle_2 .$$

The fields scattered in each crystal are statistically independent. To first order in χE_p each crystal can be assumed to emit independent biphotons. This means that if we detect photons in the first and second beams using additional detectors D_1 and D_2, then the detectors will be triggered at different random times and there will be no coincidences of counts (aside from random coincidences, which are quadratic in the pump intensity).

According to Eq. (15), fourth-order interference occurs between independent biphotons, with a period equal to the pump wavelength λ_p, though actually there is no pump field at the exit mirror M' (the field is suppressed by the filters), and a phase shift is introduced into the scattered field. Therefore the biphotons in beams 1 and 2 are emitted at random independent times, so that they actually never overlap in time (the average time interval $1/R_i \approx 10^{-4}$ s between the emission of biphotons in each crystal is much longer than the coherence time $1/\Delta\nu_i \approx 10^{-12}$ s). Both simultaneously detected photons are created in the same crystal. But this conclusion contradicts the fact that according to Eq. (15) the crystals can ''destructively'' (for certain values of ϕ) influence the probability G_{34} of coincidences, and when one crystal is removed G_{34} can increase.

This paradox shows that there is no point in describing the effect pictorially in terms of photons — wave packets — emitted by one of the crystals and possessing a definite shape and position in space–time.

*⁾e-mail: postmast@qopt.ilc.msu.su

[1] H. Paul, Rev. Mod. Phys. **58**, 209 (1986).
[2] D. N. Klyshko and A. V. Masalov, Usp. Fiz. Nauk **165**, 1249 (1995).
[3] D. V. Strekalov, T. B. Pittman, and Y. H. Shih, Phys. Rev. A **57**, 567 (1998).
[4] D. N. Klyshko, Usp. Fiz. Nauk **166**, 613 (1996).
[5] T. B. Pittman, D. V. Strekalov, A. Migdall *et al.*, Phys. Rev. Lett. **77**, 1917 (1996).
[6] D. N. Klyshko, Phys. Lett. A **132**, 299 (1988).
[7] Z. Y. Ou, L. J. Wang, and L. Mandel, Phys. Rev. A **40**, 1428 (1989).
[8] Z. Y. Ou, L. J. Wang, X. Y. Zou *et al.*, Phys. Rev. A **41**, 566 (1990).
[9] A. V. Burlakov, M. V. Chekhova, D. N. Klyshko *et al.*, Phys. Rev. A **56**, 3214 (1997).
[10] A. V. Belinsky and D. N. Klyshko, Laser Phys. **4**, 663 (1994).
[11] R. J. Glauber, Phys. Rev. **130**, 2529 (1963).
[12] R. H. Brown and R. Q. Twiss, Nature (London) **177**, 27 (1956).

Translated by M. E. Alferieff

Polarized biphotons as ''optical quarks''

A. V. Burlakov and D. N. Klyshko

M. V. Lomonosov Moscow State University,[*] 119899 Moscow, Russia

The transformation properties and the measurable parameters of a quasimonochromatic optical field consisting of two photons with the same directions of propagation and average frequency are analyzed. Like quarks, such a field possesses $SU(3)$ symmetry. © *1999 American Institute of Physics.* [S0021-3640(99)00511-3]

PACS numbers: 42.50.−p

The parametric light scattering field at low pump intensities is described by a superposition of the vacuum and two-photon states. The corresponding particle, i.e., a pair of photons correlated with respect to the emission times, polarization, and direction, is called a biphoton. We shall be interested in the degenerate case, where the average energy, direction, and type of polarization of the emitted photons are the same. For observation with detectors with quite low frequency resolution at small scattering angles (degenerate collinear matching of the type *eoo*) it can be assumed that the signal and idler photons are indistinguishable (in practice this means that they are not distinguished by the detectors employed), and a single-mode description of the field can be used. If the vacuum component $|0,0\rangle$ is neglected, then we obtain the very simple case in which the parametric scattering field is described by the Fock vector $|2,0\rangle \equiv |2\rangle_x \otimes |0\rangle_y = (a_x^+)^2 |0,0\rangle / \sqrt{2}$ (x,y are the polarization indices, and a_x^+ is an operator creating a photon polarized in the x direction). The vector $|2,0\rangle$ describes a biphoton polarized in a definite direction x.

It is of interest to ascertain whether biphotons can be synthesized with prescribed arbitrary polarization states, to determine the polarization properties of the biphotons, and to find a convenient systematic description and parametrization of such states. These problems could be pertinent to possible applications for information transmission and storage[1] and the development of components for quantum computers.[2] Some experiments along these lines are described in Refs. 3 and 4, but apparently no systematic theoretical and experimental investigations have been performed.

Here we confine our attention to the general properties of idealized pure states of a two-photon field (biphotons) that can be represented as

$$|\psi\rangle = c_1|2,0\rangle + c_2|1,1\rangle + c_3|0,2\rangle \quad (\Sigma|c_k|^2 = \Sigma d_k^2 = 1). \tag{1}$$

Here $|m,n\rangle$ is a Fock state with a definite number of photons ($m,n = 0,1,2$) in each of two polarization modes. We shall use the following parametrization and notations:

$$c_k \equiv d_k \exp(i\phi_k), \quad \phi_2 \equiv 0, \quad d_1 \equiv \sin\theta\cos\phi, \quad d_2 \equiv \cos\theta, \quad d_3 \equiv \sin\theta\sin\phi$$
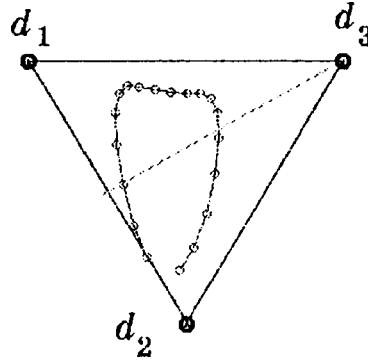
FIG. 1. Example of a trajectory described by an ''optical quark'' under the action of a loss-free polarization converter with a change in optical length of the converter. For clarity, ''triangular'' coordinates are used: each point inside a triangle corresponds to a state with definite coefficients $d_k \equiv |c_k|$. For example, the center of the triangle represents a superposition with $d_k = 1/\sqrt{3}$, specifically, the state $|\psi\rangle = (|2,0\rangle + |1,1\rangle + |0,2\rangle)/\sqrt{3}$, and the corners of the triangle represent the states $|2,0\rangle$, $|1,1\rangle$, and $|0,2\rangle$ ($|m,n\rangle$ is a Fock state with definite numbers of photons in three polarization modes).

$$(\theta, \phi \in [0, \pi/2], \quad \phi_{1,3} \in [0, 2\pi]). \tag{2}$$

Thus an arbitrary polarization state of a biphoton $|\psi\rangle$ with definite energy and direction is prescribed by four real numbers, for example, $(d_1, d_3, \phi_1, \phi_3)$ or $(\theta, \phi, \phi_1, \phi_3)$. Then $|\psi\rangle$ can be mapped into a point on the surface of a sphere $\mathbf{S}^4$ in a five-dimensional space (here there is an analogy with the Poincaré sphere in ordinary polarized optics or in the case of a single-photon state). For clarity it is convenient to employ ''triangular'' coordinates (see Fig. 1). Then the state is mapped onto a triangle with the coordinates (d_1, d_2, d_3) and a square with the coordinates (ϕ_1, ϕ_3). Under a linear transformation the polarization state of a biphoton changes and the image point moves in the space $(d_1, d_3, \phi_1, \phi_3)$ or $(\theta, \phi, \phi_1, \phi_3)$. An example of such a biphoton trajectory is given in Fig. 1.

The vector $\mathbf{e} = (c_1, c_2, c_3)$ determines the polarization properties of a biphoton field, and it can be called the polarization vector of a biphoton. The space of vectors $\{\mathbf{e}\}$ and the set of 3×3 unitary matrices G with the properties $GG^+ = 1$ and $\det(G) = 1$, describing a norm-preserving linear transformation of this space, form a three-dimensional unitary representation of the Lie group $SU(3)$. As is well known (see Ref. 5), this is a group of dimension 8 and rank 2 (i.e., it possesses eight transformation generators, two of which commute with one another). Correspondingly, the matrix G connecting two prescribed points in the space $\{\mathbf{e}\}$ and describing a transformation of the polarization of a biphoton (no losses) is given by eight parameters. (For comparison we recall the $SU(2)$ group with dimension 3 and rank 1, generated by three Pauli matrices; in this case, two points on the Poincaré sphere are connected by a rotation given by three Euler angles). All possible matrices transforming the space $\{\mathbf{e}\}$ and all operators can be represented as a superposition of eight generators of the group, for example, the Gell-Mann operators λ_k and the unit operator I. It follows from the block structure of the operators λ_k that $SU(3)$ possesses three $SU(2)$ subgroups.

Therefore there is a formal analogy here between biphotons and quarks: the two-photon basis states $|2,0\rangle$, $|1,1\rangle$, and $|0,2\rangle$ can be put into a correspondence with three quarks u, d, and s, and a superposition of the states u, d, and s corresponds to a biphoton in the arbitrary state (1). (For ''real'' quarks superselection rules that conserve charge and strangeness forbid such intermediate states.) Biphoton pairs and triplets form multiplets corresponding to various mesons and hadrons.

We consider next the possibility of controlling biphotons using polarized optics methods. The effect of loss-free polarization converters (phase plates) on a biphoton can be described by 3×3 unitary matrices: $\mathbf{e}' = G\mathbf{e}$, where

$$
G = \begin{vmatrix} t^2 & \sqrt{2}tr & r^2 \\ -\sqrt{2}tr* & |t^2| - |r^2| & \sqrt{2}t*r \\ r*^2 & -\sqrt{2}t*r* & t*^2 \end{vmatrix}.
\tag{3}
$$

Here t and r are amplitude transmission and reflection coefficients of a given converter. For example, a linear phase plate with optical thickness δ and orientation χ relative to the horizontal direction x corresponds to the transformation $t = \cos\delta + i\sin\delta\cos(2\chi)$, $r = i\sin\delta\sin(2\chi)$. For a quarter-wave plate we have $d = \pi/4$ and $t = (1 + i\cos 2\chi)/\sqrt{2}$, $r = i\sin 2\chi/\sqrt{2}$; for $\chi = 45°$ $t = 1/\sqrt{2}$, $r = i\sqrt{2}$ — linear polarization is converted into circular polarization. A half-wave plate gives $t = i\cos 2\chi$, $r = i\sin 2\chi$ — rotation of linear polarization by 2χ; for $\chi = 45°$ we have $t = 0$, $r = i$ — the conversion $x \leftrightarrow y$. Specifically, the state $|1,1\rangle$ can be prepared from the state $(|2,0\rangle + |0,2\rangle)/\sqrt{2} = |1\rangle_+|1\rangle_-$ (the indices $+$ and $-$ correspond to circular polarization). Both states $(|2,0\rangle + |0,2\rangle)/\sqrt{2}$ and $|1,1\rangle$ belong to a set with the same polarization (the degree of polarization $P = 0$), so that for this it is sufficient to convert linear polarization into circular polarization using a quarter-wave plate oriented at an angle of $45°$, in which case $t = 1/\sqrt{2}$, $r = i/\sqrt{2}$.

Arbitrary combinations of several phase plates are described by the matrices $G(\theta, \varphi, \psi)$, which depend on the three Euler angles (see Ref. 5). They give a 3×3 irreducible unitary representation of the group $SU(2)$ in the space $\{\mathbf{e}\}$. It is obvious that it is impossible to obtain an arbitrary transformation of a biphoton from one prescribed state into another using only phase plates — five additional parameters are required. In other words, the space $\{\mathbf{e}\}$ is not homogeneous relative to the action of phase plates: It is impossible to obtain an arbitrary vector $\mathbf{e}'$ from an arbitrary initial vector $\mathbf{e}$ by means of phase plates alone.

This is obvious immediately from the fact that phase plates preserve the degree of polarization. Therefore phase plates realize only a certain subgroup of the $SU(3)$ group. Besides the degree of polarization, loss-free phase plates preserve, of course, the total number of photons in two polarized modes: $S_0 = 2$ (this parameter is an invariant of the group $SU(3)$).

Thus, an arbitrary combination of phase plates that is described by three Euler angles does not permit preparing from a prescribed initial state $|\psi\rangle_0$ (four parameters) an arbitrary biphoton in the state $|\psi\rangle$ also prescribed by four parameters. For example, for parametric scattering of the type eoo polarized biphotons with $|\psi\rangle = |2,0\rangle$, where $\mathbf{e} = (1,0,0)$ and $P = 1$, are generated. These biphotons cannot be put into the state $|1,1\rangle$ (which possesses ''hidden polarization''[6]), where $P = 0$, using phase plates. To synthesize an arbitrary biphoton it is necessary to realize a transformation that changes the

degree of polarization of the biphoton between 0 and 1. A parametric converter with several nonlinear crystals can be used to prepare a biphoton with an adjustable degree of polarization. Nonunitary transformations can also be used.

Let us consider the basic parameters that can be directly measured in quantum optics — stationary normal-ordered second- and fourth-order moments. The second moments have the form

$$n_x = \langle a_x^+ a_x \rangle = 2d_1^2 + d_2^2 = 1 + \sin^2 \theta \cos 2\phi, \tag{4}$$

$$n_y = \langle a_y^+ a_y \rangle = d_2^2 + 2d_3^2 = 1 - \sin^2 \theta \cos 2\phi, \tag{5}$$

$$\langle a_x^+ a_y \rangle = \sqrt{2}(c_1^* c_2 + c_2^* c_3) = \sqrt{2} d_2 [d_1 \exp(i\phi_{21}) + d_3 \exp(i\phi_{32})]$$
$$= 2^{-1/2} \sin 2\theta [\cos \phi \exp(-i\phi_1) + \sin \phi \exp(i\phi_3)]. \tag{6}$$

It is easy to show that the degree of polarization of a biphoton is

$$P = \left[\Sigma \left(\frac{1}{2} \langle S_k \rangle \right)^2 \right]^{1/2} = \{ (|c_1|^2 - |c_3|^2)^2 + 2|c_1^* c_2 + c_2^* c_3|^2 \}^{1/2}$$

$$= \{ (d_1^2 - d_3^2)^2 + 2d_2^2 [d_1^2 + d_3^2 + 2d_1 d_3 \cos(\phi_1 + \phi_3)] \}^{1/2}$$

$$= \sin \theta \{ \cos^2 2\phi + \cos^2 \theta [1 + \sin^2 2\phi + 2\sin^2 2\phi \cos(\phi_3 + \phi_1)] \}^{1/2}. \tag{7}$$

The Stokes parameters $\langle S_k \rangle$ (see Ref. 7) for a biphoton have the form

$$\langle S_1 \rangle = 2(d_1^2 - d_3^2) = 2 \sin^2 \theta \cos 2\phi, \tag{8}$$

$$\langle S_2 \rangle = 2\sqrt{2} \, \mathrm{Re}(c_1^* c_2 + c_3^* c_2) = 2\sqrt{2} d_2 (d_1 \cos \phi_{21} + d_3 \cos \phi_{32})$$
$$= \sqrt{2} \sin 2\theta (\cos \phi \cos \phi_1 + \sin \phi \sin \phi_3), \tag{9}$$

$$\langle S_3 \rangle = 2\sqrt{2} \, \mathrm{Im}(c_1^* c_2 + c_3 c_2^*) = 2\sqrt{2} d_2 (d_1 \sin \phi_{21} + d_3 \sin \phi_{32})$$
$$= \sqrt{2} \sin 2\theta (\sin \phi \sin \phi_3 - \cos \phi \sin \phi_1). \tag{10}$$

It is convenient to introduce also the following set of four moments:

$$A \equiv \langle a_x^{+2} a_x^2 \rangle = 2d_1^2 = 2 \sin^2 \theta \cos^2 \phi, \tag{11}$$

$$B \equiv \langle a_y^{+2} a_y^2 \rangle = 2d_3^2 = 2 \sin^2 \theta \sin^2 \phi, \tag{12}$$

$$C \equiv \langle a_x^+ a_x a_y^+ a_y \rangle = d_2^2 = \cos^2 \theta, \tag{13}$$

$$D \equiv \langle a_x^{+2} a_x a_y \rangle = \sqrt{2} c_1^* c_2 = \sqrt{2} d_1 d_2 \exp(-i\phi_1) = \sin 2\theta \cos \phi \exp(-i\phi_1)/\sqrt{2}, \tag{14}$$

$$F \equiv \langle a_x^+ a_y^+ a_y^2 \rangle = \sqrt{2} c_2^* c_3 = \sqrt{2} d_2 d_3 \exp(i\phi_3) = \sin 2\theta \sin \phi \exp(i\phi_3)/\sqrt{2}, \tag{15}$$

$$E \equiv \langle a_x^{+2} a_y^2 \rangle = 2c_1^* c_3 = 2d_1 d_3 \exp(i\phi_{31}) = \sin^2 \theta \sin 2\phi \exp(i\phi_{31}) \tag{16}$$

($\phi_{31} \equiv \phi_3 - \phi_1$). Hence follow the two relations $A + B + 2C = 2$ and $DFE^* = ABC/2$, and the parameters $C = 1 - (A+B)/2$ and $E = ABC/2DF$ can be eliminated. It is important

that the moments A, B, and C are real and do not depend on the phase of the pump. We note that the complex moments D, F, and E in the absence of the vacuum component $|00\rangle$ can be comparable in magnitude to A, B, and C.

In conclusion, we underscore that switching from the ordinary ''two-level'' $SU(2)$ space (qubits)[2] to the space $SU(3)$ (quarks) when processing information gives new possibilities and could be of practical interest (specifically, in quantum computers). However, a variety of technical problems must be overcome in order to implement this program.

*)e-mail: postmast@qopt.ilc.msu.su

[1] A. K. Ekert, J. G. Rarity, P. R. Tapster, and G. M. Palma, Phys. Rev. Lett. **69**, 1293 (1992).
[2] C. H. Bennett, G. Brassard, C. Crepeau *et al.*, Phys. Rev. Lett. **70**, 1895 (1993); D. P. Di Vincenzo, Phys. Rev. A **51**, 1015 (1995).
[3] A. V. Burlakov, M. V. Chekhova, D. N. Klyshko *et al.*, Phys. Rev. A **56**, 3214 (1997).
[4] A. V. Burlakov, D. N. Klyshko, S. P. Kulik *et al.*, JETP Lett. **65**, 19 (1997).
[5] A. Sudbery, *Quantum Mechanics and the Particles of Nature* (Cambridge University Press, Cambridge–New York, 1986) [Russian translation, Mir, Moscow, 1989].
[6] D. I. Guzun and A. N. Penin, Proc. Soc. Photo-Opt. Instrum. Eng. **2799**, 249 (1996).
[7] D. N. Klyshko, Zh. Éksp. Teor. Fiz. **111**, 1955 (1997) [JETP **84**, 1065 (1997)].

Translated by M. E. Alferieff

Predicted existence of H_3^{++} molecular ions in strong magnetic fields

A. Turbiner,[*] J.-C. Lopez, and U. H. Solis

Instituto de Ciencias Nucleares, UNAM, 04510 México D. F., México

It is shown by a variational method that the molecular ion H_3^{++} can exist for magnetic fields $B > 10^{11}$ G. © *1999 American Institute of Physics.* [S0021-3640(99)00611-8]

PACS numbers: 31.15.Pf, 33.15.−e

Many years ago it was predicted by Kadomtsev and by Kudryavtsev[1] and Ruderman[2] (for a recent advances and a review, see, e.g., Ref. 3 and 4 and references therein) that the presence of a strong magnetic field can permit the formation of unusual chemical compounds whose existence is impossible in the absence of the strong magnetic field. In particular, using a semiclassical analysis it was shown that the influence of the strong magnetic field leads to the appearance of linear molecules (linear chains) situated along magnetic field lines. The transverse size of such systems should be of the order of the cyclotron radius $\hat{\rho} \sim B^{-1/2}$ (a.u.), while the longitudinal size remains of molecular (atomic) order. These systems are called needlelike. An important consequence of this quasi-one-dimensionality of Coulombic systems is the possibility of effectively compensating the Coulombic repulsion of nuclei.

The goal of this letter is to present the first quantitative study of the molecular ion H_3^{++} in a strong magnetic field. This study provides theoretical evidence that such a system can exist in magnetic field $B > 10^{11}$ G. Our study is limited to an exploration of the ground state. Throughout the present work it is assumed that the Born–Oppenheimer approximation holds, which implies that the positions of the protons are fixed. Exactly as for the H_2^+ case, we consider a configuration in which the three protons are aligned with the magnetic field (linear chain; see above). Spin effects (linear Zeeman effect) are neglected. The magnetic field ranges from 0 up to 10^{13} G, where it is assumed that the contribution of relativistic corrections can still be neglected (for a discussion see, e.g., Ref. 4 and references therein). Finally, it is also demonstrated that the molecular ion H_2^+ is the most bound one-electron molecular system in a constant magnetic field.

The present calculation is carried out in the framework of a variational method using a *unique* simple trial function equally applicable to any value of the magnetic field strength. Very recently[4] this strategy was successfully applied to study the ground state of the molecular ion H_2^+, and a simple 10-parameter trial function allowed one to get the best (lowest) values of the ground state energy for magnetic fields from 0 up to 10^{13} G (except at $B=0$, where the relative accuracy was about 10^{-5} in comparison with the best
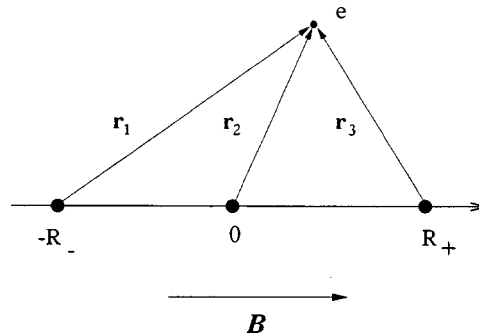
844

FIG. 1. H_3^{++} in a magnetic field B. Explanation of the notation used.

calculations). It turned out that it was not only the best calculation in the region of accessible magnetic fields $0-10^{13}$ G but also the only calculation which tackled the problem using a unified approach. Since the key point of a successful study is a wise choice of trial functions, we give a detailed description of how to choose trial functions suited to the problem at hand.

A constructive criterion for an adequate choice of trial function was formulated in Ref. 6, and further development was presented in Refs. 7 and 8. In its simplest form the criterion is the following. The trial function $\Psi_t(x)$ should contain all symmetry properties of the problem at hand. For studying the ground state, the trial function should not vanish inside the domain in which the problem is defined. The potential $V_t(x) = \nabla^2 \Psi_t / \Psi_t$, for which the trial function is an eigenfunction, should reproduce the original potential near singularities as well as its asymptotic behavior. The use of this simplest possible recipe has led to a unique one-parameter trial function, which in particular, made it possible to carry out the first qualitative study of the ground state of the hydrogen molecule H_2 in the region of both weak and strong magnetic fields.[9] Later a few-parameter trial function was proposed for a description of the hydrogen atom in an arbitrary magnetic field, which led, for the low excited states, to an accuracy comparable with the best calculations.[8,10]

Now we wish to apply the above recipe to the ion H_3^{++}. Let us first introduce notation (see Fig. 1). We consider three attractive identical centers of unit charge situated on the z axis at the origin and at a distance R_-, R_+ from the origin, respectively. The magnetic field, of strength B, is directed along the z axis, and $r_{1,2,3}$ are the distances from the electron to the first, second, or third center, respectively. The quantity ρ is the distance from the electron to the z axis. Throughout this paper the Rydberg is used as the energy unit. For the other quantities standard atomic units (a.u.) are used. The potential corresponding to the problem under study is given by

$$V = \frac{2}{R_-} + \frac{2}{R_+} + \frac{2}{R_- + R_+} - \frac{2}{r_1} - \frac{2}{r_2} - \frac{2}{r_3} + \frac{B^2 \rho^2}{4}, \tag{1}$$

where the first three terms have the meaning of the classical Coulomb energy of interaction of three charged centers. The recipe dictates that the trial functions should behave in a Coulomb-like way near the centers, correspond to two-dimensional oscillator behavior in the (x,y) plane at large distances, and be permutationally symmetric with respect to

exchange of positions of the centers. It seems quite natural that the equilibrium configuration corresponding to minimal total energy of the system should appear at $R_- = R_+$.

One of the simplest functions satisfying the above recipe is a function of the Heitler–London type multiplied by the lowest Landau orbital:

$$\Psi_1 = \exp\{-\alpha_1(r_1 + r_2 + r_3) - \beta_1 B \rho^2/4\}, \tag{2}$$

(cf. Eq. (2.2) in Ref. 5), where α_1, β_1 are variational parameters. It has a total of four variational parameters if the internuclear distances R_-, R_+ are taken as parameters. It is quite natural from a physical viewpoint to assume that a function of the Heitler–London type gives an adequate description of the system near the equilibrium position. The potential $V_1(x) = \nabla^2 \Psi_1/\Psi_1$ corresponding to this function is:

$$V_1 = 3\alpha_1^2 - B\beta_1 - 2\alpha_1\left(\frac{1}{r_1} + \frac{1}{r_2} + \frac{1}{r_3}\right) + \frac{\beta_1^2 B^2 \rho^2}{4} + 2\alpha_1^2\left[\frac{1}{r_1 r_2}(\rho^2 + z(z + R_+))\right.$$

$$+ \frac{1}{r_2 r_3}(\rho^2 + z(z - R_-)) + \frac{1}{r_1 r_3}(\rho^2 + (z - R_-)(z + R_+))\right]$$

$$+ \alpha_1 \beta_1 B \rho^2\left(\frac{1}{r_1} + \frac{1}{r_2} + \frac{1}{r_3}\right). \tag{3}$$

It is clear that this potential reproduces the original potential (1) near Coulomb singularities as well as at large distances $|x,y| \to \infty$.

Another possible trial function is a function of the Hund–Mulliken type multiplied by the lowest Landau orbital:

$$\Psi_2 = [\exp(-\alpha_2 r_1) + \exp(-\alpha_2 r_2) + \exp(-\alpha_2 r_3)]\exp(-\beta_2 B \rho^2/4) \tag{4}$$

(cf. Eq. (2.4) in Ref. 5), where α_2, β_2 are variational parameters. It is obvious that this function, in the absence of a magnetic field, gives a substantial contribution to the description of the region of large internuclear distances. The calculations we have performed show that this property remains valid for all magnetic fields up to 10^{13} G. Like Eq. (2), the trial function (4) is characterized by four variational parameters. This function, when both internuclear distances are large, corresponds to the decay $H_3^{++} \to H + p + p$.

Another trial function is supposed to describes the decay mode $H_3^{++} \to H_2^+ + p$ and could be taken to be of the form

$$\Psi_3 = [\exp(-\alpha_3(r_1 + r_2)) + \exp(-\alpha_3(r_1 + r_3))$$

$$+ \exp(-\alpha_3(r_2 + r_3))]\exp(-\beta_3 B \rho^2/4), \tag{5}$$

where α_3, β_3 are variational parameters. Finally, it will become obvious that the function (5) does give the dominant contribution at large internuclear distances. Equation (5) also depends on four variational parameters.

To take into account both equilibrium and large distances, we use an interpolation of Eqs. (2), (4), and (5). There are three natural approaches to such an interpolation:

(i) A total nonlinear superposition:

$$\Psi_{4-nls-t} = [\exp(-\alpha_4 r_1 - \alpha_5 r_2 - \alpha_6 r_3) + \exp(-\alpha_5 r_1 - \alpha_4 r_2 - \alpha_6 r_3)$$
$$+ \exp(-\alpha_4 r_1 - \alpha_6 r_2 - \alpha_5 r_3) + \exp(-\alpha_6 r_1 - \alpha_4 r_2 - \alpha_5 r_3)$$
$$+ \exp(-\alpha_5 r_1 - \alpha_6 r_2 - \alpha_4 r_3) + \exp(-\alpha_6 r_1 - \alpha_5 r_2 - \alpha_4 r_3)]\exp(-\beta_4 B \rho^2/4),$$

$$(6)$$

(cf. Eq. (2.5) in Ref. 5), where $\alpha_{4,5,6}$ and β_4 are variational parameters. The function (6) is a three-center modification of the function of the Guillemin–Zener type used for the description of the molecular ion H_2^+ in a magnetic field.[5] If $\alpha_4 = \alpha_5 = \alpha_6 \equiv \alpha_1$, the function (6) reduces to Eq. (2). When $\alpha_4 \equiv \alpha_2, \alpha_5 = \alpha_6 = 0$, it coincides with Eq. (4). Finally, if $\alpha_4 = \alpha_5 \equiv \alpha_3, \alpha_6 = 0$, the function (6) reduces to Eq. (5). In total there are 6 variational parameters characterizing the trial function (6).

(ii) A partial nonlinear superposition, which appears if in Eq. (6) the two parameters are equal, for instance, $\alpha_4 = \alpha_5$:

$$\Psi_{4-nls-p} = [\exp(-\alpha_4(r_1 + r_2) - \alpha_6 r_3) + \exp(-\alpha_4(r_1 + r_3) - \alpha_6 r_2)$$
$$+ \exp(-\alpha_4(r_2 + r_3) - \alpha_6 r_1)]\exp(-\beta_4 B \rho^2/4). \qquad (7)$$

This function can be regarded as a nonlinear interpolation between Eqs. (4) and (5).

(iii) A linear superposition of Eqs. (2), (4), and (5):

$$\Psi_{4-ls} = A_1 \Psi_1 + A_2 \Psi_2 + A_3 \Psi_3, \qquad (8)$$

where the relative weights of Eqs. (2), (4), and (5) in Eq. (7) are taken as extra variational parameters. This is a 10-parameter trial function.

Of course, as a natural continuation of the above interpolation procedure one can take a linear superposition of all five functions (2), (4), (5), (6), and (7):

$$\Psi_5 = A_{4-nls-t}\Psi_{4-nls-t} + A_{4-nls-p}\Psi_{4-nls-p} + A_{4-ls}\Psi_{4-ls}$$
$$= A_{4-nls-t}\Psi_{4-nls-t} + A_{4-nls-p}\Psi_{4-nls-p} + A_1\Psi_1 + A_2\Psi_2 + A_3\Psi_3 \qquad (9)$$

(cf. Eq. (2.7) in Ref. 5), where again, as in the case of the function (8), the relative weights of different, ''primary'' trial functions are considered as variational parameters. In total, the trial function (9) is characterized by 17 variational parameters. However, only part of our calculation is carried out using this function. Usually, some particular cases of Eq. (9) are explored. The general case will be presented elsewhere. The minimization procedure is carried out using the standard minimization package MINUIT from CERN-LIB on a Pentium-Pro PC. All integrals were calculated using the CERN-LIB routine DGAUSS with relative accuracy $\leq 10^{-7}$.

In Table I the results of our variational calculations are presented. It is quite remarkable that for magnetic field strengths $> 10^{11}$ G there exists a total-energy minimum in the (R_+, R_-) plane. Furthermore, for such magnetic fields the value of the energy at the minimum corresponding to the total energy of H_3^{++} is always lower than the total energy of the hydrogen atom but higher than that of H_2^+. Hence the decay mode $H_3^{++} \rightarrow H + p + p$ is forbidden. However, H_3^{++} is unstable with respect to the decay $H_3^{++} \rightarrow H_2^+ + p$. It seems natural to assume that even if one-electron systems like H_4^{+++}, H_5^{++++} etc. were bounded, their total energies would be larger than the total energy for H_3^{++}. This assumption and a comparison of the total energies of H, H_2^+, H_3^{++} (see Table I) allow one

TABLE I. Data for the ground state of H_3^{++} and a comparison with data for other one-electron systems, H, H_2^+.

	$B=0$		$B=10^{11}$ G			$B=10^{12}$ G			$B=10^{13}$ G		
	E (Ry)	R_{eq} (a.u.)	E (Ry)	R_{eq} (a.u.)	$\langle z \rangle$ (a.u.)	E (Ry)	R_{eq} (a.u.)	$\langle z \rangle$ (a.u.)	E (Ry)	R_{eq} (a.u.)	$\langle z \rangle$ (a.u.)
H	−1.000	–	36.929	—	—	413.57	—		4231.6	–	–
H_2^+	−1.205	1.997	35.036	0.593	0.312	408.300	0.283	0.174	4218.662	0.147	0.107
H_{3++}	–	–	36.429	0.803	0.432	410.296	0.346	0.219	4220.090	0.165	0.121

Note: The total energy E is in Rydbergs, the equilibrium distance $R_{eq} \equiv R_{+eq} = R_{-eq}$ (see text), and the average value of the longitudinal size of the system $\langle z \rangle$ is in atomic units (a.u.). The total energy for the hydrogen atom is from Ref. 11; the data for H_2^+ is from Ref. 5.

to conclude that H_2^+ is the most stable one-electron system in a constant magnetic field oriented along the magnetic field. The equilibrium distances for H_3^{++} decrease with increasing magnetic field: the ion H_3^{++}, like H_2^+, becomes more and more compact. It is worth noting that for both H_2^+ and H_3^{++} the average value $\langle z \rangle$ is much smaller than the ''natural'' size of the system, determined by the positions of the centers: R_{eq} for H_2^+ and $(R_{+eq} + R_{-eq})$ for H_3^{++} (see Fig. 1). In other words, this means that the localization length of electron is much smaller than the ''natural'' size of the system.

Figure 2 shows the electronic density distribution as a function of magnetic field. For a magnetic field $B \simeq 10^{11}$ G the distribution has three distinct maxima corresponding to the positions of the centers, but the electron is situated preferably near the central proton. The situation changes drastically as the magnetic field is increased: the electron is localized near $z=0$, having almost no memory of the two centers on either side. It is important to investigate paths of possible tunneling. There are two pronounced valleys (symmetric with respect to $R_+ \leftrightarrow R_-$) in the electronic potential energy surfaces, $E_{\text{total}}(R_+, R_-)$ (see Fig. 3a).

They vary from the position of the H_3^{++} minimum to infinity, which corresponds to
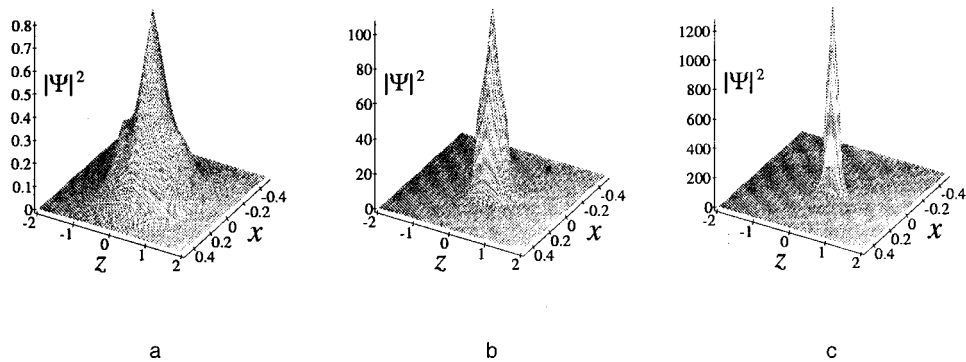

FIG. 2. Electronic distribution for various magnetic fields: 10^{11} G (a), 10^{12} G (b) and 10^{13} G (c). It peaks more and more sharply at the origin with growth of magnetic field.
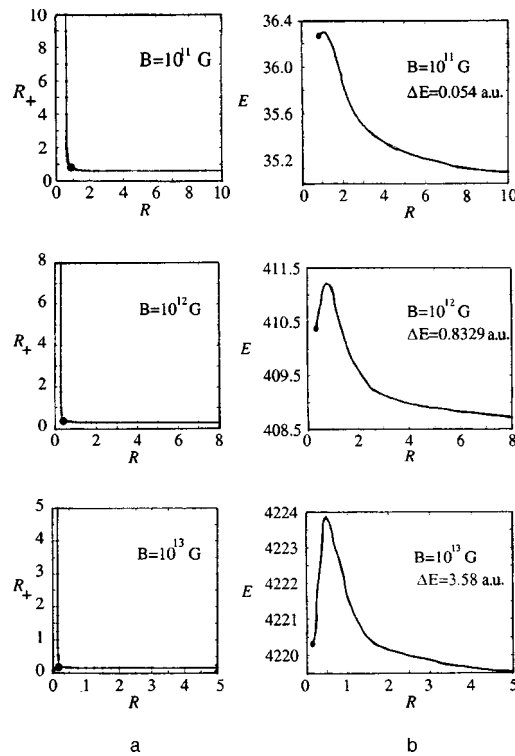
FIG. 3. Valleys in the electronic potential energy surfaces $E_{\text{total}}(R_+, R_-)$ (a) and their profiles (b) for various magnetic fields. The position of the minimum is indicated by a bullet, and ΔE denotes the depth of the well: the distance between top of the barrier and the value of the minimum.

the $H_2^+ + p$ dissociation: $(R_{+\text{eq}}, R_{-\text{eq}}) \rightarrow (\infty, R_{H_2^+}^{\text{eq}})$ and $(R_{+\text{eq}}, R_{-\text{eq}}) \rightarrow (R_{H_2^+}^{\text{eq}}, \infty)$, where $R_{H_2^+}^{\text{eq}}$ is the equilibrium distance for the H_2^+ ion. In Fig. 3b one can see the profile of the valley as a function of magnetic field. By calculating the Gaussian curvatures at the H_3^{++} minimum one can estimate the position of the ground state energy level and answer the question of whether the well is deep enough to hold an energy level. It is always delicate to answer the question of at what well ''depth'' does a level begin to exist. Usually, it requires special analysis. We made an estimate and obtained the result that for a magnetic field of 10^{11} G the situation is uncertain, the well is probably still too shallow to hold the ground state energy level. However, the well undoubtedly becomes sufficiently deep for 10^{12-13} G. From the form of the profile (see Fig. 3b) it is quite obvious that for 10^{12-13} G the barrier is rather high and the probability of tunneling should be small.

*)On leave of absence from the Institute for Theoretical and Experimental Physics, 117259, Moscow, Russia;
*)e-mail: turbiner@xochitl.nuclecu.unam.mx

---

[1] B. B. Kadomtsev and V. S. Kudryavtsev, JETP Lett. **13**, 9, 42 (1971)]; Zh. Éksp. Teor. Fiz. **62**, 144 (1972) [Sov. Phys. JETP **35**, 76 (1972)].

[2] M. Ruderman, Phys. Rev. Lett. **27**, 1306 (1971); in Physics of Dense Matter, edited by C. J. Hansen, IAU Symposium 53, Reidel, Dordrecht, 1974, p. 117.

[3] D. Lai and E. Salpeter, Phys. Rev. A **52**, 2611 (1995); **53**, 152 (1995).

[4] D. Lai and E. Salpeter, Astrophys. J. **491**, 270 (1997).

[5] J.-C. Lopez, P. O. Hess, and A. Turbiner, Phys. Rev. A **56**, 4496 (1997); http://xxx.lanl.gov/abs/astro-ph/9707050.

[6] A. V. Turbiner, Zh. Éksp. Teor. Fiz. **79**, 1719 (1980) [Sov. Phys. JETP **52**, 868 (1980)].

[7] A. V. Turbiner, Usp. Fiz. Nauk. **144**, 35 (1984) [Sov. Phys. Usp. **27**, 668 (1984)].

[8] A. V. Turbiner, Yad. Fiz. **46**, 204 (1987) [Sov. J. Nucl. Phys. **46**, 125 (1987)].

[9] A. V. Turbiner, JETP Lett. **38**, 618 (1983).

[10] A. V. Turbiner, Doctor of Sciences Thesis, ITEP, Moscow, 1989 (unpublished).

[11] D. Lai, E. Salpeter, and S. L. Shapiro, Phys. Rev. A **45**, 4832 (1992).

Stochastic heating of plasma at electron cyclotron resonance

A. N. Antonov, V. A. Buts, O. F. Kovpik, E. A. Kornilov,
O. V. Manuĭlenko,*) V. G. Svichenskiĭ, K. N. Stepanov,
and Yu. A. Turkin

Kharkov Physicotechnical Institute National Science Center, 310108 Kharkov, Ukraine

It is shown theoretically and experimentally that stochastic heating of plasma electrons is highly efficient. Calculations have shown that over the course of 100 periods of an external microwave field the kinetic energy of the particles reaches values of around 1.0 MeV and the average energy reaches values of the order of 0.3 MeV in the field of two oppositely propagating characteristic (eigen) waves of a cylindrical waveguide, with amplitudes 24 kV/cm in a 1 kG stationary magnetic field. Stochastic instability develops as a result of overlapping of non-linear cyclotron resonances. The experimental results agree with the theory: When these waves are excited by a 0.9 MW external source, above a threshold of 0.45 MW one obtains x rays with a photon energy corresponding to a maximum electron energy of the order of 1 MeV over about 800 periods of the external microwave field. © *1999 American Institute of Physics.* [S0021-3640(99)00711-2]

PACS numbers: 52.50.Gj, 52.35.Qz

1. Various radio-frequency (rf) methods based on linear ''collisionless'' energy absorption mechanisms are widely used to heat plasma in controlled thermonuclear fusion devices.[1,2] In a typical situation waves are absorbed in a narrow resonant range, where the particles acquire or give up energy depending on the wave–particle phase and then, moving along magnetic flux lines, they ''forget'' the phase as a result of collisions, so that in the subsequent passage through the resonant zone this phase can be taken as random. In this case a particle acquires energy on the average. This method of heating makes it possible to reach thermonuclear temperatures if the energy lifetime of the plasma is sufficiently long. These methods are inapplicable if the plasma must be heated in a very short time. In this case heating can be accomplished by direct conversion of electromagnetic wave energy into thermal energy of the plasma particles, where ''intermediate'' stages of the heating process, for example, collisions, are eliminated. Direct collisionless heating can be accomplished in two ways. In the first method the field itself must be chaotic, and in the second method (which we refer to below as stochastic heating) conditions under which particle motion in the field of regular waves becomes chaotic are produced. The first heating method requires noise generators. Moreover, apparently, in all cases of practical interest stochastic heating of plasma by the fields of regular waves is more efficient than heating by noise fields.[3]

Stochastic heating of plasma in open magnetic traps has been studied in Refs. 4–7, and multifrequency electron cyclotron resonance (ECR) heating has been studied in Refs. 8–10. The stochastic heating model studied in Ref. 4 and the works cited therein is less efficient than the heating scheme investigated in the present work. This is because when plasma is heated in open magnetic traps, energy transfer from the electromagnetic field to the plasma particles occurs in a narrow range where cyclotron resonance conditions are satisfied for the plasma electrons with an external rf field. After passing through such a resonant region the particles move along magnetic field lines without interacting resonantly with the rf field. In the heating scheme studied in the present work, however, the interaction of the plasma electrons with the rf field occurs not in a narrow resonant region but rather in the entire volume occupied by the plasma particles. This eliminates the time interval during which the plasma particles do not interact with the field of the electromagnetic wave.

In the present letter we report the results of theoretical and experimental investigations of stochastic heating of plasma electrons by the field of electromagnetic waves of a circular waveguide and a circular cavity in a constant external magnetic field.

2. Let us consider the motion of a charged particle in the field H of a wave in a circular waveguide with radius a in a constant magnetic field H_0 directed along the waveguide axis. In a cylindrical coordinate system (r,ϕ,z) with origin at the center of the transverse section of the waveguide and z axis directed along the waveguide axis, the field components H_{mn} of the wave have the form

$$E_r = E_0 \frac{m}{k_\perp r} J_m(k_\perp r)\sin(m\varphi)\sin(k_z z - \omega t),$$

$$E_\varphi = E_0 J'_m(k_\perp r)\cos(m\varphi)\sin(k_z z - \omega t), \quad E_z = 0,$$

$$H_r = -\frac{k_z}{k}E_\varphi, \quad H_\varphi = \frac{k_z}{k}E_r, \quad H_z = \frac{k_\perp}{k}E_0 J_m(k_\perp r)\cos(m\varphi)\cos(k_z z - \omega t), \quad (1)$$

where J_m is a Bessel function of order m, J'_m is a derivative of the Bessel function, $k_\perp = \nu_{mn}/a$, $J'_m(\nu_{m,n}) = 0$, $k_z = \sqrt{k^2 - k_\perp^2}$, $k = \omega/c$, c is the speed of light, and ω is the frequency. In dimensionless variables

$$\omega t \to t, \quad \mathbf{r}\omega/c \to \mathbf{r}, \quad \mathbf{p}/Mc \to \mathbf{p}, \quad k_\perp c/\omega \to k_\perp, \quad k_z c/\omega \to k_z,$$

where $\mathbf{r} = \{r,z\}$, $\mathbf{p} = \{p_\perp, p_z\}$ is the momentum, M is the mass, the equations of motion of a particle in the field (1) after averaging near the cyclotron resonance $(k_z p_{z0,s} + s\omega_H)/\gamma_{0,s} - 1 \approx 0$, where s is an integer, $\omega_H = eH_0/Mc\omega$, and $\gamma_{0,s}^2 = 1 + p_{\perp 0,s}^2 + p_{z0,s}^2$ (see Ref. 11), have the following form for not too small transverse particle momentum:

$$\frac{d}{dt}\tilde{\gamma} = \frac{\epsilon_0 p_{\perp 0,s}}{2\gamma_{0,s}} J_{m+s}(k_\perp r_{c,s}) J'_s(k_\perp \rho_{0,s})\mathrm{Im}[i^s \exp(i\tilde{\Theta}_s)], \quad \frac{d}{dt}\tilde{\Theta}_s = \frac{\tilde{\gamma}}{\gamma_{0,s}}(k_z^2 - 1), \quad (2)$$

where $\tilde{\gamma}$ is the deviation of the particle energy from $\gamma_{0,s}$, $\epsilon_0 = eE_0/Mc\omega$, $r_{c,s}$ is the radius of the guiding center of a particle, $\rho_{0,s} = p_{\perp 0,s}/\omega_H$ is the Larmor radius, and $\tilde{\Theta}_s$ is the resonant value of the helical phase of a particle in the field (1). The equations (2) are virtually identical to the analogous equations of Ref. 11, where the stochastic dynamics
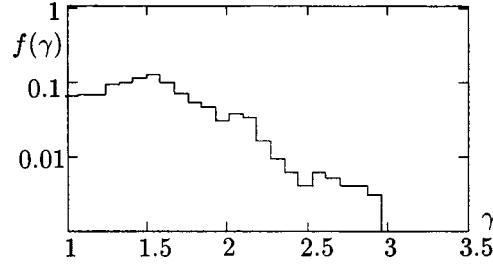
FIG. 1. Electron energy distribution function in a field of two oppositely traveling waves.

of particles in a uniform magnetic field and in the field of an electromagnetic plane wave were studied. The difference is the factor $0.5J_{m+s}(k_\perp r_{c,s})$ on the right-hand side of the first equation. If the transverse momentum is small, then Eqs. (2) become more complicated. The complete system of equations and its analysis are contained in Ref. 12.

Neighboring nonlinear cyclotron resonances overlap if

$$\left|\epsilon_0 p_{\perp 0,s}J_{m+s}(k_\perp r_{c,s})J'_s(k_\perp \rho_{0,s})\right|^{1/2}$$
$$+\left|\epsilon_0 p_{\perp 0,s+1}J_{m+s+1}(k_\perp r_{c,s+1})J'_{s+1}(k_\perp \rho_{0,s+1})\right|^{1/2} \gtrsim \omega_H/k_\perp \sqrt{2}. \qquad (3)$$

Let a particle be in cyclotron resonance with number s and let the conditions for the optimal resonance interaction hold: $m+s=0$, $r_{c,s}\approx 0$. Then the width of the nearest resonance with number $s\pm 1$ will be $\left|J_1(k_\perp r_{c,s+1})\right|^{-1/2}$ times smaller than the width of resonance s, i.e., the widths of the neighboring resonances are small. Moreover, for small $k_\perp$ the splitting between the resonances increases more rapidly ($k_\perp = 1$ is the nontransmission condition for the waveguide) than their width (the limit $k_\perp \rightarrow 0$ is an autoresonance, where the resonance line corresponds to an integral of motion[13]). For this reason it is difficult to achieve overlapping of cyclotron resonances — this requires a large field amplitude. Analytical estimates and numerical simulation for an $H_{1,1}$ wave and $a=8$ cm, $\omega/2\pi=2.8$ GHz, and $H_0=1$ kG show that resonances do not overlap all the way up to $\epsilon_0\approx 1$ ($E_0\approx 300$ kV/cm).

Particle motion becomes chaotic for smaller ϵ_0, if an $H_{2,1}$ wave propagating counter to the wave $H_{1,1}$ is added. In this case the lines of particle resonances with the wave $H_{2,1}$, which cross lines of particle resonances with the wave $H_{1,1}$, appear in the (p_z,γ) plane. Analysis of the conditions for the development of stochastic nonlinearity shows that for the above parameters the instability develops for field intensities of the order of 24 kV/cm. Numerical analysis of the electron motion in the field of the two waves $H_{1,1}$ and $H_{2,1}$ confirms this result. The initial equations of motion were integrated numerically for 1000 particles. At $t=0$ the electrons are distributed randomly over the coordinates and the direction of the transverse velocity inside a cylinder of radius $a/8$ and length $2\pi/k_z$ located at the center of the waveguide, $\gamma(t=0)=1+10^{-4}$, $p_z(t=0)=0$, and the amplitudes of the $H_{1,1}$ and $H_{2,1}$ waves are the same: $\epsilon_0=0.08$, $a=8$ cm, $\omega/2\pi=2.8$ GHz, and $H_0=1$ kG. The particle distribution function at $t=200\pi$ is presented in Fig. 1. It is evident that the particles acquire substantial energy: $\gamma>1.5$ for more than half of all particles. The time dependences of the average energy $\langle\gamma\rangle$ of the particles and of the
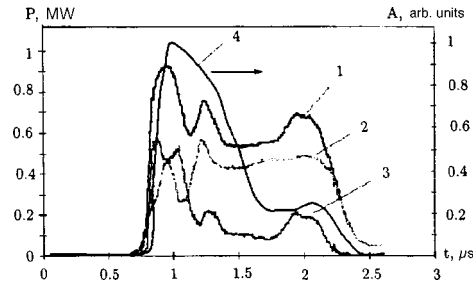
FIG. 2. Time dependence of the power of the incident wave (*1*), the power of the reflected wave (*2*), the absorbed power (*3*) in the cavity, and the x-ray intensity (*4*).

variance $\sigma^2 = \langle (\gamma - \langle \gamma \rangle)^2 \rangle$ show that $\langle \gamma \rangle$ increases to 1.6 and σ^2 to 0.12 in a time $t = 200\pi$. Similar results are obtained for particle motion in the fields of a circular cavity.

3. The experimental results are displayed in Figs. 2 and 3. Microwave power at frequency 2.7 GHz was fed into a plasma-filled cavity (density up to 10^9 cm^{-3}) where several characteristic modes were excited simultaneously. When the threshold value was reached (>450 kW), intense x-ray radiation was detected. The intensity reached its maximum value only for H_0 corresponding to ECR. The width of the x-ray resonance line at the 0.5 level is 10% of the resonant value H_0. All measurements presented below were performed with $H_0 = 0.97$ kG.

High-energy electrons and the x rays associated with them appear only when several modes are excited simultaneously. The mode composition of the cavity ($Q \sim 100$) was changed by varying the length of the cavity. The maximum x-ray intensity is observed with the excitation of the modes $H_{1,1,10}$ and $H_{2,1,8}$ (cavity length 60.8 cm), $H_{2,1,7}$ and $E_{0,1,8}$ (length 52.6 cm), and $H_{0,1,5}$ and $E_{1,1,5}$ (length 52.2 cm). A somewhat lower intensity is observed with the excitation of $H_{0,1,6}$ and $E_{1,1,6}$ (length 62.6 cm).

Figure 2 shows the time dependence of the power of the incident wave (*1*) and reflected wave (*2*), and the absorbed power (*3*) in a 60.8 cm long cavity. The time dependence of the x-ray intensity (*4*) has two peaks which virtually coincide with the peaks of the absorbed power in the cavity: 500–550 kW at 1 μs and 200 kW at 2 μs. The electron energy at the peak x-ray intensity is 100–150 keV at 2 μs and 8–10 times higher at 1 μs. The microwave power absorbed by the plasma at the peaks differs by only a
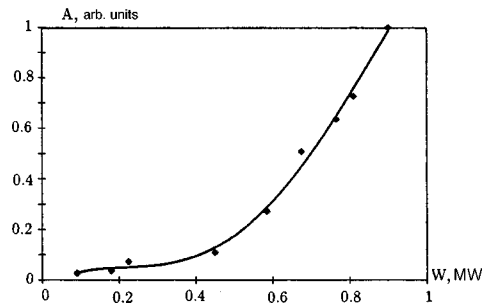

FIG. 3. Maximum x-ray intensity with excitation of $H_{1,1}$ and $H_{2,1}$ modes versus the power fed into the plasma.

factor of 2.5–3. This indicates the existence of a nonlinear dependence of the energy and number of accelerated electrons on the microwave power fed into the plasma and attests to a high efficiency of energy transfer from the microwave field to the plasma electrons. The maximum x-ray intensity is established in no more than 0.3 μs. This attests to a high rate of energy transfer to the plasma electrons from the excited oscillations. The dependence of the maximum x-ray intensity (cavity length 60.8 cm) on the power fed into the plasma is shown in Fig. 3. It is evident that appreciable growth of the radiation starts when the high-frequency power exceeds 450 kW. Above this point the growth rate of the x-ray intensity is eight or nine times higher, i.e., the increase in the x-ray intensity and therefore the heating of the plasma electrons are of a threshold character with respect to the microwave power fed into the plasma.

The curve of the x-ray intensity versus the plasma density has a maximum. Under optimal conditions the microwave power required for stochastic heating decreases. This can be explained by the appearance of a plasma resonance or by the excitation of characteristic plasma waves, whose presence facilitates the transition to stochasticity. The decrease in the x-ray intensity with a further increase of the plasma density is probably due to screening of the field by the plasma.

Investigation of plasma heating by two modes with different frequencies showed that this heating scheme is qualitatively no different from the heating scheme based on spatial modes with the same frequency. Heating at two frequencies is equivalent to increasing the power at one frequency when using several modes.

4. Therefore there exists the possibility of a simple experimental realization of the conditions for stochastic heating of plasma by the field of regular electromagnetic waves. This heating mechanism is exceptionally efficient — the rate of conversion of a substantial fraction of the energy of regular electromagnetic waves into the thermal energy of plasma electrons is high and the plasma electrons themselves reach relativistic energies.

Experimental investigations have shown that the basis of the heating mechanism is ECR. When H_0 was detuned from resonance by 10–20% in the experiment, virtually no plasma heating occurred. These results agree with the numerical and analytical calculations. Thus, numerical simulation of heating by the field of a standing $H_{1,1}$ wave has shown that for a 20% detuning from exact resonance electrons acquire virtually no energy.

The heating mechanism studied is a threshold mechanism. Substantial heating and correspondingly a substantial x-ray intensity were observed only above a certain threshold microwave intensity in the cavity. This is in good qualitative agreement with the theory. However, it should be noted that there is a discrepancy between the theoretical field intensity required for stochastic instability (24 kV/cm) and the experimentally observed threshold (of the order of 10 kV/cm). This discrepancy can be explained by the fact that the theory constructed is a single-particle theory of plasma heating and neglects collective processes, which can arise for sufficiently high plasma density. In the experiment, when the microwave field reaches an intensity of the order of 10 kV/cm additional ionization of the residual gas occurs, and the plasma density increases to 5×10^{10} cm^{-3} in the heating time. Plasma resonance as well as the characteristic plasma modes that can be excited in the plasma can play a large role under these conditions. Each of these factors decreases the microwave power level required for development of stochastic

instability of the motion of plasma particles. However, an adequate theory of these phenomena is lacking at present.

Stochastic heating is observed only with the excitation of several spatial modes in the cavity or with the excitation of the cavity by two frequencies. This is in complete agreement with the analysis of the theoretical models.

We shall now compare the above-described scheme of stochastic heating with the scheme implemented in traps with magnetic mirrors. In these devices there are two spatially limited regions where ECR conditions are satisfied. A particle acquires energy in one pass through the resonant region. This energy is low, and the change in energy can be described on the basis of a linear theory. The motion becomes stochastic as a result of collisions with other particles in the path from one mirror to the other. We shall compare the heating efficiency in this scheme with that of the scheme which we have examined above, assuming the charged particles to be constantly located in the resonant region. Then an effective collision frequency can be introduced. For the scheme with magnetic mirrors it is of the order of $\nu_{eff} \sim 1/T$, where T is the passage time of a particle between the mirrors. When dynamical chaos develops, the effective collision frequency and correspondingly the heating efficiency are much higher. It can be estimated as $\nu_{eff} \sim 1/T_C$, where $T_C \sim 1/\omega \cdot \ln K$ is the decorrelation time, K is the ratio of the width to the splitting between the nonlinear resonances, and T_C is comparable to the period of the rf field for $K > 1$. Therefore the heating of the plasma in a trap can be made substantially more efficient by introducing into the plasma trap an additional wave with specially chosen parameters. Indeed, under ordinary conditions the time during which a particle interacts with the field in one pass through the resonant region is of the order of 500 periods of the rf field.[14] As we have seen above, when dynamical chaos develops, this time is sufficient for the particle energy to change substantially.

*)e-mail: man@kipt.kharkov.ua

[1] V. E. Golant and V. I. Fedorov, *RF Plasma Heating in Toroidal Fusion Devices* (Plenum, New York, 1989) [Russian original, Énergoatomizdat, Moscow, 1986].

[2] *High-Frequency Plasma Heating*, edited by A. G. Litvak (AIP, New York, 1992).

[3] V. A. Buts and K. N. Stepanov, JETP Lett. **58**, 524 (1993).

[4] A. K. Nekrasov, Nucl. Fusion **10**, 387 (1970).

[5] A. J. Lichtenberg and M. A. Liberman, *Regular and Stochastic Motion* (Springer-Verlag, New-York, 1983) [Russian translation, Mir, Moscow, 1984].

[6] A. V. Timofeev, Fiz. Plazmy **1**, 88 (1975) [Sov. J. Plasma Phys. **1**, 47 (1975)].

[7] A. V. Timofeev, Fiz. Plazmy **3**, 913 (1977) [Sov. J. Plasma Phys. **3**, 516 (1977)].

[8] B. H. Quon, R. A. Dandl, W. DiVergilio *et al.*, Phys. Fluids **28**, 1503 (1985).

[9] A. V. Zvonkov and A. V. Timofeev, Fiz. Plazmy **15**, 552 (1989) [Sov. J. Plasma Phys. **15**, 320 (1989)].

[10] M. Yu. Glyavin, G. S. Nusinovich, T. B. Pankratova *et al.*, Vopr. At. Nauki Tekh. Ser. Termoyad. Sintez (Kharkov) **4**, 65 (1990).

[11] V. A. Balakirev, V. A. Buts, A. P. Tolstoluzhskiĭ, and Yu. A. Turkin, Zh. Éksp. Teor. Fiz. **95**, 1231 (1989) [Sov. Phys. JETP **68**, 710 (1989)].

[12] A. N. Antonov, V. A. Buts, E. A. Kornilov *et al.*, *Proceedings of the ICPP and 25th Conference on Controlled Fusion and Plasma Physics*, Praha, 29 June – 3 July, 1998, ECA **22C**, 248 (1998).

[13] V. A. Buts, O. V. Manuĭlenko, K. N. Stepanov, and A. P. Tolstoluzhskiĭ, Fiz. Plazmy **20**, 794 (1994) [Plasma Phys. Rep. **20**, 794 (1994)].

[14] A. J. Lichtenberg, *Phase-Space Dynamics of Particles* (John Wiley, New York, 1969) [Russian original, Atomizdat, Moscow, 1972].

Translated by M. E. Alferieff

A sharp decrease of resistivity in La$_{0.7}$Ca$_{0.3}$Mn$_{0.96}$Cu$_{0.04}$O$_3$: Evidence for Cu-assisted coherent tunneling of spin polarons

S. A. Sergeenkov and H. Bougrine

Bogoliubov Laboratory of Theoretical Physics, Joint Institute for Nuclear Research, 141980 Dubna, Moscow District, Russia

M. Ausloos and R. Cloots

SUPRAS, Institute of Physics, B5, University of Liège, B-4000 Liège, Belgium

Nearly a 50% decrease of the resistivity $\rho(T,x)$ is observed upon just 4% Cu doping at the Mn site of La$_{2/3}$Ca$_{1/3}$Mn$_{1-x}$Cu$_x$O$_3$. When the observed phenomenon is attributed to a decrease of the spin-polaron energy $E_\sigma(x)$ below $T_C(x)$, all of the data are found to be well fitted by the nonthermal coherent tunneling expression $\rho(T,x) = \rho_0 e^{-\gamma M^2(T,x)}$, assuming that the magnetization in the ferromagnetic state is given by the expression $M(T,x) = M_R(x) + M_0(x)\tanh\{\sqrt{[T_C(x)/T]^2 - 1}\}$. The best fits through all the data points suggest $M_0(x) \simeq \sqrt{1-x}M_0(0)$, $M_R(x) \simeq \sqrt{x}M_0(0)$, and $E_\sigma(x) \simeq E_\sigma(0)(1-x)^4$ for the explicit x dependence of the Cu-induced modifications of the Mn-spin-dominated zero-temperature spontaneous magnetization, residual paramagnetic contribution, and spin-polaron tunneling energy, respectively, with $E_\sigma(0) = 0.12$ eV. © *1999 American Institute of Physics.*
[S0021-3640(99)00811-7]

PACS numbers: 75.30.Kz, 72.80.Sk, 71.38.+i, 81.40.Rs

As is well known,[1] the ground state of La$_{2/3}$Ca$_{1/3}$MnO$_3$, which exhibits colossal magnetoresistance, is ferromagnetic (FM), and the paramagnetic–ferromagnetic transition is accompanied by a sharp drop in resistivity below T_C. This correlation is considered as a basic element for the so-called magnetically induced electron localization scenario,[2–4] in which the changes of observable resistivity at low temperatures are related to the corresponding changes of the local magnetization, and a coherent nonthermal tunneling charge carrier transport mechanism dominates other diffusion processes.

The effects of elemental substitution on the properties of La$_{2/3}$Ca$_{1/3}$MnO$_3$ have been widely studied in an attempt to further shed some light on the underlying transport mechanisms in this interesting material.[5–14] In particular, substitution of rare-earth atoms (like Y or Gd) in the La site leads to a lowering of the ferromagnetic (and ''metal–insulator'') transition temperature T_C, due mostly to the cation size mismatch.[5,11–14] At the same time, a reduction in T_C and a rather substantial drop of the resistivity in the FM
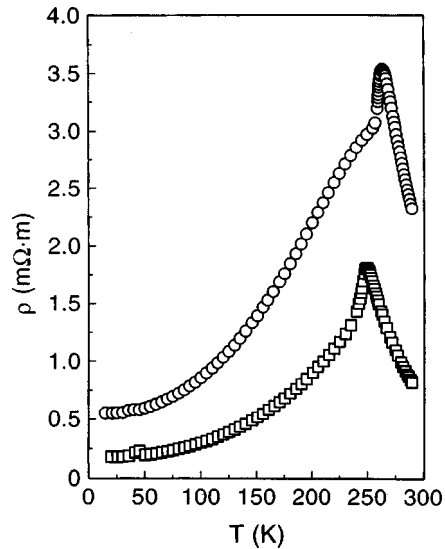
FIG. 1. Temperature behavior of the observed resistivity $\rho(T,x)$ in $La_{2/3}Ca_{1/3}Mn_{1-x}Cu_xO_3$ for $x=0$ (circles) and $x=0.04$ (squares).

region due to replacement of the Mn ions with metals (like Co or Ni) are ascribed to a weakening of the Zener double-exchange interaction between two unlike ions.[1,13] In other words, metal-ion doping was found[13] to decrease the polaron tunneling energy barrier, thus facilitating the transfer of carriers in the FM region.

In this letter we present a comparative study of resistivity measurements on two manganite samples from the $La_{2/3}Ca_{1/3}Mn_{1-x}Cu_xO_3$ family for $x=0$ and $x=0.04$ over a wide temperature interval (from 20 to 300 K). As we shall see, this very small amount of impurity leads to a marked (factor of two) drop in resistivity, which can hardly be understood in the framework of the conventional scattering theories. The data are in fact well fitted by a nonthermal spin tunneling expression for the resistivity, assuming a magnetization $M(T,x)$-dependent charge carrier correlation length $L(M)$.

The samples examined in this study were prepared by the standard solid-state reaction from stoichiometric amounts of La_2O_3, $CaCO_3$, MnO_2, and CuO powders. The necessary heat treatment was performed in air, in alumina crucibles at 1300° C for 2 days, to preserve the right phase stoichiometry. The powder x-ray diffraction patterns are characteristic of perovskites. No appreciable changes in the diffraction patterns induced by Cu doping have been observed (suggesting thus that no structural changes have occurred after replacement of Mn by Cu). Energy-dispersive x-ray microanalyses confirm the presence of copper on the manganese crystallographic sites.

The electrical resistivity $\rho(T,x)$ was measured using the conventional four-probe method. To avoid Joule and Peltier effects, a dc current $I=1$ mA was injected (as a one second pulse) successively on both sides of the sample. The voltage drop V across the sample was measured with high accuracy by a KT256 nanovoltmeter. Figure 1 presents the temperature dependence of the resistivity $\rho(T,x)$ for two $La_{2/3}Ca_{1/3}Mn_{1-x}Cu_xO_3$ samples, with $x=0$ and $x=0.04$, respectively. Notice a rather sharp (nearly a 50%) drop

of resistivity (both near the peak and on its low temperature side) for the doped sample, along with a small reduction of the transition (peak) temperature $T_C(x)$, which reaches $T_C(0) = 265\,\mathrm{K}$ and $T_C(0.04) = 250\,\mathrm{K}$, respectively. The kink-like behavior in the resistivity of the Cu-free sample seen just below $T_C(0)$ is most likely due to a slight oxygen-nonstoichiometry-induced grain-boundary (GB) scattering.[12] It completely disappears upon doping, suggesting[14] a healing role of copper in reducing the GB resistivity (see below).

Since no tangible structural changes have been observed upon copper doping, the Jahn–Teller mechanism can be safely ruled out, and the most reasonable cause for the resistivity drop in the doped material is the reduction of the spin-polaron tunneling energy E_σ, which within the localization scenario[2–4] is tantamount to an increase of the charge carrier correlation length $L \simeq \hbar / \sqrt{2mE_\sigma}$ (here m is an effective polaron mass). In the FM region [below $T_C(x)$] the tunneling-based resistivity is[2,3] $\rho[M(T,x)] = \rho_s e^{2R/L(M)}$, with $\rho_s^{-1} = e^2 R^2 \nu_{\mathrm{ph}} N_m$, where R is the tunneling distance (and $2R$ is the size of a small spin polaron), ν_{ph} is the phonon frequency, and N_m is the density of available states. In turn, the correlation length $L(M)$ depends on the temperature and copper concentration x through the corresponding dependences of the magnetization $M(T,x)$. Assuming, along the basic lines of the conventional mean-field approximation scheme,[3] that $L(M) = L_0/(1 - M^2/M_L^2)$ [with M_L being the fraction of the saturation magnetization $M(0)$], we arrive at the following expression for the tunneling-dominated resistivity:

$$\rho(T,x) = \rho_0 e^{-\gamma M^2(T,x)}, \tag{1}$$

with $\rho_0 = \rho_s e^{2R/L_0}$ and $\gamma = 2R/L_0 M_L^2$.

To account for the observed behavior of the resistivity, we identify T_C with the doping-dependent Curie temperature $T_C(x)$, and assume that the temperature and x dependence of the magnetization is the sum of a classical Curie–Weiss contribution and a residual term, namely

$$M(T,x) = M_R(x) + M_0(x)\tanh\{\sqrt{[T_C(x)/T]^2 - 1}\}. \tag{2}$$

Specifically, $M_R(x)$ is interpreted as a copper-induced residual paramagnetic contribution, while $M_0(x)$ takes into account the deviation of the ferromagnetically aligned Mn magnetic moments of the undoped material in the presence of copper atoms. In fact, save for the $M_R(x)$ term, Eq. (2) is an analytical (approximate) solution of the well-known Curie–Weiss mean-field equation for the spontaneous magnetization, viz., $M(T,x)/M(0,x) = \tanh\{[M(T,x)/M(0,x)](T_C(x)/T)\}$. Among the possible reasons for the observed sharp decline of resistivity in the Cu-doped sample is also the electronic nature of its grain boundary (GB). Indeed, since $Cu(d^9)$ has a substantially larger ionic radius than the Mn ion, it may actually improve the GB conduction (through a relieving of the local strain), eventually reducing the overall resistivity Ref. 14. In order to exclude any such extrinsic effects (related to GB scattering), we consider the normalized resistivity $\Delta\rho(T,x)/\Delta\rho(0,x)$, where $\Delta\rho(T,x) = \rho(T,x) - \rho(T_C(x),x)$ and $\rho(0,x)$ is the resistivity taken at the lowest available temperature. Figure 2 depicts the above-defined normalized resistivity versus the reduced temperature $T/T_C(x)$ for the two samples. First of all, notice that the data for $x=0$ and $x=0.04$ merge both at low temperatures and above $T_C(x)$. The latter suggests the absence of GB-related effects in the normalized resistivity.
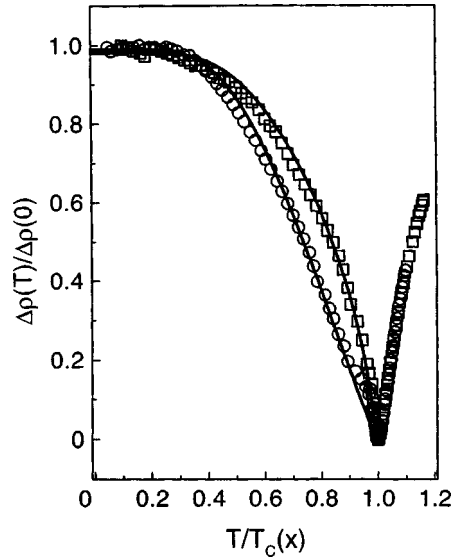
FIG. 2. The temperature dependence of the normalized resistivity $\Delta\rho(T,x)/\Delta\rho(0,x)$ in $La_{2/3}Ca_{1/3}Mn_{1-x}Cu_xO_3$ for $x=0$ (circles) and $x=0.04$ (squares) as a function of the reduced temperature $T/T_C(x)$. The solid lines through all the data points are the best fits according to Eqs. (1) and (2).

At the same time, starting from $T_C(x)$ and below, the Cu-doped (squares) and Cu-free (circles) samples follow different routes. In particular, approaching $T_C(x)$ from low temperatures, a (most likely) oxygen-nonstoichiometry-driven[12] crossover from the un-doped to the doped transport mechanism is clearly seen near $T/T_C(x)\simeq0.9$. On the other hand, the fact that the data below $T_C(x)$ fail to merge suggests the presence of some magnetic-structure-related scattering mechanism, probably due to Cu-spin-induced modifications (domains) in the FM structure of the undoped sample. The solid lines are the best fits through all the data points according to Eqs. (1) and (2), yielding $M_0(0)/M_L = 1.41\sqrt{L_0/2R}$, $M_R(0)=0$, $M_0(0.04)=0.98M_0(0)$, and $M_R(0.04)=0.06M_0(0)$ for the model parameters. Recalling that in our present study the copper content is $x=0.04$, the above estimates can be cast (with a rather good accuracy) into the following explicit x dependences of the residual $M_R(x)\simeq\sqrt{x}M_0(0)$ and spontaneous $M_0(x)\simeq\sqrt{1-x}M_0(0)$ magnetizations, which lead to an exponential (rather than power-law) x dependence of the observed resistivity $\rho(T,x)$ [see Eqs. (1) and (2)]. Furthermore, assuming (as usual[2]) that the ratio of the (undoped) tunneling distance to the correlation length has a value $2R/L_0\simeq1$ and using the value found for the residual resistivity $\rho(T_C(0),0)=\rho_0\simeq3.5$ mΩm, the density of states[2] $N_m\simeq9\times10^{26}$ m^{-3}eV^{-1}, and the phonon frequency $\nu_{ph}\simeq2\times10^{13}$ s^{-1} (estimated from the Raman shift for optical Mn–O modes), we obtain $R\simeq5$ Å for an estimate of the tunneling distance (corresponding to $2R\simeq10$ Å for the size of a spin polaron) which in turn results in $L_0\simeq10$ Å (when the free-electron approximation is used for the mass m of a polaron) and $E_\sigma(0)\simeq0.12$ eV for the zero-temperature copper-free carrier charge correlation length and for the spin-polaron tunneling energy, respectively, both in good agreement with reported[1–5,9,13] estimates of these parameters in other systems. Based on the above estimates, we can roughly estimate the copper-induced variation of the correlation length $L(x)$ and the corresponding spin polaron tunneling

energy $E_\sigma(x)$. Indeed, according to the earlier introduced definitions, $L[M(T_C(x))]$ $=L_0/(1-M_R^2(x)/M_L^2)\simeq L_0/(1-2x)$ and $E_\sigma(x)\propto L^{-2}(x)$, which lead to $L(x)$ $\simeq L(0)/(1-x)^2$ and $E_\sigma(x)\simeq E_\sigma(0)(1-x)^4$ for small enough x. These explicit x dependences [along with the composition variation of the transition temperature $T_C(x)$ $\simeq T_C(0)(1-x)$] correlate remarkably well with the recently observed[13,14] transition-element (T) induced changes in $La_{2/3}Ca_{1/3}Mn_{1-x}T_xO_3$.

In summary, a rather substantial drop in resistivity $\rho(T,x)$ in a lightly Cu doped manganite $La_{2/3}Ca_{1/3}Mn_{1-x}Cu_xO_3$ sample is reported. Along with a lowering of the Curie point $T_C(x)$, the copper substitution is argued to add a small paramagnetic contribution $M_R(x)$ to the Mn-spin-dominated spontaneous magnetization M of the undoped material, leading to a small decrease of the spin-polaron tunneling energy $E_\sigma(x)$. However, due to the tunneling-dominated carrier transport process, this small amount of impurity is sufficient to cause drastic changes in the absolute value of the resistivity across the whole temperature range. The temperature and x dependences of the observed resistivity was found to be rather well fitted by a nonthermal coherent tunneling of spin polarons, with a heuristic expression for the magnetization $M(T,x)$ in the ferromagnetic state (as an approximate analytical solution to the mean-field Curie–Weiss equation), resulting in an exponential (rather than linear) doping dependence of $\rho(T,x)$.

[1] For a recent review on the subject, see, e.g., M. Jaime and M. B. Salamon, http://xxx.lanl.gov/abs/cond-mat/9901081 and further references therein.
[2] M. Viret, L. Ranno, and J. M. D. Coey, Phys. Rev. B **55**, 8067 (1997).
[3] L. Sheng, D. Y. Xing, D. N. Sheng *et al.*, Phys. Rev. Lett. **79**, 1710 (1997).
[4] L. P. Gor'kov and V. Z. Kresin, JETP Lett. **67**, 985 (1998).
[5] J. Fontcuberta, M. Martinez, A. Seffar *et al.*, Phys. Rev. Lett. **76**, 1122 (1996).
[6] N. A. Babushkina, L. M. Belova, O. Yu. Gorbenko *et al.*, Nature (London) **391**, 159 (1998).
[7] N. A. Babushkina, L. M. Belova, V. I. Ozhogin *et al.*, J. Appl. Phys. **83**, 7369 (1998).
[8] A. M. Balagurov, V. Yu. Pomyakushin, D. V. Sheptyakov *et al.* JETP Lett. **69**, 46 (1999).
[9] J. Fontcuberta, V. Laukhin, and X. Obradors, Appl. Phys. Lett. **72**, 2607 (1998).
[10] T. T. M. Palstra, A. P. Ramirez, S-W. Cheong *et al.*, Phys. Rev. B **56**, 5104 (1997).
[11] H. Y. Hwang, S-W. Cheong, P. G. Radaelli *et al.*, Phys. Rev. Lett. **75**, 914 (1995).
[12] J.-Q. Wang, R. C. Barker, G.-J. Cui *et al.*, Appl. Phys. Lett. **71**, 3418 (1997).
[13] M. Rubinstein, D. J. Gillespie, J. E. Snyder *et al.*, Phys. Rev. B **56**, 5412 (1997).
[14] K. Ghosh, S. B. Ogale, R. Ramesh *et al.*, Phys. Rev. B **59**, 533 (1999).

Space−time characteristics of nuclear resonant excitation during Bragg reflection from multilayers

M. A. Andreeva

M. V. Lomonosov Moscow State University, 119899 Moscow, Russia

Mössbauer experiments using synchrotron radiation have opened up a new method for investigating nuclear-resonance scattering — in the time domain. It is shown that the field distribution in a multilayer structure, including periodic interlayers of a resonant isotope, under Bragg reflection conditions is substantially different in the energy and time differential regimes of investigation. For separate delay times the field does not decay into the medium, but rather it undergoes complicated dynamic beats. The positions of the antinodes of the ''energy'' and ''temporal'' standing waves are also different. In consequence the energy (Mössbauer) and temporal spectra of nuclear resonant reflection contain substantially different information about the structure of the films. © *1999 American Institute of Physics.*

[S0021-3640(99)00911-1]

PACS numbers: 76.80.+y, 71.70.Jp, 68.65.+g

Effects due to the collective excitation of low-energy (Mössbauer) nuclear levels under conditions of coherent scattering of resonance radiation are a subject of continuing interest. The suppression of inelastic channels of nuclear reactions (Kagan–Afanas'ev effect) during diffraction of Mössbauer radiation by crystals containing Mössbauer nuclei was predicted and studied experimentally in the 1970s (Ref. 1; see also the reviews in Refs. 2 and 3). In recent years the use of sharply directed synchrotron radiation (SR) has greatly expanded the possibilities of investigating coherent effects in nuclear resonant scattering. Mössbauer experiments with SR have reached a qualitatively new level: nuclear-resonance scattering can now be investigated in the time domain, since SR is characterized by a virtually white spectrum and possesses a pulsed structure (see Ref. 4 for a more detailed discussion of the experimental implementation of nuclear resonant experiments using SR). New manifestations of collective effects, such as enhancement and speedup of the decay of a nuclear system, dynamic beats, acoustic modulation, and modulation by an ac magnetic field, were immediately observed in Bragg reflection from Mössbauer crystals as well as in forward scattering.[5–7]

In the present letter the unusual distribution of the radiation field in a periodic multilayer resonance medium under Bragg reflection conditions for a time-differential method of investigation is examined theoretically.

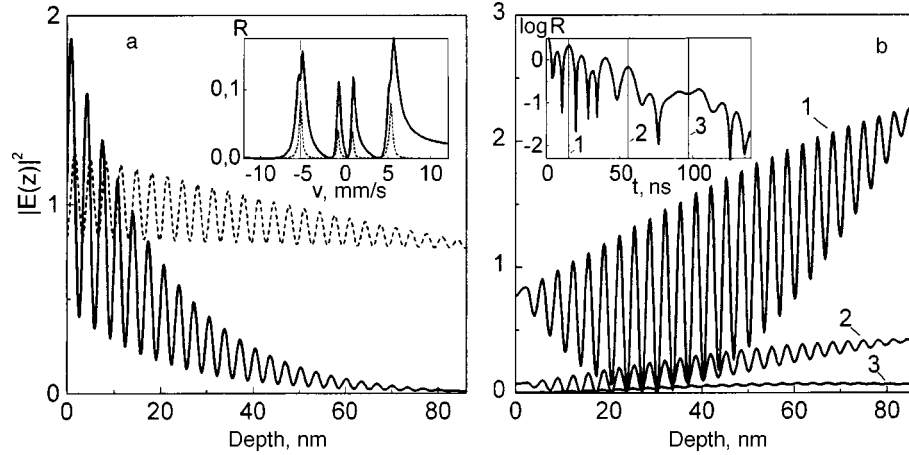The calculation was performed for 26 Cr(1.7 nm)/^{57}Fe(1.6 nm) bilayers with a 3.3

FIG. 1. Distribution $|E(z)|^2$ of the radiation field in a $[\text{Cr}(1.7 \text{ nm})/^{57}\text{Fe}(1.6 \text{ nm})]_{26}$ multilayer film on glass under Bragg reflection conditions ($\theta = \theta_B$) for energy-differential (a) and time-differential (b) regimes of investigation. Insets: The solid lines represent, respectively, the energy (left-hand panel) and time (right-hand panel, logarithmic scale) reflection spectra R at $\theta = \theta_B$; the thin solid lines represent the energy ($v = -5.31$ mm/s) or the time delay after an instantaneous excitation pulse (1 — $t = 15.2$ ns, 2 — $t = 55.7$ ns, 3 — $t = 97.1$ ns) for which the field distribution is presented; the dashed line in the inset in left-hand panel shows the theoretical nuclear resonant absorption spectrum (on an arbitrary scale). The dashed line in panel (a) shows the distribution of the field in a periodic structure in the absence of a nuclear resonant interaction.

nm period on a glass substrate. A Bragg reflection peak from this structure for resonant radiation wavelength 0.086 nm appeared at a grazing angle $\theta = \theta_B = 13.545$ mrad. Magnetic hyperfine splitting in the iron layers was taken as in the α-Fe phase, and it was assumed that the second and fifth lines of the magnetic spectrum are absent, which happens for in-plane orientation of the magnetic moments of the iron atoms in the films, grazing geometry of the experiment, and σ polarization of the radiation (see the dashed spectrum in the inset in Fig. 1a). The computational scheme was as follows: The energy (Mössbauer) spectrum $E_R(\omega)$ of the amplitude of the mirror reflection for a fixed grazing angle was calculated taking account of nuclear resonant interaction; thus the amplitude of the radiation field at the surface was known: $E(z=0,\omega) = E_0 + E_R(\omega)$ (E_0 is the amplitude of the incident wave). Next, the energy spectrum of the amplitude of the radiation field was systematically calculated (with step $\Delta z = 0.1$ nm) at each depth, starting at $z = 0$, using propagation matrices.[8] With the use of the Fourier transform

$$E(z,t) = \frac{1}{2\pi} \int_{-\infty}^{+\infty} E(z,\omega) e^{-i\omega t} d\omega, \quad \omega = E_\gamma/\hbar,$$

the time spectrum of the field amplitude $E(z,t)$ was compared with each spectrum $E(z,\omega)$.[9,7] Despite the apparent equivalence of these two regimes (energy and temporal) of investigation, the character of the variations in $E(z,\omega = \text{const})$ and $E(z,t = \text{const})$ with depth was found to be completely different (Figs. 1 and 2). The amplitude and oscillations of $|E(z,\omega = \text{const})|^2$, as expected, decay quite rapidly with depth (more rapidly than in the absence of the nuclear-resonance interaction channel), whereas $|E(z,t = \text{const})|^2$ increases (!) with depth down to the lower limit of the periodic resonance structure studied. That is, at some particular instant of delay time after an instantaneous pulse the
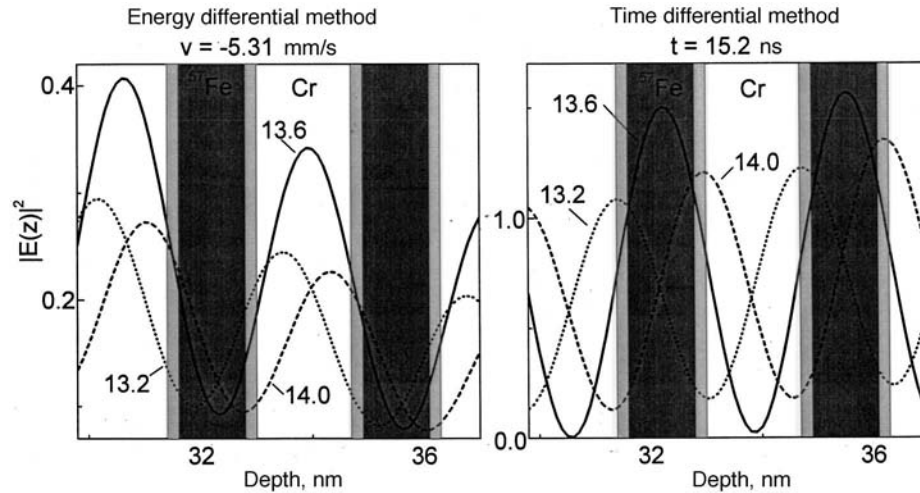
FIG. 2. Displacements of the antinodes of the field relative to the resonant layers (the central part of the structure under study is shown on an enlarged scale) as a function of the grazing angle θ near the Bragg angle θ_B for $v = -5.31$ mm/s (left-hand side) and $t = 15.2$ ns (right-hand side). For each curve in the figure the grazing angles are given in milliradians.

excitation of the system is maximum not at the surface of the reflecting structure but rather in the interior volume of the structure. We also note that oscillations of the intensity $|E(z,t)|^2$ reach a maximum at the center of the film.

The positions of the antinodes of the standing waves $|E(z, \omega = \text{const})|^2$ and $|E(z, t = \text{const})|^2$ are also completely different (Fig. 2). Oscillations of $|E(z, \omega = \omega_{\text{res}})|^2$ for exact resonance have a minimum at the center of the resonant layers, as a result of which the reflection coefficient at resonance increases (this effect is similar to the enhancement of reflection from absorbing periodic structures, described in Ref. 10; there is also an analogy with the well-known suppression of inelastic channels of a nuclear reaction[1–3]). In the time-differential interaction, the antinodes of $|E(z, t = \text{const})|^2$ at the instants t of delay time considered (see inset in Fig. 2, right-hand side), i.e., at the maxima of the oscillations of the temporal spectrum of the Bragg reflection coefficient, occur in the resonance layers, and this enhances the interaction with the nuclear-resonant layers. However, it should be noted that for other energy shifts relative to the resonance or at other instants of delay time, the phase of the oscillations of the field relative to the resonant layers is different, since on the whole the shape of the energy or time spectra of the squared modulus of the field amplitude varies dramatically at a depth of one bilayer.[11] This circumstance can be used to investigate secondary radiation for localization of impurity atoms.

The increase in the field amplitude with depth can be qualitatively explained by multiple scattering with a delay determined by the lifetime of the nuclear level. Nuclei at depth z at a certain point in time are excited by the initial pulse (decay has not yet occurred) and by the reemission from other nuclei, which occurs with a delay; on the whole, this increases the probability of excited nuclei being present at large depths. Mathematically, this effect is characteristic for processes described by a multiple convo-

lution in time. Indeed, the amplitude at each point is described by the product of the propagation matrix and the field amplitude at the surface. But the product of two frequency-dependent functions is replaced in the time representation by their convolution. Such an analysis for forward scattering is presented in Ref. 12. Rescattering processes are more complicated under reflection conditions, since the presence of coherent waves in the forward and backward directions must be taken into account (which corresponds to a transformation of the components of the field amplitude with depth using a matrix exponential). For this reason, this behavior of $|E(z,t)|^2$ was difficult to predict without direct calculations.

We note that an increase in the amplitude of the radiation field during propagation through a resonant absorber has already been observed in measurements in the time domain. Thus, even investigations of the time spectra of the decay of Mössbauer nuclei in the delayed coincidence method[13,14] have shown that at individual points in time the amplitude of a wave transmitted through a resonant absorber can be greater than the amplitude determined by the natural decay of the absorber. For time spectra of forward scattering excited by a synchrotron pulse the variations in the field amplitude with increasing thickness of the resonant scatterer have been investigated theoretically in Refs. 7, 12, and 15. It was observed, specifically, that in both the time differential and time-integrated regimes this amplitude grows until the photoelectric absorption predominates.

It is of interest to investigate whether or not similar limitations on the increase in the amplitude of the radiation field are present in our case of a periodic multilayer Bragg reflector. For this we increased the number of periods of the structure until full saturation of the field amplitude $|E(z,t=\text{const})|^2$ with depth occurred (Fig. 3). It follows from the calculation that saturation is reached for different time delays at different depths. In addition, the subsequent decay of the field is nonmonotonic; here unique dynamic beats of the field with depth occur. Nothing like this can occur in the energy domain.

The characteristic features, examined above, of the space–time structure of the radiation field in a periodic resonant medium are also of interest for practical applications.

In the first place, we have shown that the depth from which information is extracted in Bragg reflection is different for the energy and time methods of investigation. This explains the complexity of the simultaneous analysis of Mössbauer and time reflection spectra measured on the same sample on the assumption of the same model for the variation of the hyperfine interactions over film depth.[16,17]

In the second place, the contribution of scattering at interfaces is enhanced in the energy spectra of exact Bragg reflection, while the contribution from the central part of the resonant films predominates in the time reflection spectra. As the grazing angle θ varies near the Bragg angle θ_B, the position of the antinodes of $|E(z,t=\text{const})|^2$ shifts, as always happens in the standing-wave method (Fig. 2), and since the modulation amplitude of $|E(z,t=\text{const})|^2$ is much greater than $|E(z,\omega=\text{const})|^2$ (at least at the center of a multilayer film), successive ''de-excitation'' of different regions in the resonant ^{57}Fe layers should be the more striking effect. Thus, if the hyperfine interactions at the center of the ^{57}Fe layers and interfaces are different (which apparently always happens), the time reflection spectra will differ very strongly for θ near θ_B. There are no fundamental difficulties in performing such selective investigations over the depth of a resonant layer
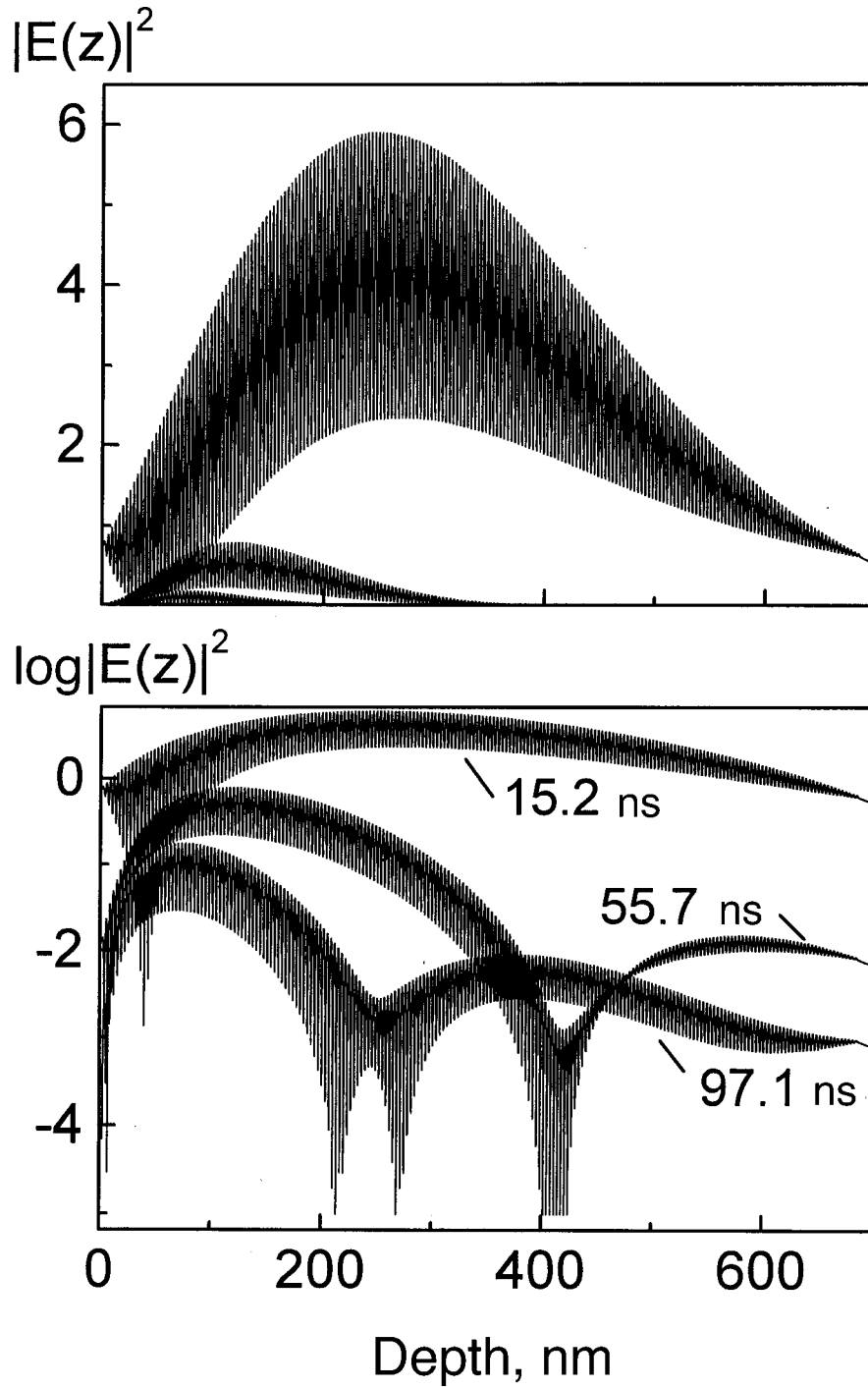
FIG. 3. Distribution $|E(z,t = \text{const})|^2$ of the radiation field in ordinary and logarithmic scales under Bragg reflection conditions $\theta = \theta_B$ for the same three points in time as in the right-hand panel in Fig. 1 but for a much thicker periodic structure (the number of periods is eight times greater than in Fig. 1: $N = 208$).

in multilayer periodic structures, since the divergence of the SR, ($\sim 20–30$ μrad) is much smaller than the width of the Bragg reflection, and angular alignments on the Mössbauer SR stations are very accurate.

Finally, the dramatic change in the shape of the time spectrum $|E(z, t = \text{const})|^2$ (just as $|E(z, \omega = \text{const})|^2$ also) as a function of z within one bilayer makes it possible to localize the position of an impurity in the structure according to the shape of the ''M'óss-bauer spectrum'' of the fluorescence of the impurity, as is done in the x-ray standing wave method.[18,19]

I thank A. I. Chumakov and G. V. Smirnov for a discussion of the results.

[1] A. M. Afanas'ev and Yu. Kagan, Zh. Éksp. Teor. Fiz. **64**, 1958 (1973) [Sov. Phys. JETP **37**, 987 (1973)].

[2] G. V. Smirnov, Hyperfine Interact. **27**, 203 (1986).

[3] Yu. V. Shvyd'ko and G. V. Smirnov, J. Phys.: Condens. Matter **1**, 10563 (1989).

[4] R. Rüffer and A. I. Chumakov, Hyperfine Interact. **97/98**, 589 (1996).

[5] U. van Bürck, R. L. Mössbauer, E. Gerdau et al., Phys. Rev. Lett. **59**, 355 (1987).

[6] G. Faigel, D. P. Siddons, J. B. Hastings et al., Phys. Rev. Lett. **61**, 2794 (1988).

[7] G. V. Smirnov, Hyperfine Interact. **97/98**, 551 (1996).

[8] M. A. Andreeva, S. M. Irkaev, and S. M. Semenov, Zh. Éksp. Teor. Fiz. **105**, 1767 (1994) [JETP Lett. **78**, 956 (1994)].

[9] Yu. Kagan, A. M. Afanas'ev, and V. G. Kohn, Phys. Lett. **68A**, 339 (1978).

[10] E. Spiller, Appl. Phys. Lett. **20**, 365 (1972).

[11] M. A. Andreeva, Poverkhnost' (1999), in press.

[12] W. Sturhahn, K. W. Quast, T. S. Toellner et al., Phys. Rev. B **53**, 171 (1996).

[13] F. J. Lynch, R. E. Holland, and M. Hamermesh, Phys. Rev. **120**, 513 (1960).

[14] M. Haas, V. Hizhnyakov, and E. Realo, Phys. Lett. A **124**, 370 (1987).

[15] G. V. Smirnov, in Nuclear Resonance Scattering of Synchrotron Radiation, edited by E. Gerdau, (Baltzer, 1999).

[16] M. A. Andreeva, S. M. Irkaev, V. G. Semenov et al., J. Alloys Compounds (1999), in press.

[17] V. G. Semenov, M. A. Andreeva, S. M. Irkaev et al., Izv. Akad. Nauk, Ser. Fiz. (1999), in press.

[18] M. V. Koval'chuk and V. G. Kon, Usp. Fiz. Nauk **149**, 69 (1986) [Sov. Phys. Usp. **29**, 426 (1986)].

[19] S. I. Zheludeva, M. V. Koval'chuk, N. N. Novikova et al., Poverkhnost', No. 1, 28 (1999).

Translated by M. E. Alferieff

Mechanism of the formation of a diamond nanocomposite during transformations of C_{60} fullerite at high pressure

V. V. Brazhkin, A. G. Lyapin, R. N. Voloshin, and S. V. Popova

Institute of High-Pressure Physics, Russian Academy of Sciences, 142092 Troitsk, Moscow District, Russia

Yu. A. Klyuev and A. M. Naletov

All-Russia Scientific-Research Institute for Diamonds, 119110 Moscow, Russia

S. C. Bayliss and A. V. Sapelkin

Solid State Research Center, De Montfort University, Leicester, LE1 9BH, England

The results of an investigation of the transformation of C_{60} fullerite to diamond under pressure through intermediate three-dimensionally polymerized and amorphous phases are reported. It is found that treatment of fullerite C_{60} at pressures 12–14 GPa and temperatures $\sim 1400\,°C$ produces a nanocrystalline graphite–diamond composite with a concentration of the diamond component exceeding 50%. At lower temperatures (700–1200 °C) nanocomposites consisting of diamondlike (sp^3) and graphitic (sp^2) amorphous phases are formed. The nanocomposites obtained have extremely high mechanical characteristics: hardness comparable to that of best diamond single crystals and fracture resistance two times greater than that of diamond. Mechanisms leading to the transformation of C_{60} fullerite into diamond-based nanocomposites and the reasons for the high mechanical characteristics of these nanocomposites are discussed. © *1999 American Institute of Physics.* [S0021-3640(99)01011-7]

PACS numbers: 81.05.Tp, 81.05.Ys, 81.40.Vw

1. Diamond and diamond-containing materials are attracting a great deal of attention from investigators and technologists because of the unique intrinsic mechanical properties of such materials. Artificial diamonds are ordinarily synthesized from a carbon–graphite phase that is stable under normal conditions. At the same time, from the standpoint of fundamental investigations and for technological applications it is of enormous interest to study the possibility of synthesizing diamond from metastable carbon phases. The production of a new, highly metastable, ordered phase of carbon — fullerite C_{60} — in macroscopic quantities[1] has led to new possibilities for synthesizing diamondlike carbon phases.[2]

A direct graphite–diamond transformation without special catalysts occurs, for kinetic reasons, far from the line of thermodynamic equilibrium ($T > 2000$ K at $P \sim 12$

GPa).[3] Metastable phases of carbon, such as soot, fullerites, and carbynes, have a conditional thermodynamic equilibrium with diamond at pressures much lower than the diamond–graphite equilibrium pressure. For fullerite C_{60} a conditional equilibrium with diamond is reached in general at negative pressures.[4] However, a decrease of the thermodynamic equilibrium pressure does not yet signify a decrease of the pressure (or temperature) of the real transition, since the kinetics and microscopic mechanism of the transition play a very important role in a real structural transformation. From this standpoint it is extremely interesting to investigate the transformation of fullerite C_{60} into diamond.

It has been established previously that heating of fullerite C_{60} at various pressures results in a one- (1D), two- (2D), or three-dimensional (3D) polymerizations of the molecular crystal, and with further heating the polymer phases transform into amorphous modifications of carbon with destruction of the molecular structure of C_{60}.[3,5–8] The amorphous carbon obtained from C_{60} contains an appreciable fraction of atomic sp^3 states at pressures 8–9 GPa, where crossover is observed between temperature-induced 2D and 3D polymerizations.[8,9] However, the amorphous network becomes predominantly fourfold coordinated only at pressures 12–13 GPa.[4,8,9] As a result, an appreciable yield of diamonds from C_{60} without intermediate graphitization is kinetically realizable only at $P > 12$ GPa.

It is well known that many mechanical properties of polycrystals improve as the grain size decreases (see Ref. 10 and references cited therein). In this connection, it is of enormous interest to synthesize diamond-based nanocomposites. However, because of residual porosity, chemical impurities, and residual stresses at grain boundaries the standard methods of compacting diamond nanopowders do not yield composites with high mechanical characteristics. An alternative method for obtaining a nanocrystalline state is crystallization of the corresponding amorphous phase. A distinctive feature of amorphous carbon modifications is that the average coordination number in them can actually vary from 2 to 4.[9] It is natural to assume that amorphous phases with a large fraction of fourfold coordinated sp^3 states are preferred for obtaining diamond nanocomposites. Up to now amorphous modifications of carbon with a large fraction of sp^3 states have been synthesized only in the form of thin films.[11] The transformations of fullerite C_{60} which were discussed above open up new possibilities for obtaining three-dimensional samples of amorphous diamondlike carbon. Our objective in the present work was to investigate fullerite–diamond transformations via an intermediate amorphous phase and to investigate the mechanical properties of diamond nanocomposites.

2. The samples were synthesized from fullerite powder with a C_{60} content of at least 99.9% and crystalline grain size ~ 100 μm. A Toroid chamber with a modified profile was used to produce a high pressure. The chamber could produce pressures of up to 14 GPa in a volume of up to 20 mm^3. Micron-size Fe_2O_3 powder, which increased friction, was used to decrease the outflow of the catlinite interlayer between the high-pressure chambers and to obtain the maximum pressure at the chamber–interlayer interface. Heating was performed by passing a current through a heater into which a Pt container with a fullerite sample (C_{60} powder compacted into a cylinder 2 mm high and 2 mm in diameter) was placed. The structure of the samples obtained was investigated by x-ray diffraction (CuK_{α} and CrK_{α}). The density of the samples was determined by a pycnometric method. The mechanical properties were investigated by indentation with diamond
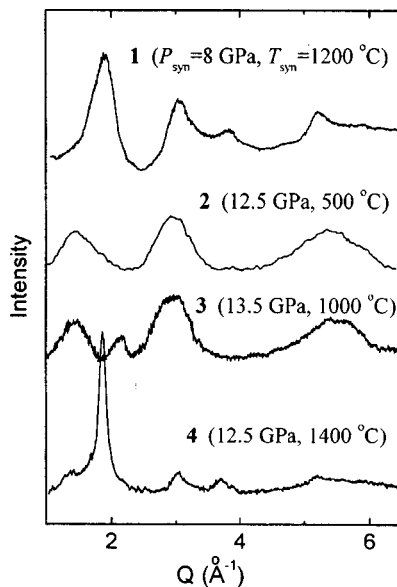
FIG. 1. X-ray diffraction patterns (with the background subtracted out) for amorphous and nanocomposite samples obtained by heating C_{60} up to various temperatures T_{syn} under pressure P_{syn} (GPa) followed by quenching. The intensity is shown as a function of the scattering wave vector $Q = 4\pi\sin\theta/\lambda$.

Vickers pyramids at loads up to 5.5 N. Calculations of the Vickers hardness H_v and the critical stress intensity coefficient (fracture resistance) K_{1c} were performed using the method proposed in Ref. 12 and successfully used for investigating ultrahard materials.

3. X-ray diffraction data for several amorphous and nanocrystalline samples are presented in Fig. 1. For comparison, the diffraction pattern of a sample obtained by the disordering of C_{60} at $T = 8$ GPa, i.e., in the region of 1D and 2D polymerizations, is shown by curve *1*. This curve corresponds to a disordered graphitic state, which is confirmed by the density of this sample, ≈ 2.2 g/cm^3. Substantially different diffraction patterns are observed for amorphous samples obtained at 12.5–13.5 GPa (in the region of 3D polymerization). The wide amorphous peak near 3 Å^{-1} indicates the presence of a substantial fraction of atoms in the sp^3 states (in what follows we shall refer to such samples as diamondlike amorphous). This corresponds to a high density and extremely high hardness of the samples (Table I).

It should be noted that the mechanism leading to the formation of an amorphous phase at $P = 12.5–13.5$ GPa is substantially different from the mechanism of disordering in the low-dimensional polymerization range ($P \leqslant 8$ GPa). Indeed, gradual 3D polymerization culminates in the formation of an amorphous phase whose diffraction pattern does not contain the peak near 2 Å^{-1} corresponding to a graphitic, predominantly layered, packing of atoms (compare curves *1* and *2* in Fig. 1). A diffraction peak close to the (002) reflection of graphite but displaced rightward in angle (curve *3*) appears only at higher temperatures. The corresponding interplanar distance ≈ 3 Å is 10% less than the distance between the planes in graphite (≈ 3.3 Å). From the width of the amorphous peaks one can estimate the mean order length l in the disordered phase using the relation

TABLE I. The density ρ, hardness H_v, and fracture resistance K_{1c} (measured with various loads P on the indenter) of amorphous and nanocomposite samples synthesized from C_{60} under various pressures P_{syn} and temperatures T_{syn}.

P_{syn} (GPa)	T_{syn} (°C)	ρ (g/cm^3)	P (N)	H_v (GPa)	K_{1c} (MN/m$^{3/2}$)
12.5	600	2.8	1.96	68 ± 5	–
			5.42	88 ± 5	8.3 ± 1.3
12.5	750	2.9	1.96	61 ± 6	5.9 ± 0.7
–	–	–	3.64	84 ± 4	8.9 ± 2.2
12.5	900	3.2	1.96	93 ± 14	7.9 ± 0.3
			5.42	62 ± 3	6.9 ± 0.7
12.5	1400	3.05	1.96	119 ± 15	10 ± 2
			5.42	66 ± 5	–
13	800	3.1	4.54	122 ± 9	24 ± 5
13.5	900	3.1	3.43	68 ± 4	9.5 ± 1
13.5	1000	3.4	3.43	125 ± 8	9.6 ± 0.7
			4.54	79 ± 8	12.3 ± 1.4
± 0.5 GPa	$\pm 20\%$	± 0.15 g/cm^3			

$l \sim 2\pi/\Delta Q$, where ΔQ is the half-width of the peak in units of the scattering wave vector (for a polycrystalline sample an analogous estimate gives the characteristic crystallite size). The corresponding calculation gives 7–10 Å for diamondlike (predominantly sp^3) regions and 15–20 Å for graphitic regions.

In summary, increasing the synthesis temperature results in the formation of an amorphous sp^2–sp^3 nanocomposite. The results of scanning electron microscopy confirm this interpretation (Fig. 2). The amorphous sample obtained at lower temperatures is a uniform material on a micron scale, while the high-temperature sample has a complicated macroscopic morphology. The change in the morphology of the samples is due to the rearrangement of the structure on a nanoscale, while the sample remains amorphous on large scales. Crystallization of the amorphous nanocomposite starts near 1400 °C (curve *4*, Fig. 1). At this temperature diamond crystallites of appreciable size are formed, since in addition to the reflection peak (111) there are weak reflections (220) and (311), as are graphite clusters, since the peaks of the graphitic phase shift toward the exact positions of the reflections (002) and (004) of graphite. The crystallite sizes estimated from the widths of the x-ray peaks are ~ 50 Å for graphite and ~ 25 Å for diamond.

The data for the hardness and fracture resistance of amorphous and nanocomposite samples are presented in Table I and Fig. 3, which also show points corresponding to 3D polymers of different density and graphitic disordered phases. We call attention to the general trend in the behavior of the hardness, the growth of H_v with increasing density of the carbon phases (Fig. 3); in addition, our results are in good agreement with the $H_v(\rho)$ data for amorphous carbon films.[11] The large variance in the values obtained for the hardness makes it impossible to establish a systematic dependence on the load or type of phase. Nonetheless, the measurement accuracy is sufficient to conclude that an appreciable increase in hardness to values characteristic for diamond is observed for nanocomposite phases with density in the range 3.0–3.4 g/cm^3. The fracture resistance of such
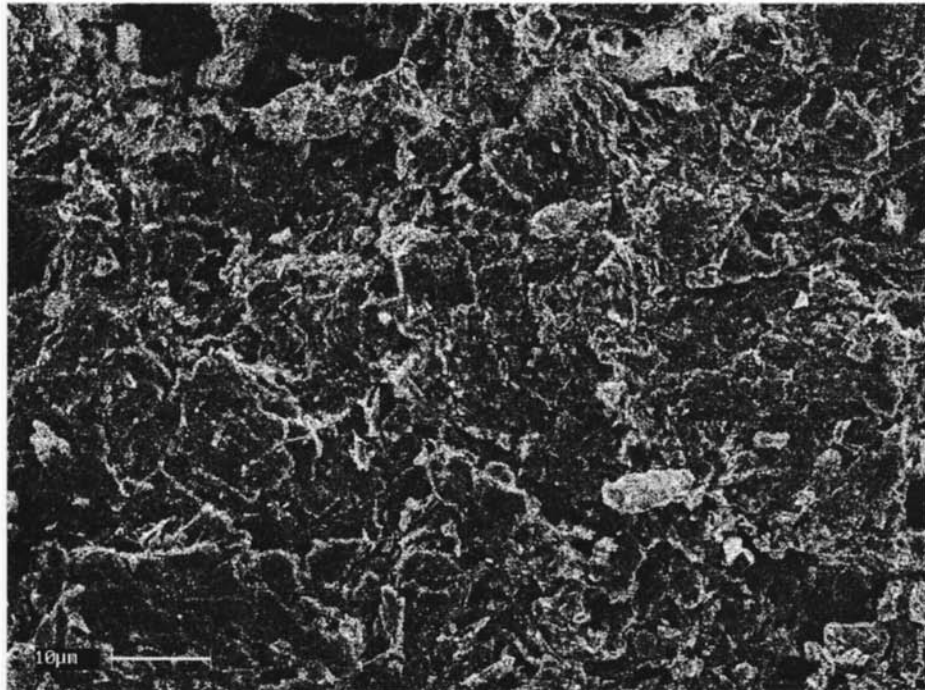
A)
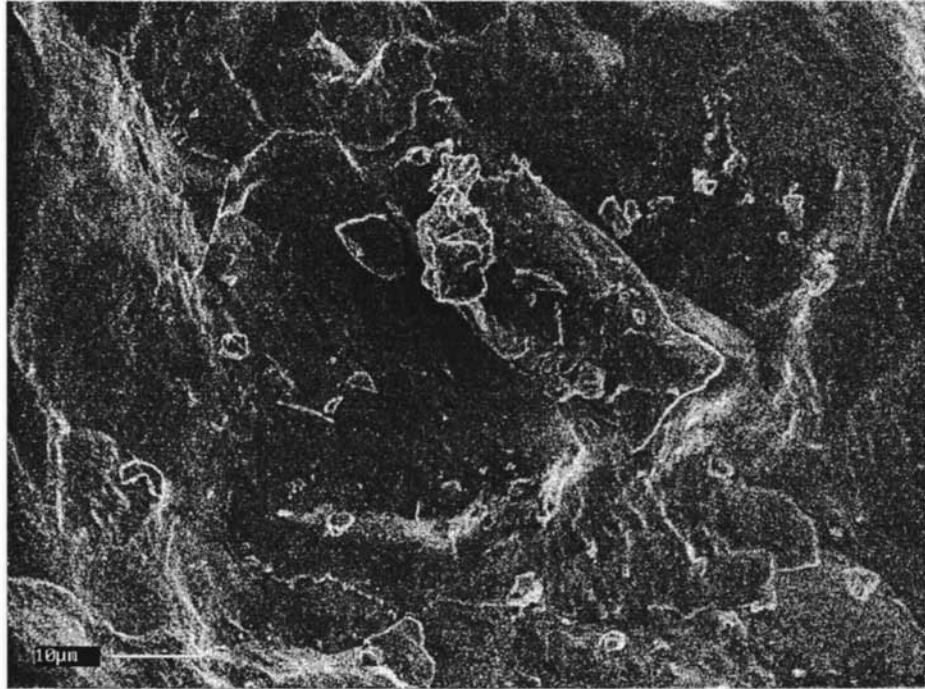
B)

FIG. 2. Scanning electron microscope images of the surface of amorphous diamondlike (A) and nanocomposite (B) samples.
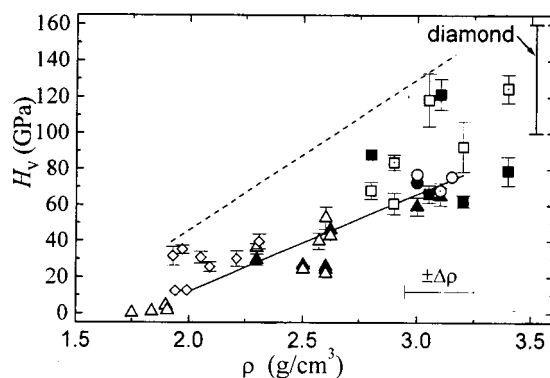
FIG. 3. Hardness versus the density for carbon phases obtained from C_{60}: triangles — 3D polymers, rhombi — graphitic amorphous phases, circles — diamondlike amorphous phases, squares — sp^2–sp^3 nanocomposites. The open symbols correspond to loads ≈ 2 N on the indenter, symbols with a centered dot correspond to ≈ 3.5 N, and filled symbols correspond to ≈ 5 N. The diamond data[13] were taken for 2–5 N loads. The solid line corresponds to the curve for the amorphous films,[11] and the dashed line is apparently the limit of maximum hardness achievable for carbon phases obtained from C_{60}.

phases can be two times greater than the values for diamond 7–10 MN/m$^{3/2}$ (see Table I).[14]

4. Although the formal thermodynamic equilibrium of fluorite C_{60} with diamond lies at negative pressures, kinetic factors determine the real structural evolution of fullerite under pressure. Specifically, at pressures up to 8 GPa the fullerite–diamond transition occurs through graphitization, just as for amorphous soots.[14] However, graphitization of soots is observed at least up to 15 GPa,[14] whereas for C_{60} the situation changes radically already at 12–13 GPa. An amorphous phase with a high fraction of sp^3 states (up to 80%) forms in this pressure range at record low temperatures ~ 500 °C. The convex shape of the spherical molecules makes it possible for them to approach one another effectively under pressure and lends a high capacity for the formation of covalent bonds between molecules, with the appearance of sp^3 states. At the same time the extremely high stability of C_{60} molecules prevents the formation of graphitic clusters. The formation of a disordered network of atoms from 3D polymers apparently occurs without the rupture of a large number of covalent bonds of the initial C_{60} molecules as structural units.

As the synthesis temperature increases, evidently, spatial separation of sp^2 and sp^3 atoms occurs (which is simply advantageous energetically) and first amorphous and then crystalline graphite–diamond nanocomposites form. The yield of nanodiamonds accompanying crystallization of such an amorphous state reaches 50–80%. The corresponding crystallization temperature (~ 1200–1400 °C) is much lower than the temperature of the direct noncatalytic graphite–diamond transformation at these pressures.

It is interesting that the mechanical characteristics of the synthesized nanocomposites are extremely high, even though the materials contain a large fraction of graphitic clusters. We note that the mechanical characteristics of the nanocrystalline diamond compacts obtained with the standard technology[15] ($H_v \sim 25$ GPa and $K_{1c} \sim 4$–6 MN/m$^{3/2}$) are two to three times lower than those of a diamond single crystal. There are several reasons why in our case the nanocomposites have a high hardness: 1) the nano-

clusters are apparently close to optimal size (see Ref. 10) to prevent the motion of dislocations; 2) because the formation of nanocomposites from large fullerite crystals is ''homogeneous'' in character, there are no stresses, nanopores, or impurities on the boundaries of the nanoclusters; 3) graphitic clusters themselves give high mechanical characteristics, since the graphitic phases obtained at even lower pressures have a quite high hardness ($\sim$ 40 GPa; see Fig. 3); and, 4) because the fraction of diamondlike clusters is high, stiffness percolates along them and a stiff framework is formed.

In summary, the method for obtaining diamond-containing nanocomposites via amorphization of fullerite C_{60} followed by crystallization without intermediate graphitization is extremely promising. It is very likely that nanocomposites with a smaller fraction of graphitic clusters and higher mechanical characteristics can be obtained at higher pressures 15–20 GPa.

[1] W. Kraetschmer, L. D. Lamb, K. Fostiropolous, and D. Huffman, Nature (London) **347**, 354 (1990).

[2] M. Núñez-Regueiro, L. Abello, G. Lucazeau, and J-L. Hodeau, Phys. Rev. B **46**, 9903 (1992).

[3] E. Yu. Tonkov, *Handbook of High Pressure Phase Transformations* (Gordon and Breach, Philadelphia, 1992), Vols. 1–2.

[4] V. V. Brazhkin, A. G. Lyapin, Yu. V. Antonov *et al.*, JETP Lett. **62**, 350 (1995).

[5] M. Núñez-Regueiro, L. Marques, J-L. Hodeau *et al.*, Phys. Rev. Lett. **74**, 278 (1995).

[6] L. Marques, J-L. Hodeau, M. Núñez-Regueiro, and M. Perroux, Phys. Rev. B **54**, R12633 (1996).

[7] V. V. Brazhkin, A. G. Lyapin, and S. V. Popov, JETP Lett. **64**, 803 (1996).

[8] V. V. Brazhkin, A. G. Lyapin, S. G. Lyapin *et al.*, Rev. High Pressure Sci. Technol. **7**, 817 (1998).

[9] A. G. Lyapin, V. V. Brazhkin, S. G. Lyapin *et al.*, Phys. Status Solidi B **211**, 401 (1999).

[10] S. Barnett and A. Madan, *Physics World*, January 1998, p. 45.

[11] M. Weiler, S. Sattel, T. Giessen *et al.*, Phys. Rev. B **53**, 1594 (1996).

[12] A. R. Evans and T. R. Wilshaw, Acta Metall. **24**, 939 (1976).

[13] A. V. Kurdyumov, V. G. Malogovets, N. V. Novikov *et al.*, *Polymorphic Modifications of Carbon and Boron Nitride* (Metallurgiya, Moscow, 1994).

[14] A. Onodera, Y. Irie, K. Higashi *et al.*, J. Appl. Phys. **69**, 2611 (1991).

[15] K. Kondo, S. Kukino, and H. Hirai, J. Am. Ceram. Soc. **79**, 97 (1996).

Translated by M. E. Alferieff

Quasi-one-dimensional antiferromagnet LiCuVO$_4$

A. N. Vasil'ev

M. V. Lomonosov Moscow State University, 119899 Moscow, Russia

An antiferromagnetic transition is observed in the quasi-one-dimensional metal-oxide compound LiCuVO$_4$. A wide peak is observed in the temperature dependence of the magnetic susceptibility at $T_M = 28$ K, and the magnetic susceptibility exhibits a sharp drop at $T'_N \approx 4$ K. As the magnetic field increases, the antiferromagnetic-ordering temperature $T_N = 2.3$ K at first increases somewhat and then decreases rapidly. The exchange interaction in the chains of copper–oxygen octahedra is estimated to be $J_1 = 22.5$ K. The interchain interaction is estimated to be $J_2 \sim 1$ K. © *1999 American Institute of Physics.* [S0021-3640(99)01111-1]

PACS numbers: 75.30.Kz, 75.50.Ee, 75.30.Cr

The discovery of diverse cooperative quantum phenomena in complex metal oxides has stimulated the search for inorganic materials with a low-dimensional magnetic subsystem. This search has uncovered a variety of new quasi-one- and quasi-two-dimensional compounds, as well as systems of intermediate dimension — coupled magnetic chains or spin ladders. Such compounds are distinguished, as a rule, by specific temperature dependences of the magnetic properties and are characterized by quite low magnetic ordering temperatures. In certain cases magnetic ordering does not occur at all and one or another interaction mechanism opens up a spin gap in the magnetic excitation spectrum of a low-dimensional magnet.[1,2] The magnetic properties of many low-dimensional magnets are due to the presence of copper ions Cu^{2+} or vanadium ions V^{4+} in their structure; in addition, the most diverse variations of low-dimensional magnetic structures are encountered in compounds where these ions coexist with lithium ions Li^{1+}. Thus, in lithium cuprate LiCuO$_2$ the copper ions Cu^{2+} ($S = 1/2$) in linear CuO$_4$ chains are bound with one another by a ferromagnetic interaction, while the interaction between chains is antiferromagnetic.[3] Magnetic V^{4+} ($S = 1/2$) and nonmagnetic V^{5+} ($S = 0$) ions are present in the layered structure of lithium vanadate LiV$_2$O$_5$, and each of the ions form zig-zag chains of vanadium pyramids VO$_5$. A magnetic phase transition occurs in this system only at ultralow temperatures.[4]

The orthorhombic metal-oxide compound LiCuVO$_4$, where all of the ions listed above are present, is genetically related with the spinel structure, where the lithium ions Li^{1+} and magnetic copper ions Cu^{2+} ($S = 1/2$) are located in an octahedral environment, while the nonmagnetic vanadium ions V^{5+} ($S = 0$) are located in a tetrahedral environment consisting of oxygen ions O^{2-} (Ref. 5). As shown in Fig. 1, the chains of copper-
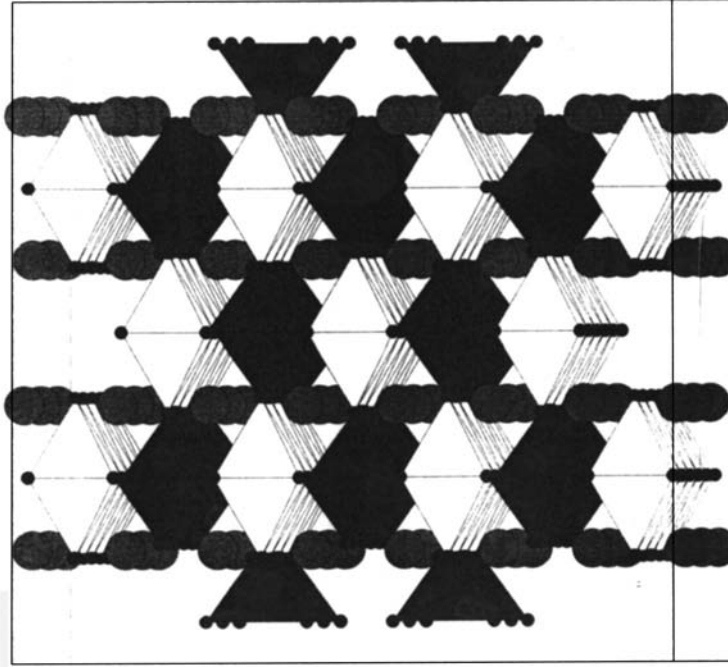
FIG. 1. Crystal structure of orthorhombic spinel $LiCuVO_4$ in a polyhedral representation. Copper is located in the unshaded octahedra, which are coupled along the edge in the basal plane into linear chains. Vanadium is located in the isolated shaded tetrahedra. The polyhedra for lithium, which is represented by circles, are not presented.

oxide octahedra CuO_6, which are coupled along an edge in the basal plane, extend along the a axis, and they form almost regular triangles in the $b-c$ plane. Chains of lithium–oxygen octahedra LiO_6 extend along the b axis, and the vanadium–oxygen tetrahedra VO_4 are isolated from one another. The room-temperature lattice constants are: $a = 0.5652$ nm, $b = 0.5798$ nm, and $c = 0.8747$ nm,[5] so that the copper–oxygen octahedra are characterized by a strong tetragonal distortion, the long axis of the CuO_6 octahedra being oriented along the c axis. Away from stoichiometry in $Li_{1-x}CuVO_4$ ($0 \leqslant x \leqslant 0.2$) samples a structural phase transition of the cooperative Jahn–Teller effect type is observed above room temperature.[6] This transition has not been observed in stoichiometric samples.

The $LiCuVO_4$ samples were prepared by solid-phase synthesis from a stoichiometric mixture of lithium carbonate Li_2CO_3, copper oxide CuO, and vanadium pentoxide V_2O_5. Synthesis was conducted at 530 °C for one week and after additional repeated mixings for one month. The final product — a light-yellow powder — consisted of a monophase sample, as was verified by x-ray diffraction. Magnetic measurements were performed at the Institute of Solid-State Physics at Tokyo University on a ''Quantum Design'' SQUID in fields up to 5 T in the temperature range 2–300 K.

The temperature dependence of the magnetic susceptibility of $LiCuVO_4$ is presented in Fig. 2. As temperature decreases, the magnetic susceptibility χ passes through a wide
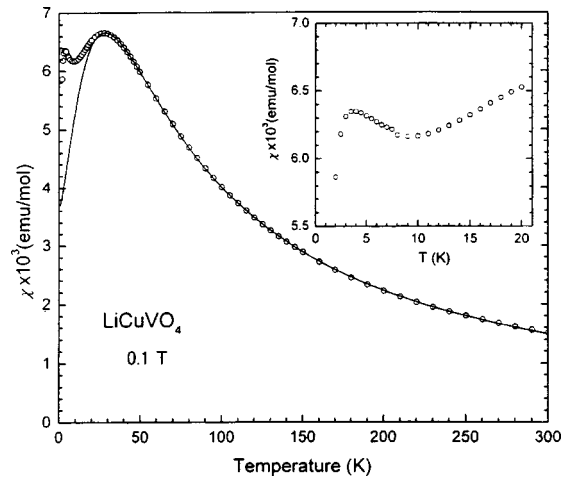
FIG. 2. Temperature dependence of the magnetic susceptibility of LiCuVO$_4$ in a field $H=1$ T. Inset: Data for $T \leqslant 20$ K on an enlarged scale.

peak at $T_M = 28$ K, then increases somewhat at ~ 10 K, and once again sharply decreases at $T_{N'} \sim 4$ K. The magnetization M as a function of the field H is linear in a wide range of experimental temperatures, but at the lowest temperatures, as shown in Fig. 3, the dependence $M(H)$ deviates from linearity in the direction of smaller values. In contrast to the wide peak in χ at T_M, the position of the low-temperature peak in χ at $T_{N'} \sim 4$ K depends nonmonotonically on the magnetic field. In weak fields the peak first shifts somewhat to higher temperatures and then rapidly shifts to lower temperatures as the field increases further. This dependence is displayed in Fig. 4, where the solid line connecting the experimental points is drawn only for visual clarity.

All experimental data presented are characteristic for a quasi-one-dimensional magnet which, as the temperature decreases, first exhibits short-range magnetic correlations in chains and then undergoes three-dimensional antiferromagnetic ordering at low
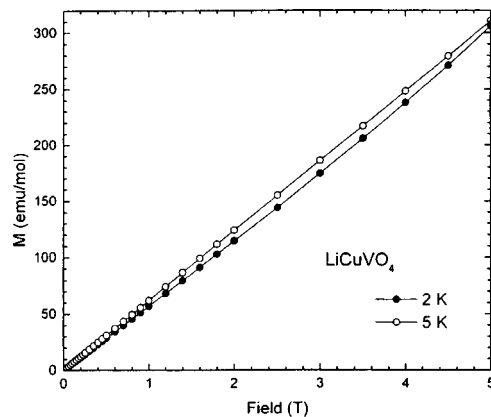

FIG. 3. Field dependences of the magnetization of LiCuVO$_4$ at $T=2$ K ($\bullet$) and $T=5$ K ($\circ$).
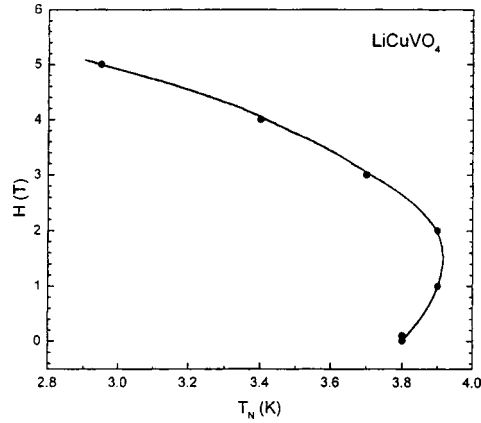
FIG. 4. Field dependence of $T_{N'}$ (positions of the low-temperature peak in the susceptibility χ) in LiCuVO$_4$.

temperatures. The antiferromagnetic ordering temperature is strictly different from $T_{N'}$, and it can be determined according to the peak in the temperature dependence of the derivative $\partial\chi/\partial H$. In weak fields $T_N = 2.3$ K, and it decreases to 2 K at $H = 5$ T.

At high temperatures ($T \gtrsim 150$ K) the magnetic susceptibility of LiCuVO$_4$ is described by the Curie–Weiss law

$$\chi = C/T - \Theta$$

with $\Theta = -31.5$ K and effective g factor 2.26. At lower temperatures and near the wide peak the magnetic susceptibility can be approximated well by a polynomial corresponding to the Bonner–Fisher curve.[7] The small increase in the magnetic susceptibility in the range from 10 to 4 K is probably due to impurities and defects. Comparing the Bonner–Fisher curve with experiment gives the appreciably larger value 2.39 for the g factor averaged over the crystallographic directions, and from the position of the wide peak along the temperature scale,

$$T_M = 1.282 J_1,$$

it follows[8] that the exchange integral in the chains is $J_1 = 22.5$ K. The interchain exchange interaction J_2 can be estimated[9] from the three-dimensional antiferromagnetic ordering temperature T_N as

$$J_2 = \frac{T_N}{1.28\sqrt{\ln(5.8J_1/T_N)}}.$$

In order of magnitude $J_2 \sim 1$ K, and the saturation magnetization is $m_0 = 1.017\sqrt{J_2/J_1} = 0.2\mu_B$.

The nonmonotonic behavior of the critical temperature in a magnetic field (Fig. 4) is characteristic for low-dimensional magnets. The initial increase in the antiferromagnetic ordering temperature is due to the fact that the magnetic field effectively decreases the number n of degrees of freedom in the magnetic subsystem, transferring a Heisenberg magnet ($n=3$) into an xy-type magnet ($n=2$). The subsequent decrease of the critical temperature is due to the Zeeman splitting of the levels in a magnetic field. The weak

nonlinearity of the magnetization at low temperatures is probably explained by the fact that spin reorientation occurs in $LiCuVO_4$ in a magnetic field, but a magnetic-field-induced lowering of the Néel temperature is superposed on this process.

Further investigation of quasi-one-dimensional antiferromagnetic ordering in $LiCuVO_4$ apparently requires neutron diffraction investigations on single-crystal samples. Specifically, the value obtained for the interchain exchange integral may be too low because of frustrations of the exchange interaction in a triangular arrangement of chains, if the interaction between the copper ions in the $b-c$ plane is antiferromagnetic.

[1] M. Hase, I. Terasaki, and K. Uchinokura, Phys. Rev. Lett. **70**, 3651 (1993).
[2] M. Isobe and Y. Ueda, J. Phys. Soc. Jpn. **65**, 1178 (1996).
[3] M. Boehm, S. Coad, and S. Uchida, Europhys. Lett. **43**, 77 (1998).
[4] Y. Karaki, private communication.
[5] A. Durif, J. C. Grenier, J. C. Joubert, and T. Q. Duc, Bull. Soc. Fr. Mineral. Cristallogr. **89**, 407 (1966).
[6] R. Kanno, Y. Kawamoto, Y. Takeda *et al.*, Solid State Chem. **96**, 397 (1992).
[7] W. E. Hatfield, J. Appl. Phys. **52**, 1985 (1981).
[8] J. C. Bonner and M. E. Fisher, Phys. Rev. A **135**, 640 (1964).
[9] H. J. Schulz, Phys. Rev. Lett. **77**, 2790 (1996).

Translated by M. E. Alferieff

Commensurability oscillations and a new phase transition in YBa$_2$Cu$_3$O$_y$ single crystals

A. A. Zhukov,[*)] M. G. Mikheev,[†)] and V. I. Voronkova
M. V. Lomonosov Moscow State University, 119899 Moscow, Russia

K. I. Kugel' and A. L. Rakhmanov
Scientific-Research Center of Applied Electrodynamics, Russian Academy of Sciences, 127412 Moscow, Russia

H. Küpfer and T. Wolf
Forschungszentrum Karlsruhe, Institut für Technische Physik, D-76021 Karlsruhe, Germany

G. K. Perkins and A. D. Caplin
Centre for High Temperature Superconductivity, Blackett Laboratory, Imperial College, London SW7 2BZ, United Kingdom

Magnetization oscillations due to the commensurability of the vortex and crystal lattice periods in YBa$_2$Cu$_3$O$_y$ ($y = 6.97 \pm 0.02$) single crystals are investigated using a high angular resolution magnetometer. A sharp peak in the temperature dependence of the oscillation amplitude as well as other features in the behavior of the oscillation amplitude and of the irreversible magnetization are observed at $T_f \sim 60$ K. It is inferred that T_f is the temperature of a transition of the solid vortex state to a smectic phase. © *1999 American Institute of Physics.*
[S0021-3640(99)01211-6]

PACS numbers: 74.72.Bk, 75.60.Ej, 74.25.Ha

The lamination of the crystal structure of high-temperature superconductors is responsible for the large anisotropy and unusual behavior of these materials. In combination with the short coherence length the laminated structure gives rise to intrinsic pinning of vortices between the CuO planes.[1] The energy of the vortex lattice is minimum when the intervortex distance is comparable to the interlayer distance. A theory of commensurate vortex structures has been developed in Refs. 2 and 3. Magnetic moment oscillations due to commensurability have been observed experimentally in Refs. 4–6. These oscillations are very sensitive to the perfection of the vortex lattice and can serve as an effective tool for studying the character of its ordering.

A theory describing possible structures for a system of vortices which are parallel to the superconducting layers has been proposed recently.[7] Three different vortex phases are predicted to exist in this case. In addition to liquid and solid phases, a smectic vortex phase,[8] which would be characterized by liquid properties in the direction of the CuO

planes and crystalline order in the direction of the *c* axis (as in ordinary smectic liquid crystals), is expected at intermediate temperatures. In the present work we investigated commensurability oscillations in perfect $YBa_2Cu_3O_y$ single crystals in order to determine the unusual features due to the possible existence of a smectic ordering of the vortices.

Five $YBa_2Cu_3O_y$ single crystals[9] grown from a fluxed melt and subjected to a long anneal (300–700 h) in an oxygen atmosphere at 1 bar pressure were investigated. As a result, all samples showed a diamagnetic signal at $T_c \approx 91$ K; the oxygen content was $y = 6.97 \pm 0.02$. At the same time the samples differed substantially with respect to impurity content, so that their screening currents varied by more than two orders of magnitude (from 80 A/cm^2 for the sample CD to 4×10^4 A/cm^2 for the sample MK) at $T = 77$ K in a magnetic field $B(\parallel c) = 1$ T. The three samples VG, AZ, and CD were essentially in a single-domain state immediately after synthesis. Two other samples, WZ and MK, were detwinned by means of uniaxial detwinning.[10] X-ray diffraction analysis performed on four samples showed that the disordering of the *c* axis did not exceed 0.02°.

An Oxford Instruments model 5^H vibrating magnetometer with a system of mutually perpendicular detection coils, which made it possible to measure simultaneously two components of the magnetic field, parallel and perpendicular to the applied magnetic field, was used for the magnetic measurements. For small angles ($<0.3°$) between the *ab* plane and the magnetic field the component m_{std} parallel to the applied magnetic field gives a magnetization parallel to the CuO planes, $M_\parallel \approx m_{std}/V$, while the transverse component m_{ort} corresponds to magnetization along the *c* axis $M_c \approx m_{ort}/V$ (V is the volume of the sample). The samples rotated around the vertical axis (perpendicular to the magnetic field) with angular resolution 0.01°.

Commensurability oscillations for the sample MK are shown as an example in Fig. 1. The small amplitude of the oscillations and the presence of a monotonic component precluded a direct quantitative analysis of the magnetic moment $M(H)$, and for this reason the differential susceptibility $\chi_d = dM/dH$ was used. For χ_d the oscillating part dominates and quantitative analysis becomes reliable. This approach showed the oscillations of the differential susceptibility χ_d to have a pronounced triangular form (Fig. 1b). This attests to the existence of a sharp transition between different commensurate vortex states.

The condition of commensurability presumes that an integral number *k* of intervortex spacings a_c in a direction normal to the layers is equal to an integral number *l* of interlayer periods *d*. The energy of a vortex is minimum for $k = 1$. Therefore the corresponding commensurability condition is

$$a_c = (\sqrt{3}\Phi_0/2\Gamma B)^{1/2} = ld,$$

where $\Gamma^2 = M_c/M_{ab}$ is the anisotropy of the effective masses. Here and below we ignore the small anisotropy between the directions *a* and *b*.

Depending on the magnetic field, the points of commensurability should be periodic in $B^{-1/2}$ with period $\Delta B^{-1/2} = d(2\Gamma/\sqrt{3}\Phi_0)^{1/2}$. The experiment indeed showed periodicity in $B^{-1/2}(n)$ (inset in Fig. 1a). For all the crystals with high oxygen content that were investigated in the present work as well as for the crystals analyzed in Refs. 4–6 the period of the oscillations falls into a narrow range $\Delta B^{-1/2} = (6.6 \pm 0.3) \times 10^{-2}$ T$^{-1/2}$. As
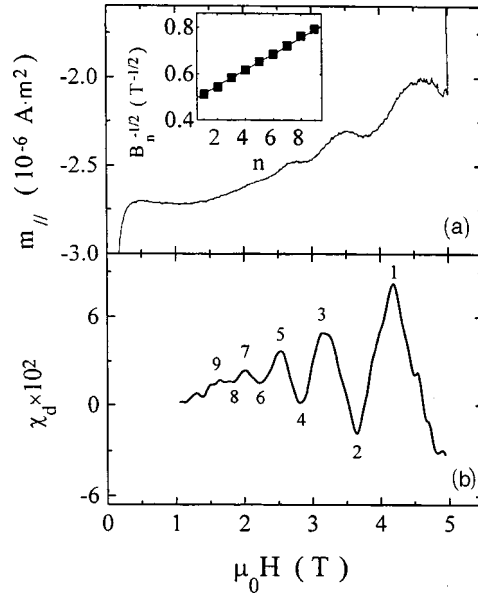
FIG. 1. (a) Field dependence of the magnetic moment of the single-crystal sample MK at temperature 60 K in a magnetic field H parallel to the CuO planes. (b) Differential susceptibility. Inset: Position of the extrema on the scale $B^{-1/2}$ ($T^{-1/2}$) as a function of the number n of the extremum.

expected, $\Delta B^{-1/2}$ is essentially independent of the magnetic field direction and temperature.

Using the expression following from the commensurability condition

$$\Gamma = \frac{\sqrt{3}}{2}\Phi_0\left(\frac{\Delta B^{-1/2}}{d}\right)^2$$

and the crystal lattice period $d = 11.7$ Å,[11] the anisotropy of effective masses is found to be $\Gamma^2 = 30 \pm 5$. This value agrees well with other results.[12]

In contrast to the period of the oscillations, which is temperature-independent, the amplitude varies rapidly and has a sharp peak (Fig. 2). This behavior, which is characteristic for all of the experimental samples, will be the main subject of the subsequent discussions and interpretations. The position T_f (which we shall call the melting temperature) of the peak slowly shifts to higher temperatures as the order l of commensurability decreases or, correspondingly, the magnetic field increases. For fixed l the values of T_f are close in different samples. For example, for $l = 7$ (with the corresponding magnetic field 4.0 ± 0.4 T, which depends on the internal parameters of different samples) T_f is 59 K, 66 K, 58 K, 63 K, and 59 K for the samples VG, AZ, WM, CD, and MK, respectively. Despite the small differences in T_f (which can be attributed to the difference in the internal parameters and strength of the pinning), the closeness of the values obtained shows that the anomaly, which is insensitive to the large difference in the pinning properties of the samples, is of a thermodynamic character.
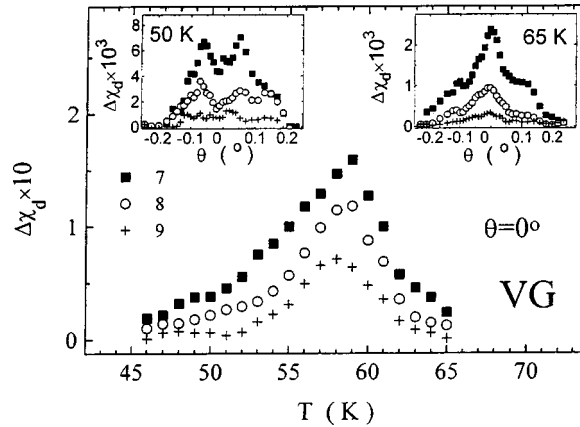
FIG. 2. Temperature dependence of the oscillation amplitude of the differential susceptibility of the single-crystal sample VG. The applied magnetic field is parallel to the CuO planes. The commensurability parameter $l = 7$, 8, and 9 corresponds to magnetic fields $\mu_0 H = 3.8$, 3.0, and 2.4 T, respectively. Insets: Angular dependence of the oscillation amplitude above and below the temperature T_f.

The angular dependences of the oscillation amplitude for temperatures above and below T_f are different. At high temperatures (right-hand inset in Fig. 2) the oscillation amplitude decreases continuously, and below T_f two sharp peaks are observed with the magnetic field deviating in both directions away from the CuO planes (left-hand inset in Fig. 2). In both cases the oscillations vanish for an angle of deviation $\sim 0.2°$.

The temperature dependences of the hysteresis of magnetization $M_\parallel$ provided further confirmation of the existence of a phase transition at temperature T_f, and they also provided evidence concerning the nature of the transition. The nonoscillatory part predominates in the irreversible magnetic moment. Therefore it is determined by physical processes that are unrelated with the oscillations. As will be shown below, $M_\parallel$ is related with the current j_c^c along the c axis; this current gives rise to motion of vortices parallel to the CuO planes. A peak is also present in $M_\parallel(T)$ at temperature T_f (Fig. 3). This gives additional evidence that the nature of the vortex system changes at this point. Outside a very narrow range of angles (approximately $\pm 0.2°$) the peak in $M_\parallel(T)$, like the oscillations, vanishes. At low temperatures the current $j_c^c \sim \Delta M_\parallel$ exhibits a quite weak temperature dependence. However, above T_f it decreases very rapidly and vanishes at a much lower temperature than T_c or the expected temperature of three-dimensional melting of the vortex lattice $T_m \approx 90$ K (T_m was calculated on the basis of the values for $H \parallel c$ using the anisotropic Ginzburg–Landau model). The observed behavior agrees with melting of a solid vortex lattice into a smectic structure. Indeed, the smectic phase was described in Refs. 8 and 13 as a combination of a solid phase in the direction of the c axis and a liquid phase in the direction of the CuO planes. Since fluctuations and pinning are present, we can attribute the rapid decrease in $\Delta M_\parallel(T)$ to a second-order melting,[7] which leads to free motion of vortices parallel to the CuO planes. The presence of oscillations attests to the presence of good order in the system of vortices along the c axis at temperatures above T_f.

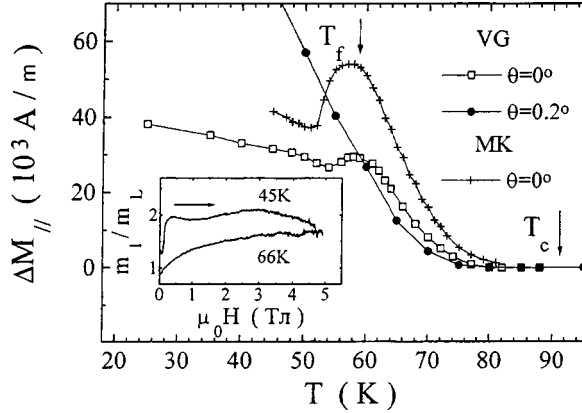We shall now briefly discuss the relation between the irreversible magnetic moment

FIG. 3. Temperature dependence of the irreversible magnetization $\Delta M_\parallel$ of the single-crystal samples VG and MK. Inset: Field dependence of the ratio of the irreversible magnetic moments for the magnetic field H parallel to the long (m_L) and short (m_l) transverse edges of the sample VG. The arrow marks the ratio L/l of the transverse dimensions of the sample.

and the currents in the sample. According to the anisotropic Bean model,[14] Δm is determined by two different screening currents. One current (j_c^c) flows in the direction of the c axis, while the other current ($j_c^\parallel$) flows parallel to the CuO planes. These two components can be extracted from two measurements of $\Delta M_\parallel$ for a prolate rectangular sample for magnetic field directions $H \parallel ab$, parallel to the long and short edges of the sample, respectively. For vortex penetration predominantly in the direction of the c axis the magnetization $\Delta M_\parallel \approx j_c^\parallel t$ (t is the sample thickness) should be equal for both directions of the magnetic field. For vortex penetration parallel to the CuO planes $\Delta M_\parallel$ is determined by the current component j_c^c and is calculated as $\Delta M_\parallel \approx j_c^c L/2$, where L is the size of the crystal in a direction perpendicular to the applied magnetic field.[14]

The sample VG was the only one with a prolate shape. As is evident from the inset in Fig. 3, the ratio of the magnetizations for different directions of the magnetic field is much greater than 1, and for large H it agrees well with the ratio of edge lengths of the sample. This means that the measured quantity $\Delta M_\parallel$ corresponds to vortex motion parallel to the CuO planes.

The theory predicts melting of the smectic phase into a vortex liquid at high temperatures. Resistance investigations[15,7] confirm a second-order transition into a vortex liquid at $T_m \sim 90$ K, but the vanishing of vortex pinning makes it impossible to observe this transition in our measurements.

The decrease in the oscillation amplitude in the solid vortex phase with decreasing temperature could be due to a rapid increase of the pinning by point defects,[16] which suppress order in the vortex structure. According to the theory of Ref. 7, smectic order should be insensitive to point defects. Therefore thermal disordering and decrease of pinning become the main factors responsible for the decrease in the oscillation amplitude with increasing temperature.

*)e-mail: zhukov@lt.phys.msu.su
†)e-mail: mikh@lt.phys.msu.su

[1] M. Tashiki and S. Takahashi, Solid State Commun. **70**, 291 (1989).

[2] B. I. Ivlev and N. B. Kopnin, Phys. Rev. Lett. **64**, 1828 (1990).

[3] L. Bulaevskii and J. R. Clem, Phys. Rev. B **44**, 10234 (1991).

[4] M. Oussena, P. A. J. de Groot, R. Gagnon *et al.*, Phys. Rev. Lett. **72**, 3606 (1994).

[5] H. Kupfer, A. A. Zhukov, A. Will *et al.*, Phys. Rev. B **54**, 644 (1996).

[6] A. A. Zhukov, Yu. V. Bugoslavsky, G. K. Perkins *et al.*, Physica C **282-287**, 2151 (1997).

[7] L. Balents and D. R. Nelson, Phys. Rev. Lett. **73**, 2618 (1994); L. Balents and D. R. Nelson, Phys. Rev. B **52**, 12951 (1995).

[8] K. B. Eftov, Zh. Éksp. Teor. Fiz. **76**, 1781 (1979) [Sov. Phys. JETP **49**, 905 (1979)].

[9] Th. Wolf, W. Goldacker, B. Obst *et al.*, J. Cryst. Growth **96**, 1010 (1989).

[10] A. A. Zhukov, H. Küpfer, H. Claus *et al.*, Phys. Rev. B **52**, R9871 (1995).

[11] J. D. Jorgensen, B. W. Veal, A. P. Paulikas *et al.*, Phys. Rev. B **41**, 1863 (1990).

[12] E. Z. Meĭlikhov and V. G. Shapiro, Sverkhprovodimost' (KIAE) **4**, 1437 (1991) [Superconductivity **4**, 1353 (1991)].

[13] B. Horovitz, Phys. Rev. Lett. **67**, 378 (1991); G. Blatter, B. I. Ivlev, J. Rhyner *et al.*, Phys. Rev. Lett. **66**, 2392 (1991).

[14] V. V. Moshchalkov, A. A. ZHukov, V. D. Kuznetsov *et al.*, Sverkhprovodimost (KIAE) **2**, 84 (1989) [Superconductivity **2** 98 (1989)]; E. M. Gyorgy, R. B. van Dever, K. A. Jackson *et al.*, Appl. Phys. Lett. **55**, 283 (1989).

[15] W. K. Kwok, J. Feindrich, U. Welp *et al.*, Phys. Rev. Lett. **72**, 1088 (1994).

[16] G. Blatter, J. Rhyner, and V. M. Vinokur, Phys. Rev. B **43**, 7826 (1991).

Translated by M. E. Alferieff